STRESS WAVE PROPAGATION AND TUNABILITY IN 1D GRANULAR SYSTEMS

by

Wen Zhang

A dissertation submitted to the faculty of
The University of North Carolina at Charlotte
in partial fulfillment of the requirements
for the degree of Doctor of Philosophy in
Mechanical Engineering

Charlotte

2021

Approved by:

_____
Dr. Jun Xu

_____
Dr. Terry Xu

_____
Dr. Nigel Zheng

_____
Dr. Mesbah Uddin

_____
Dr. Shen-En Chen

ABSTRACT

WEN ZHANG. Stress Wave Propagation and Tunability in 1D Granular Systems

(Under the direction of DR. JUN XU)

Mechanical stress wave propagation in granular materials has attracted much attention for exploring new physical phenomena due to versatile engineering applications. One-dimensional (1D) granular systems, a type of artificially designed granular materials consisting of periodically aligned discrete particles, are demonstrated to produce unprecedented wave properties that are notably different from conventional engineering materials. By designing the critical characteristics of 1D granular systems, a remarkable tunability can be achieved, which yields various engineering applications. However, a systematic understanding of the stress wave behaviors within the system is still lacking.

Therefore, in this dissertation, firstly, 1D cylindrical composite granular chains are systematically investigated via experiments, numerical simulations, and theoretical analysis, which is demonstrated to support strongly nonlinear solitary waves. By creating material mismatch within single granular particles, a shell-dominated dynamic response is achieved in 1D composite granular chains. Next, the dynamic properties of solitary waves supported by 1D spherical granular chains are analyzed, making it possible to achieve an equivalent wave transmission among various materials and dimensions. Accordingly, two types of equivalent systems are designed to expand the understanding of governing factors in wave dynamics, including generalized and restricted equivalent systems. Furthermore,

two types of highly efficient and controllable stress wave attenuation approaches are developed based on 1D hollow cylindrical particles and kirigami lantern structures. The fundamental mechanisms of the two strategies are strain-softening behaviors of hollow cylindrical particles and unique folding-unfolding responses of kirigami cells during stress wave propagation, respectively. Finally, 1D cylindrical granular systems with various mismatch configurations, including mass, modulus, and thickness mismatch, are tailored to investigate quantitatively solitary wave tuning strategies. Meanwhile, the solitary wave attenuation capability can be further boosted by coupling different strategies or creating a multilayer granular chain.

This study comprehensively explores the stress wave propagation and tunability in various 1D granular systems via an integrated methodology, systematically uncovering the fundamental physical relations between wave dynamics and system properties. Results promote the science of stress wave propagation by developing the fundamental stress wave propagation laws and provide design guidance for next-generation impact protection, signal measurement, and monitoring systems.

ACKNOWLEDGMENTS

I gratefully acknowledge my advisor Dr. Jun Xu for his support and guidance in both course study and research work. He always encourages me to be confident and provides constructive guidance when I meet problems. To help me get familiar with my research, he broke down the research tasks and walked me through them step by step. Furthermore, he mentored my independent working skills and trained me in critical thinking by teaching me to challenge existing procedures. Following his path, I keep pushing myself to explore the unknown and try to achieve my full potential during the whole Ph.D. program.

I would like to express my gratitude to Dr. T.X. Yu, who provided a lot of valuable comments and insightful suggestions for improving the methodology and enhancing the theoretical foundation of my research work. He set me a good example by the ultimate pursuit of scientific research.

I want to thank Dr. Terry Xu, Dr. Nigel Zheng, Dr. Mesbah Uddin, and Dr. Shen-En Chen for being my committee members. Their inspiring advice helped me to accomplish more systematic work and become more professional in research presentations. I am also grateful to all members of our group. I would like to thank Xiang Gao for being supportive in both my research work and daily life. Thank Yikai Jia and Chunhao Yuan for suggestions on my numerical modeling. I appreciate Jiani Li for advice on equipment selection for my experimental setups.

Lastly, I am so blessed to have my parents in my corner. They always respect every

decision I make and provide support during my whole life. I am a simply better human being because of them.

TABLE OF CONTENTS

LIST OF TABLES xii

LIST OF FIGURES xiii

NOMENCLATURE xx

CHAPTER 1 INTRODUCTION 1

1.1 Analytical model of 1D granular systems 2

1.2 Strongly nonlinear solitary waves in 1D granular systems 6

1.3 Stress wave attenuation in 1D granular systems 11

CHAPTER 2 SOLITARY WAVE PROPAGATION IN 1D GRANULAR SYSTEMS ... 15

2.1 Methods 15

2.1.1 Configurations 15

2.1.2 Experimental setups 16

2.1.3 Finite element modeling 18

2.1.4 Validation 20

2.2 Results 21

2.3 Discussion 22

2.3.1 Core-shell type 22

2.3.2 Further Extension to the Sandwich type 30

2.4 Conclusions 34

CHAPTER 3 UNIVERSAL DESIGN OF EQUIVALENT SYSTEM SUPPORTING

SOLITARY STRESS WAVES 35

3.1 Methods 35

3.1.1 Theoretical analysis 36

3.1.2 Experimental setups 42

3.1.3 Finite element model 45

3.1.4 Validation 46

3.2 Results and discussions 48

3.2.1 Mechanism map 48

3.2.2 Generalized equivalent system 51

3.2.2.1 Experimental results 51

3.2.2.2 Numerical analysis 52

3.2.3 Restricted equivalent system 53

3.2.3.1 Experimental results 53

3.2.3.2 Numerical analysis 54

3.3 Conclusions 56

CHAPTER 4 STRESS WAVE ATTENUATION IN 1D GRANULAR SYSTEMS 57

4.1 Tunable traveling wave properties in 1D chains composed from hollow cylinders 58

4.1.1 Materials and methods 58

4.1.1.1 Experimental setups 58

4.1.1.2 Finite element model 60

4.1.2 Results 62

4.1.3 Discussion 65

4.1.3.1 The effect of impact velocity 65

4.1.3.2 The effect of impactor-to-particle mass ratio 72

4.1.3.3 The effect of thickness ratio 74

4.1.3.4 The effect of particle number 77

4.1.4 Conclusions 80

4.2 Kirigami-based lantern chain for superior impact mitigation 80

4.2.1 Methods 80

4.2.1.1 Kirigami fabrication 81

4.2.1.2 Experimental setup 82

4.2.1.3 Finite element model 84

4.2.1.4 Model validation 86

4.2.2 Results 87

4.2.3 Discussion 89

4.2.3.1 Impact energy 89

4.2.3.2 Cell number 93

4.2.3.3 Petal number 95

4.2.3.4 Hinge number 97

4.2.4 Conclusion 99

CHAPTER 5 TUNABILITY OF STRESS WAVE PROPAGATION IN 1D GRANULAR SYSTEMS 101

5.1 Method 101

5.1.1 1D granular chain setups 101

5.1.2 Configurations of solitary wave tuning strategies 102

5.1.3 Finite element modeling 103

5.1.4 Experimental setups 104

5.1.5 Validation 107

5.2 Results 108

5.2.1 Mass mismatch 108

5.2.2 Modulus mismatch 109

5.2.3 Thickness mismatch 110

5.3 Discussion 111

5.3.1 Coupling strategy 111

5.3.2 Multilayer granular chain 115

5.3.3 Mechanism map 119

5.4 Conclusions 120

CHAPTER 6 CONCLUDING REMARKS 121

REFERENCES 123

APPENDIX A: Formation of solitary waves in 1D composite granular chains 131

APPENDIX B: Demonstration of the contact law in 1D composite particles 132

APPENDIX C: Mesh size convergence study of equivalent systems 133

APPENDIX D: The evaluation criteria of equivalent systems used in experiments 134

APPENDIX E: The amplitude decay in experiments of equivalent systems 136

APPENDIX F: The return pass in equivalent systems 138

APPENDIX G: Waveforms in experiments of 1D cylindrical granular chains 139

APPENDIX H: Mesh size convergence study of 1D cylindrical granular chains 140

APPENDIX I: The effect of gravity 141

APPENDIX J: The elastic assumption of 1D cylindrical granular chains 142

APPENDIX K: The mitigating effect of 1D HC chains under a higher impact velocity 144

APPENDIX L: Investigation on the reusability of 1D kirigami lantern chains 146

APPENDIX M: PERMISSION LETTERS 147

LIST OF TABLES

Table 1 Core-shell granular chains fabricated for model validation..... 21

Table 2. Material properties and geometric parameters of granular chains in experiments 43

Table 3 Comparison of wave speeds in 1D granular chains 48

Table 4 Testing results of generalized equivalent systems under various impact velocities. 52

Table 5 Phase speed of restricted equivalent systems under different impact velocities.. 54

Table 6 Durations corresponding to different impactor-to-particle mass ratios 74

Table 7 The force mitigation ratios of 1D HC chains with different thickness ratios 77

Table 8 Amplitude and duration induced spatial positions of optimal mitigating efficiency 79

Table 9 Configurations of 1D cylindrical granular chains in experiments 106

Table 10 Compression ratios obtained from different configurations 108

LIST OF FIGURES

Figure 1 (a) Schematics of compressed particles in 1D spherical granular chains subjected to impulsive loadings, where u_i and x_i denote the displacement and coordinate of the i^{th} particle, respectively. The cross symbol is the original position of particle centers, while the solid circle represents the current position of particle centers. (b) An example of strongly nonlinear solitary waves in a monomer granular chain [39]. 3

Figure 2. Experimental techniques: typical experimental setups with (a) vertical [79] and (b) horizontal sliding rails [13]; (c) schematic of a laser Doppler vibrometer measuring systems [43]; (d) dynamic responses of spherical granular particles monitored by a high-speed camera [59]. 9

Figure 3 Numerical methods for exploring the wave behaviors in 1D granular systems. (a) Discrete element model of an elastic woodpile periodic structure [89]. (b) Finite element model of a hollow cylindrical granular chain [50].....11

Figure 4 (a) Oscillatory and monotonic shock-like waves in a "Sonic Vacuum" [11]; (b) Experimental setups of a brass-steel dimer chain in SHPB [95]; (c) The comparison between the results from experiments and the dissipative model in a steel granular chain [90]. 13

Figure 5 (a) Configuration of cylindrical composite particles. Type I: core-shell structure; Type II: sandwich structure. Schematic of (b) the particle fabrication process and (c) experimental setups. Herein, the contact force waveforms of two different locations were measured, i.e., the 1^{st} and 2^{nd} particle, the 4^{th} and 5^{th} particle. 17

Figure 6 (a) Finite element model of the 1D composite granular chain. Comparison of experimental and numerical results in (b) S-W and (c) W-S granular chains, respectively. 19

Figure 7 Typical results of wave propagation in 1D granular chains with core-shell particles ($\alpha = 0.1$). Contact force map: (a) S-W and (d) W-S; Wave properties: (b) S-W and (e) W-S; Stress distribution (the 2^{nd} and 3^{rd} particles): (c) S-W and (f) W-S. 22

Figure 8 Numerical results (solid symbols) and theoretical prediction (cross symbols) of solitary wave speed variation as a function of α: (a) S-W (blue) and W-S (green) composite granular chains. (b) Illustration of interaction between two neighboring composite particles..... 23

Figure 9 S-W: the deformation waveforms upon (a) $\alpha = 5$, (b) $\alpha = 1$, (c) $\alpha = 0.1$, (d) $\alpha = 0.02$. The blue and gray parts represent strong and weak materials, respectively. 28

Figure 10 W-S: the deformation waveforms upon (a) $\alpha = 5$, (b) $\alpha = 1$, (c) $\alpha = 0.1$, (d) $\alpha = 0.02$ 29

Figure 11 Wave properties in 1D composite granular chains with sandwich particles. The varying trend of wave speed with respect to α^*: (a) S-W-S and (b) W-S-W configurations. (c) A lumped mass-nonlinear spring model describing more generalized 1D granular systems. 31

Figure 12 S-W-S: the deformation waveforms upon (a) $\alpha^*=5$, (b) $\alpha^*=0.5$, (c) $\alpha^*=0.1$, (d) $\alpha^*=0.05$. 32

Figure 13 W-S-W: the deformation waveforms upon (a) $\alpha^*=5$, (b) $\alpha^*=0.5$, (c) $\alpha^*=0.1$, (d) $\alpha^*=0.05$. 33

Figure 14 Experimental setups. (a) Overall configuration of a horizontal test platform for 1D spherical granular crystal; (b) Schematic of the film sensor structure; (c) Experimental setup for 1D granular chain consisting of *N* beads, where film sensor was embedded in the bead to obtain the compression force..... 43

Figure 15 Finite element model of 1D spherical granular chain. Impact pulses were generated with a striker under different impact velocities. 46

Figure 16 Comparison of force-time responses of (a) (c) experiments and (b) (d) finite element analysis of Nesterenko solitary wave. Herein, (a) and (b) are results of 1D stainless steel granular chain with an impact velocity of 0.3 m/s, while (c) and (d) are results of 1D nylon granular chain with an impact velocity of 1.654 m/s. The curves in group A and group B show the responses of 5^{th} particle and 10^{th} particle in the 1D granular chain, respectively 47

Figure 17 Repeated testing results of three types of granular systems under different impact velocities. (a)-(c) Stainless steel; (d)-(f) Brass; (g)-(i) Aluminum 48

Figure 18 Mechanism maps of equivalent systems. (a) A comprehensive map indicating the normalized properties of Nesterenko solitary waves and granular chains, together with the distribution of equivalent systems and (b) An instructive map to design a granular system. The circle symbols are four selected groups of generalized equivalent systems from specific lines with identical λ. 50

Figure 19 Experimental results of generalized equivalent systems. Force-time curves of 5^{th} and 10^{th} particles in (a) 1D brass granular chain and (b) 1D stainless steel granular chain at three different impact velocities (0.3 m/s, 0.4 m/s, 0.5 m/s)..... 52

Figure 20 Numerical results (particle velocity-time curve) of generalized equivalent systems. (a) Group 1; (b) Group 2; (c) Group 3; (d) Group 4. 53

Figure 21 Experimental results of restricted equivalent systems. Force-time curves of 5^{th} and 10^{th} particles in (a) 1D stainless steel granular chain and (b) 1D aluminum granular chain at three different impact velocities (0.3 m/s, 0.4 m/s, 0.5 m/s) 54

Figure 22 Numerical results (particle velocity-time curve) of restricted equivalent systems. (a) Group 1; (b) Group 2; (c) Group 3; (d) Group 4. 55

Figure 23 Schematic of setups. (a) Experimental setups of the proposed 1D HC granular chain. (b) Experimental setups and FE models were developed to investigate the contact properties between HC particles. A 3D-printed cubic box was adopted to keep two HC particles vertically aligned in experiments. (c) FE model of the 1D HC granular chain, which is consistent with the settings in experiments. 62

Figure 24 Typical results. (a) Contact behaviors of HC granular crystals ($2R$ = 19.05 mm, R/t = 5.77). A 3D-printed box was applied to ensure purely vertical displacement during the experiments. (b) Validation of the FE granular chain model. Contact forces at four different positions (i.e., the 1st and 2nd particles, the 3rd and 4th particles, the 6th and 7th particles, the 8th and 9th particles) obtained from the experiment and numerical simulation are compared. (c) Particle force and (d) Nondimensional kinetic energy maps in time and space domains from the numerical simulation. The red dashed and white dotted lines represent the wave peak and front edge of the stress wave during the propagation process, respectively. 64

Figure 25 Effects of impact velocities. (a) Definitions of characteristic parameters in stress wave propagation. (b) Wave width variation in space domain under different impact velocities. The inset shows wave speeds of different cases. (c) The geometry of the contact region corresponding to two contact types: point contact (sphere-to-sphere) and line contact (cylinder-to-cylinder). 67

Figure 26 Contact forces of different particles (R/t = 20, M/m = 1, N = 20) illustrate stress wave propagation under the impact velocity of (a) 0.1 m/s, (b) 0.5 m/s and (c) 1 m/s. Nondimensional kinetic energy maps were plotted to investigate energy transmission in HC granular chains under different impact velocities: (d) 0.1 m/s, (e) 0.5 m/s, and (f) 1 m/s. The input energies of each system, i.e., the initial kinetic energy of the impactor, were marked by white circles in the energy maps. 71

Figure 27 The evolution of leading waveforms at different spatial positions (R/t = 20, V_i = 0.1 m/s, N = 20): (a) N = 3, (b) N = 6, (c) N = 9, (d) N = 12. The normalized force (F/F_{max}) is plotted versus nondimensional time ($V_sT/2R$) and the right halves of the curves have been shifted to the origin for comparison. 73

Figure 28 Contact behaviors of HC granular crystals with a thickness ratio R/t varying from 1 to 20. The behaviors of HC granular chains can switch from strain-hardening to softening based on different values of exponent n. Four thickness ratios (R/t = 2, 4, 16, 20, star markers in the graph) were selected to investigate the tunable wave properties. 75

Figure 29 Wave propagation in 1D HC granular chains with different thickness ratios (M/m = *1*, V_i = 1 m/s, N = 20): (a) R/t = 2, (b) R/t = 4, (c) R/t = 16, (d) R/t = 20. 76

Figure 30 Effects of thickness ratios. (a) The nondimensional kinetic energy of particles with different thickness ratios. Three positions (1st, 6th, and 10th) were considered. Wave widths of 1D HC granular chains with (b) low and (c) high thickness ratios. 77

Figure 31 Effects of particle numbers. A 1D HC granular chain ($R/t = 20$, $M/m = 1$, $V_i = 0.1$ m/s) with particle number $N = 50$ was considered. (a) Force mitigation (defined as F_{Nm}/F_{1m}) decreases as the stress wave propagates. (b) Specific force mitigation variation shows that good specific mitigation results can be achieved within a very short chain (~5.46 particles in this case). 78

Figure 32 (a) Fabrication process of a single kirigami lantern; (b) Schematic of the setup for impact experiments. An expand screw was inserted into the top of two supports to fix the round shaft. Four unthreaded holes were designed at the base to secure the supports on the optical table. Both the cubic impactor and kirigami lanterns can freely slide along the shaft; (c) Cyclic tests on kirigami lanterns for preconditioning. 82

Figure 33 (a) Experimental setup captured by the high-speed camera; (b) FE model; (c) Quasi-static tensile testing of the watercolor paper specimens used in fabrication. Young's modulus and yield strength can be obtained from the elastic stage and 0.2% plastic strain offset respectively; (d) Comparison of the maximum nominal strain between experimental and numerical results; Deformation modes from the (e) experiment and (f) simulation.. 85

Figure 34 (a) Definition of transmission ratio; (b) Acceleration (normalized by the maximum input acceleration) of input and output waves under impact energy of 1.6 J (corresponding to an impact velocity of 21.17 m/s); (c) Comparison of transmission ratio of the kirigami lantern chain (KLc) with existing structures from previous publications (The impact energy is 1.6 J). Note that an axis break is added at 7.9% due to the large difference between the transmission values of the structures. 88

Figure 35 The effect of impact energy. (a) The variation of transmission as impact energy increases from 0.13 J to 1.60 J. The insets exhibit the deformation modes of the 1st and 2nd kirigami cells at ξ_m during the stress wave propagation. (b) The evolution of ξ_m with respect to unit index under different impact energies. 90

Figure 36 The evolution of nominal strain in the first four kirigami lanterns during stress wave propagation. (a) $N = 1$; (b) $N = 2$; (c) $N = 3$; (d) $N = 4$. 93

Figure 37 Comparison of (a) transmission, wave width, normalized input amplitude, and (b) maximum strain of the kirigami chains with different cell numbers. (c) Deformation modes of the kirigami lantern chain with 20 cells at different times (From top to the bottom: 4 ms, 12 ms, and 20 ms). 94

Figure 38 Comparison of (a) transmission, wave width, normalized input amplitude, and (b) maximum nominal strain of the kirigami chains with different petal numbers. 96

Figure 39 Configuration of kirigami cells with different hinge numbers (N_h): (a) $N_h = 1$; (b) $N_h = 2$; (c) $N_h = 3$. (d) Comparison of transmission (blue columns) and mass of unit cell (yellow columns) in kirigami chains with different N_h. 98

Figure 40 (a) Wave width and normalized input of the kirigami chains with different N_h. (b) The evolution of the maximum nominal strain of the kirigami chains during stress wave propagation. 99

Figure 41 Configurations of the proposed solitary wave tuning strategies and a three-dimensional FE model of the cylindrical granular chain. Parts 1, 2, and 3 represent the launching part, tuning part and receiving part, respectively. Two distinct types of interfaces, "strong-weak" and "weak-strong", are marked as black dashed lines accordingly. 102

Figure 42 (a) Schematic and (b) actual **e**xperimental setups. 3D-printed enclosures (Formlabs, Form 2) were assembled to serve as a guide for the cylindrical granular chain, and the guide was fixed to an optical table with vibration isolation. The contact area between particles and enclosures is highlighted in the top view of the enclosure. An electromagnet was fixed to a 3D-printed holder for releasing the impactor, and an optical sensor served as an external trigger, ensuring that each test had an identical initial condition. A film sensor was inserted into two different positions in launching part and receiving part (i.e., between 1st and 2nd particles, 13th, and 14th particles), respectively. The effect of thickness and mass of the film sensor can be neglected compared to particles in the granular chain [79]. 105

Figure 43 Validation of the FE model by comparing the contact force profiles from experiments and simulations. The frictional effect in experiments is included by introducing a mild frictional coefficient (f) in interaction properties. (a) Configuration 1: $f = 0.05$; (b) Configuration 2: $f = 0.01$; (c) Configurations 3: $f = 0.02$; (d) Configuration 4: $f = 0.02$; (e) Configuration 5: $f = 0.02$. 107

Figure 44 Typical results of the mass mismatch strategy. (a) The evolution of contact forces from different particles as stress waves propagate ($m_{1,3} / m_2 = 4$); (b) Compression ratios under various mass ratios. 109

Figure 45 (a) Typical results of the modulus mismatch strategy ($E_{1,3} / E_2 = 10$); (b) Compression ratios under various modulus ratios. 110

Figure 46 (a) Typical results of the thickness mismatch strategy ($t_{1,3} / t_2 = 2.67$); (b) Compression ratios under various thickness ratios. 110

Figure 47 Maps of compression ratios obtained from Type I coupling strategies. (a) Mass-modulus mismatch, (b) mass-thickness mismatch, (c) modulus-thickness mismatch. 113

Figure 48 (a) Typical results of Type II coupling strategy ($m_{1,3} / m_2 = 2$, $E_{1,3} / E_2 = 5$, $t_{1,3} / t_2 = 1.33$); (b) Compression ratio maps corresponding to different mass, modulus, and

thickness ratios. 114

Figure 49 (a) Configuration of the two-layer granular chain. Typical results of two-layer granular chains with (b) mass mismatch ($m_{1,3,5}$ / $m_{2,4}$ = 5), (c) modulus mismatch ($E_{1,3,5}$ / $E_{2,4}$ = 10), and thickness mismatch (d) $t_{1,3,5}$ / $t_{2,4}$ = 1.33, (e) $t_{1,3,5}$ / $t_{2,4}$ = 2.67. 115

Figure 50 Compression ratios of two-layer granular chains with (a) mass mismatch, (b) modulus mismatch, and (c) thickness mismatch. 117

Figure 51 Compression ratios of two-layer granular chains with Type I coupling strategies. (a) Mass-modulus, (b) mass-thickness, (c) modulus-thickness. 118

Figure 52 Informative map of materials for the tuning part corresponding to specific compression ratios. 119

Figure 53 Comparison of waveforms at different locations of an S-W composite chain. Note that the x-axis is shifted for a better comparison. 131

Figure 54 Validation of the power contact law based on a compressive test of two W-S particles 132

Figure 55 Mesh size convergence study of the equivalent systems: five gradient mesh sizes (0.02~2 mm, 0.05~2 mm, 0.1~2 mm, 0.2~2 mm, 0.5~2 mm) were considered. 133

Figure 56 The numerical results of contact force-time curves (the left and right curves in solid line) and average force-time curve (the central curve in dot line), which is also used to obtain the numerical coefficient β representing the ratio of the dynamic contact force between two particles to the maximum dynamic compression force in the center of the given particle. 135

Figure 57 The effect of tiny gap on stress wave propagation within spherical granular chain. 136

Figure 58 Spherical granular chain model with tube guide. 137

Figure 59 The effect of friction on stress wave propagation within spherical granular chain 137

Figure 60 Wave transmissions in two types of equivalent systems: (a) Generalized equivalent system: stainless and brass; (b) Restricted equivalent systems: Nickel and Titanium 138

Figure 61 The methodology to obtain waveforms in granular chain tests. (a) The original waveforms from channels 1 (the film sensor) and 2 (the photoelectric sensor). A relative time (t*) is measured to determine the actual time difference between the two tests given two different positions of the film sensor. (b) The desired waveforms after translation. 139

Figure 62 Mesh size convergence study. Six mesh sizes are considered (0.5 mm, 0.8 mm,

1.0 mm, 2.0 mm, 3.0 mm, and 5.0 mm) and two groups of contact force (F_4 and F_8) are compared. 140

Figure 63 The effect of gravity. The evolution of the contact force was compared upon a specific case ($R/t = 20$, $V_i = 0.1$ m/s, $N = 20$, $M/m = 1$) with and without gravity, respectively. Two regions (regions I and II) were obtained given the gravitational effects on the granular chain. 141

Figure 64 The investigation on elastic assumption. (a) A critical granular chain ($R/t = 20$, $N = 20$), where the 1st cylindrical particle is selected to investigate its response during the stress wave propagation. (b) The maximum Mises stress of the 1st cylindrical particle in three critical loading scenarios. (c) The definition of equivalent deformation of the 1st cylindrical particle. (d) The evolution of equivalent deformations obtained from the 1st cylindrical particle in different loading scenarios displayed in (b). 143

Figure 65 The demonstration of existing results under an impact velocity of 10 m/s. (a) Contact forces of different particles ($R/t = 20$, $M/m = 1$, $N = 20$). (b) Wave width variation in space domain under different impact velocities (i.e., 0.1 m/s, 1 m/s and 10 m/s). The inset shows wave speeds of corresponding cases. 144

Figure 66 Demonstration of the reusability via five repeated impacts in experiments .. 146

NOMENCLATURE

Nomenclature

F	Contact force	$V_{s,r}$	Rarefaction solitary wave speed
R	Radius	κ	Viscous coefficient
x	Coordinate of the particle	χ	Dissipative exponent
A	Material-related coefficient	α	The ratio of core radius and shell thickness in a core-shell particle
E	Young's modulus	t	Thickness
L_c	The spatial characteristic length of the wave	α^*	The ratio of interlayer thickness and core radius
v	Poisson's ratio	l	Length of the particle
u	Displacement of the particle	L_s	Wave width
m	Particle mass	F_m	Force amplitude
ρ	Density	V	Wave speed
ξ_{min}	Minimal strain	T	Waveform duration
a	Diameter of the particle	d	Deformation
V_s	Solitary wave speed	γ_s	Shear strain
ξ_i	Infinity strain	E_e	Effective modulus
ξ_m	Strain amplitude	$f_c(\alpha)$	Governing coefficient of core
v_p	Particle velocity	$\bar{x}$	Nondimensional coordinate
v_m	The amplitude of particle velocity	$\bar{t}$	Nondimensional time
$f_s(\alpha)$	Governing coefficient of shell	ξ_0	Initial strain
s_1	Modulus mismatch ratio of core and shell materials	$\tilde{\lambda}$	Nondimensional material-related coefficient
δ_0	Static displacement	A_0	Constant
m_t	Total mass	p	Constant
s_2	Density mismatch ratio of core and shell materials	$\tilde{\gamma}$	Nondimensional damping coefficient
S	Constant	n	Nonlinear exponent
ξ	Strain	ω	Constant
λ	Material-related coefficient	c	1D elastic wave speed

$V(t)$	The phase speed of wave subjected to weak dissipation	$A(t)$	The amplitude of wave subjected to weak dissipation
γ	Damping coefficient	E_p	Potential energy
t_c	The characteristic time of contact deformation	$\bar{V}_s$	The nondimensional phase speed of solitary waves
T_c	Characteristic period of grain oscillations	$\bar{v}_m$	Nondimensional maximum particle velocity
$\bar{u}$	Nondimensional displacement	E_k	Kinetic energy
K_s	Sensitivity of film sensor	E_t	Total energy
O	Output voltage per unit of amplifier	E_k^{Central}	The kinetic energy of the central particle in a hump
K_a	Sensitivity of amplifier	$\bar{v}_i$	Normalized impact velocity
U	Output voltage	N	Unit cell number in a chain
$\bar{R}$	Normalized radius	τ	Unit time
ΔT	The interval between two specific peaks	q	Half-length of the rectangular contact area
μ_0	Fitting constant	k	Contact coefficient
V_i	Impact velocity	M	Impactor mass
KE*	Nondimensional kinetic energy	KE_m	Maximum kinetic energy
V_Y	Yield velocity	Y_c	Yield strength
T_s	Temporal width	w	Fitting constant
$p(x, y)$	Pressure distribution in plane xy	P	Load
L_a	Major semi-axis of the elliptical contact area	L_b	Minor semi-axis of the elliptical contact area
H	Height	$\bar{P}$	Load per unit
f	Frictional coefficient	μ	Force mitigation ratio
y	Fitting constant	μ^*	Specific force mitigation ratio
z	Fitting constant	B	Fitting constant
α_c	Compression ratio	b	Fitting constant
$F_{m,e}$	Force captured by the sensor	β	Coefficient
F_0	Pre-compression force	t^*	Relative time
L_0	Original length	h	Cutting length
OD	Outer diameter	ID	Inner diameter
N_h	Hinge number	L	Length

CHAPTER 1 INTRODUCTION

1D granular systems composed of tightly packed particles are among the simplest and standout candidates for shaping our understanding of wave dynamics and providing an enormous landscape of exotic physical phenomena [1-6]. Originated from the exact nature of dispersion and nonlinearity, 1D granular systems possess the unique capability of supporting various novel waves (e.g., traveling solitary waves [7-10], dispersive shock waves [11, 12]). Yet, the wave behaviors heavily depend on the contact properties between elastically interacting particles [1, 13]. The effective contact stiffness can be tailored by modifying the material properties (e.g., Young's modulus) [14, 15] and the shapes of granular particles [16-18]. Furthermore, it is possible to efficiently control the nonlinearity of 1D granular systems from strongly nonlinear to almost linear by engineering the pre-compression to the system [8, 19, 20]. The fascinating dynamic responses and remarkable tunability make 1D granular systems potentially applicable for impact mitigation [21-24], waveguide [25], acoustic switch [26, 27], nondestructive testing [28-30], vibration suppression [31, 32], and sound scramblers [14, 33].

In the following review, the analytical model of 1D granular systems will be first introduced. Next, strongly nonlinear solitary waves in a series of 1D granular systems will be presented, where representative experimental techniques and numerical methods will be discussed. Finally, the stress wave attenuation in 1D granular systems will be illustrated.

1.1 Analytical model of 1D granular systems

Given a granular chain consisting of coherent spheres with no pre-compression (i.e., the state of "Sonic Vacuum" [34]), Nesterenko first developed a simple analytical solution to describe the propagation of the strongly nonlinear solitary wave (also called Nesterenko solitary wave) [1, 19, 35] that was different from the traditional solitons supported by Korteweg–de Vries (KdV) equation [36, 37]. The schematic of compressed spheres in Sonic Vacuum subjected to impulsive loadings is presented in Fig. 1(a), where the interaction of neighboring particles is governed by Hertz's contact law [38]:

$$F = A\left[\left(R_{i-1} + R_i\right) - \left(x_i - x_{i-1}\right)\right]^{3/2}, \tag{1}$$

where F is the contact force between particles, $R_{i\text{-}1}$ and R_i are the radii of spherical particles, $x_{i\text{-}1}$ and x_i are the coordinates of the sphere centers, and A is a material-related coefficient that can be expressed by [39]

$$A = \frac{4E_{i-1}E_i}{3E_i\left(1-v_{i-1}^2\right) + 3E_{i-1}\left(1-v_i^2\right)}\left(\frac{R_{i-1}R_i}{R_{i-1}+R_i}\right)^{1/2}. \tag{2}$$

Here, $E_{i\text{-}1}$ and E_i are Young's moduli of spherical particles, $v_{i\text{-}1}$ and v_i are Poisson's ratios. It is necessary to point out that the Hertzian interaction is valid only if neighboring particles are in contact and overlap with each other. Also, Hertz's contact law can be extended to a more generalized power contact law by considering different types of granular particles [1, 40, 41]:

$$F = A\left[\left(R_{i-1} + R_i\right) - \left(x_i - x_{i-1}\right)\right]^n, \tag{3}$$

where the nonlinear exponent n is greatly dependent on the contact geometry between interacting particles. For instance, the exponent n varies with the thickness of hollow spherical particles and can be larger than 3/2 [17]. Furthermore, the exponent n of interacting cylindrical particles can be effectively tuned by modifying the contact angle [42, 43]. Cylindrical particles aligned in perpendicular have an exponent of $n = 3/2$, yet the exponent is quite close to unity ($n = 10/9$) when they are in parallel [44], which corresponds to line contact.

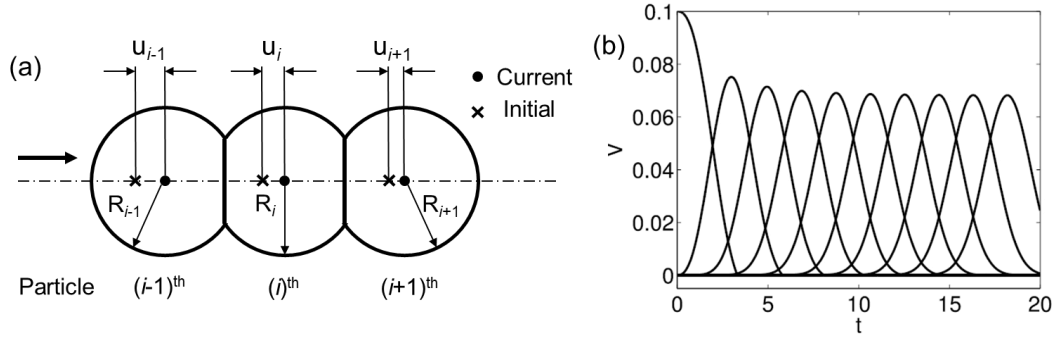

Figure 1 (a) Schematics of compressed particles in 1D spherical granular chains subjected to impulsive loadings, where u_i and x_i denote the displacement and coordinate of the i^{th} particle, respectively. The cross symbol is the original position of particle centers, while the solid circle represents the current position of particle centers. (b) An example of strongly nonlinear solitary waves in a monomer granular chain [39].

For 1D monoatomic spherical granular chains, the equation of motion for the i^{th} particle is given by

$$\ddot{u}_i = K\left[\left(u_{i-1} - u_i\right)^{3/2} - \left(u_i - u_{i+1}\right)^{3/2}\right],\ K = \frac{E(2R)^{1/2}}{3\left(1-\nu^2\right)m},\ m = \frac{4}{3}\pi R^3 \rho\,, \tag{4}$$

where m is the mass of the spherical particle and ρ is the density of particle material.

To explicitly solve Eq. (4), Nesterenko introduced an equivalent partial differential equation (PDE) based on a long-wavelength approximation where $L_c >> a = 2R$ (L_c is the spatial characteristic length of the wave) [1, 45]. Accordingly, the wave equation for "Sonic Vacuum" is obtained [1]

$$\ddot{u} = c^2\left[\frac{3}{2}\left(-u_x\right)^{1/2}u_{xx} + \frac{a^2}{8}\left(-u_x\right)^{1/2}u_{xxxx} - \frac{a^2}{8}\frac{u_{xx}u_{xxx}}{\left(-u_x\right)^{1/2}} - \frac{a^2}{64}\frac{\left(u_{xx}\right)^3}{\left(-u_x\right)^{3/2}}\right],$$
$$-u_x > 0\,,\quad c^2 = \frac{2E}{\pi\rho\left(1-\nu^2\right)} = Ka^{5/2}. \tag{5}$$

Additional transformations are made by introducing dimensionless variables to derive a general stationary solution of the wave equation, yielding the nonlinear dependence of solitary wave speed (V_s) on the infinity strain (ξ_i) and strain amplitude (ξ_m) [1]:

$$V_s = \frac{c}{\left(\xi_m - \xi_i\right)}\left\{\frac{2}{5}\left[3\xi_i^{5/2} + 2\xi_m^{5/2} - 5\xi_i^{3/2}\xi_m\right]\right\}^{1/2}. \tag{6}$$

The corresponding strain and particle velocity are

$$\xi = \left(\frac{5V_s^2}{4c^2}\right)^2\cos^4\left(\frac{\sqrt{10}}{5a}x\right), \tag{7}$$

and

$$v_p = V_s\left(\frac{5V_s^2}{4c^2}\right)^2\cos^4\left(\frac{\sqrt{10}}{5a}x\right). \tag{8}$$

Therefore, the characteristic length L can be given by the period of the solutions in

Eq. (7) [1]

$$L = \left(\frac{5a}{\sqrt{10}} \right) \pi \approx 5a \, . \tag{9}$$

An example of strongly nonlinear solitary waves in a monomer granular chain is presented in Fig. 1(b). Herein, a finite spatial length of five spherical particles ($5a$) is obtained in Nesterenko solitary waves, which is fundamentally different from that of KdV waves [7]. Another unique feature of Nesterenko solitary waves is that the wave speed is nonlinearly dependent on the amplitude of particle velocity v_m (or strain amplitude ξ_m):

$$V_s = \frac{2}{\sqrt{5}} c \xi_m^{1/4} = \left(\frac{16}{25} \right)^{1/5} c^{4/5} v_m^{1/5} . \tag{10}$$

For more general 1D granular systems in which neighboring particles are governed by a power contact law shown in Eq. (3), similar waves are observed in strain-hardening materials ($n > 1$) yet rarefaction waves appear in strain-softening materials ($n < 1$) [46, 47]. Following a similar continuum approximation, stationary solutions of compression solitary waves in strain-hardening materials lead to [48, 49]

$$L = \frac{\pi a}{n-1} \sqrt{\frac{n(n+1)}{6}} \tag{11}$$

and

$$V_s = c \sqrt{\frac{2}{n+1}} \xi_m^{\frac{(n-1)}{2}} = \left(\frac{2c^2}{n+1} \right)^{\frac{1}{(n+1)}} v_m^{\frac{(n-1)}{(n+1)}} . \tag{12}$$

Note that the above stationary solution is valid even if the power-law material is

approaching a linear contact ($n = 1 + r$, $r << 1$ [50]) or the exponent is rather large ($n >> 1$ [51, 52]). Rather than compression solitary waves, rarefaction solitary waves with expanded waveforms propagate in strain-softening granular systems where abnormal behaviors are observed under compression [33, 40]. Also, the rarefaction solitary wave speed $V_{s,r}$ nonlinearly depends on the strain [1]:

$$V_{s,r} = \frac{c}{\left(\xi_i - \xi_{\min}\right)} \left\{ \frac{2\left[p\xi_i^{n+1} + \xi_{\min}^{n+1} - \left(n+1\right)\xi_i^n \xi_{\min} \right]}{\left(n+1\right)} \right\}^{1/2}. \tag{13}$$

Significantly, there is no smooth transition between strain-hardening and strain-softening materials since no stationary solitary solution can be derived for an ideal linear contact (i.e., $n = 1$). Therefore, it is essential to investigate wave dynamics in 1D granular systems with the exponent being very close to 1 (e.g., cylinders in parallel). Furthermore, one may fundamentally broaden the tunability of 1D granular systems if a switch from strain-hardening to strain-softening behaviors can be achieved.

1.2 Strongly nonlinear solitary waves in 1D granular systems

The analytical model of strongly nonlinear solitary waves was subsequently demonstrated by both numerical and experimental studies [7, 8, 53, 54], leading to an explosion of interest in nonlinear wave dynamics of granular systems [55-57]. Most of the studies in this active domain focused on macroscale granular systems where the dimension of granular particles is within the millimeter to centimeter range. A variety of particle

shapes (e.g., sphere [58], hollow sphere [59], cylinder [21, 42], hollow cylinder [50], ellipsoid [16]) and materials (e.g., stainless-steel [60], brass [61], aluminum [62], glass [63], Teflon [14], nylon [13, 63], rubber [64]) have been investigated accordingly, where the nonlinearity of the granular systems can be effectively tuned via pre-compression [19]. By applying a material or geometric mismatch between neighboring particles, one may anticipate extended nonlinear wave dynamics in 1D heterogeneous granular systems (i.e., configurations with defects [58, 65], dimer [15], and trimer chains [66]).

More recently, strongly nonlinear solitary waves have been experimentally discovered in 1D microscopic granular chains [67]. A natural attempt was then made at the nanoscale, where the effect of surface geometry on nanoparticle collisions was systematically investigated, including facets, sharp crystal edges, and amorphous surfaces of nanoparticles ($R < 10$ nm) [68]. The results show that both the edge and amorphous surface contact match with the prediction of Hertz contact law, making it possible to discover novel dynamic phenomena in granular systems at the nanoscale [69]. Accordingly, numerical investigations were made to a series of nano granular systems (e.g., buckyball and nanogold systems [70-72]), which further demonstrates the formation, propagation, and tunability of strongly nonlinear solitary waves in small scales.

A typical experimental setup to investigate strongly nonlinear solitary waves in 1D granular systems can be developed based on an optical table with vibration isolation (Figs.

2(a)-(b)). Major components include an impactor or actuator for generating impulses, a sliding rail for aligning particles, sensors for capturing the propagating stress waves, and an oscilloscope for recording digital data and visualizing waveforms [73]. Specifically, the impulse amplitude and duration can be tailored by modifying the impact velocity and applying impactors with different mass properties, respectively [74]. According to customized requirements, the sliding rail can be either vertical (Fig. 2(a)) or horizontal (Fig. 2(b)), yet the vertical trail may bring about non-uniform pre-compression due to gravitational effect [20, 75]. For waveform detection, piezoelectric transducers (or film sensors) are mostly embedded in selected particles [76] or inserted between neighboring particles [21]. The nonuniformity between the measured particles and other particles in the granular chain is usually neglected due to the minor mass discrepancy [14].

In recent years, researchers have applied a series of novel experimental techniques to achieve higher accuracy and continuous measurements. For instance, the application of a laser Doppler vibrometer (LDV) makes it possible to measure the velocity and displacement of each particle in a non-contact way (Fig. 2(c)), where a full map of the wave dynamics can be obtained [43, 77]. Furthermore, a high-speed camera can continuously monitor and record the detailed dynamic responses of the granular systems during stress wave propagation [59, 78] (Fig. 2(d)).

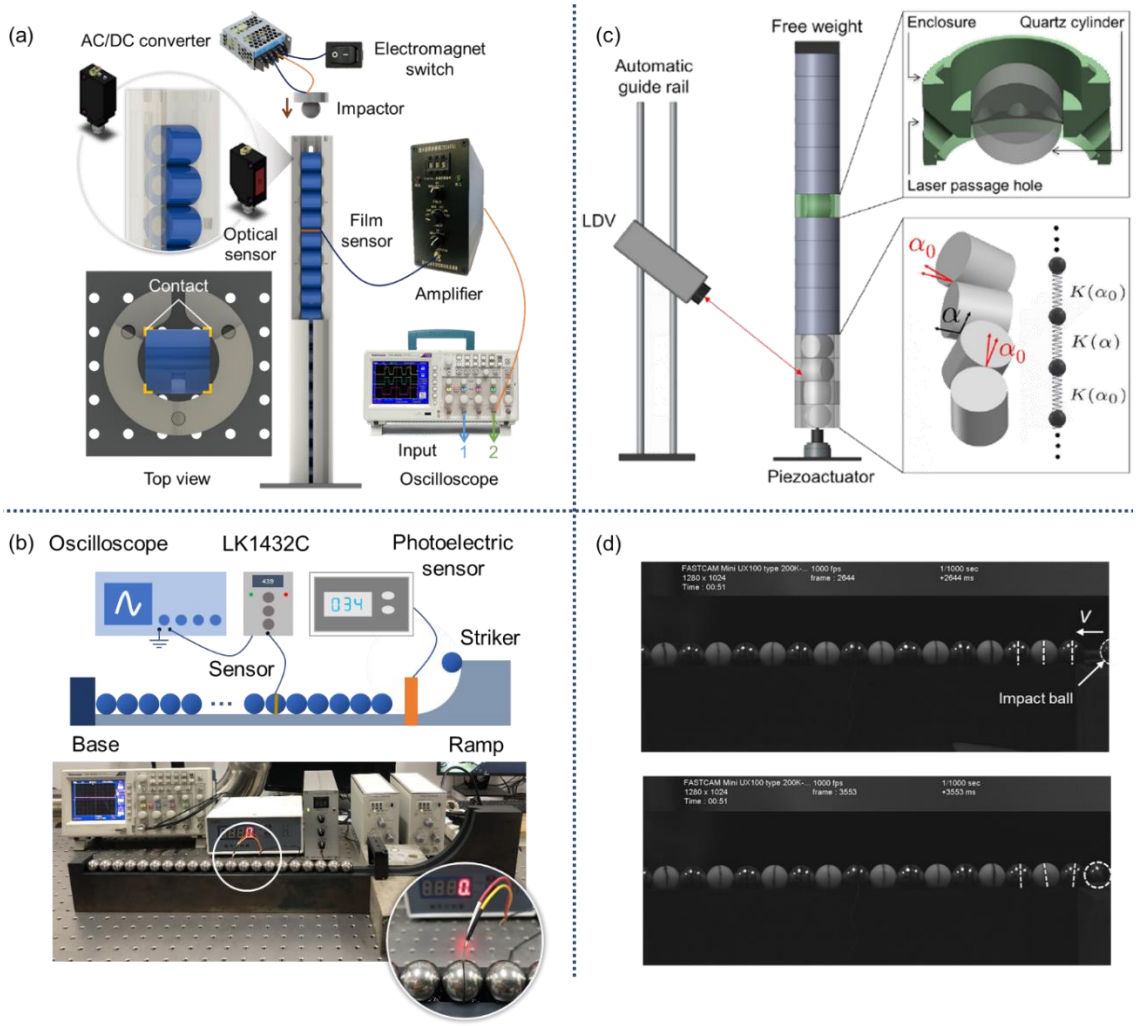

Figure 2. Experimental techniques: typical experimental setups with (a) vertical [79] and (b) horizontal sliding rails [13]; (c) schematic of a laser Doppler vibrometer measuring systems [43]; (d) dynamic responses of spherical granular particles monitored by a high-speed camera [59].

The fundamental problem of wave propagation is to solve the corresponding PDEs (i.e., wave equation) based on different configurations, boundary conditions, and initial conditions. Therefore, numerical methods can be highly efficient to explore wave behaviors in 1D granular systems. The discrete element method (DEM) and finite element

method (FEM) are commonly applied to 1D granular systems at the microscale and macroscale [5, 80-82]. Moreover, the molecular dynamics (MD) simulation, a widely accepted method for analyzing the physical movements of particles, has been also used to examine the dynamic responses of 1D granular systems at the nanoscale [70-72, 83, 84]. In DEM (Fig. 3(a)), neighboring particles are approximated as lumped mass connected by a nonlinear spring, where appropriate initial conditions and boundary conditions are selected according to specific loading scenarios [85]. Each particle is reduced to points with a single-degree-of-freedom (DOF), and the interaction between the particles is described by either Hertz contact law (Eq. (1)) or the power law (Eq. (3)) [86]. By solving the equations of motion, the dynamic responses of the system can be obtained accordingly [10].

Compared to the discrete method, FEM can provide more abundant information (e.g., localized stress and strain distribution). FE models of 1D granular systems are established per specific configurations and loading scenarios [87] (Fig. 3(b)), in which only elastic material properties are modeled [88]. Following the 1D assumption, all the lateral movements of particles are restricted, while the impactor with an exact initial velocity will hit the remaining granular chain to generate an impulse [13]. A frictionless surface-to-surface hard contact is used to describe the interaction between particles and the sliding rail [50]. Furthermore, a finer mesh is usually employed in the vicinity of the contact point

to precisely simulate the localized deformation [29]. Although a systematic methodology has been developed to study wave dynamics in 1D granular systems, the approach to achieve a controllable and quantitative tunability of wave propagation is still unclear.

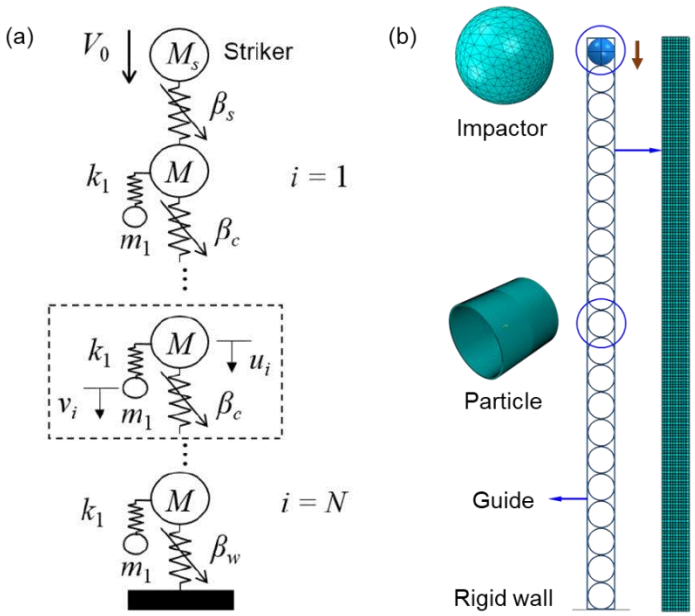

Figure 3 Numerical methods for exploring the wave behaviors in 1D granular systems. (a) Discrete element model of an elastic woodpile periodic structure [89]. (b) Finite element model of a hollow cylindrical granular chain [50].

1.3 Stress wave attenuation in 1D granular systems

Recent experimental observations of dissipative perturbations have brought forward new challenges on traditional wave dynamics, which motivates pioneers to investigate stress wave attenuation in 1D granular systems [9, 90] and in turn offers insights into designing the next generation mitigating systems. Despite a lack of a universally accepted model, primary efforts have been placed on exploring stress wave attenuation originated from friction between particles and the sliding rail [91], viscoelasticity of soft particles [92],

plastic deformation of granular particles [93-96], the viscous drag of liquid medium [97, 98], rotations of granular particles [78], and energy losses due to the randomness of aligned particles [55, 99, 100]. More recently, the dispersive rarefaction shocks have been discovered in a 3D-printed hollow elliptical cylinder chain as well, making it possible to achieve stress wave attenuation in strain-softening granular systems without material damping or plastic deformations [18].

The dissipation in stress wave propagation may result in the variation of both the amplitude and shape of the wave [11]. For example, a critical viscosity predicts the transition of shock wave profiles from oscillatory to monotonic (see the transition in Fig. 4(a)) [97], while the plastic deformation leads to qualitatively different wave profiles accompanied by a significant decrease of wave amplitude [101]. In addition to traditional testing platforms, a modified split Hopkinson pressure bar (SHPB) was applied to provide high amplitude loads for testing 1D granular systems (Fig. 4(b)) [22, 93, 95], where localized plastic deformations were observed near the contact point and the dissipation was obtained by measuring the residual plastic contact area.

Based on the extension of the Hertzian model in Eq. (1), a quantitative and systematic model of dissipation in 1D spherical granular chains was proposed by adding a phenomenological term in which a discrete Laplacian of the particle velocities was considered [11, 90]:

$$\ddot{u}_i = K\left[\left(u_{i-1}-u_i\right)^{3/2}-\left(u_i-u_{i+1}\right)^{3/2}\right]+\kappa s\left|\dot{u}_{i-1}-2\dot{u}_i+\dot{u}_{i+1}\right|^{\chi},$$
$$s \equiv \operatorname{sgn}\left(\dot{u}_{i-1}-2\dot{u}_i+\dot{u}_{i+1}\right) \tag{14}$$

where $\kappa<0$ is a viscous coefficient of the phenomenological force depending on the relative velocities of neighboring particles. A dissipative exponent of $\chi=1$ was demonstrated to be effective for dry granular matter [98], which was further optimized according to experimental and numerical results (Fig. 4(c)) [90].

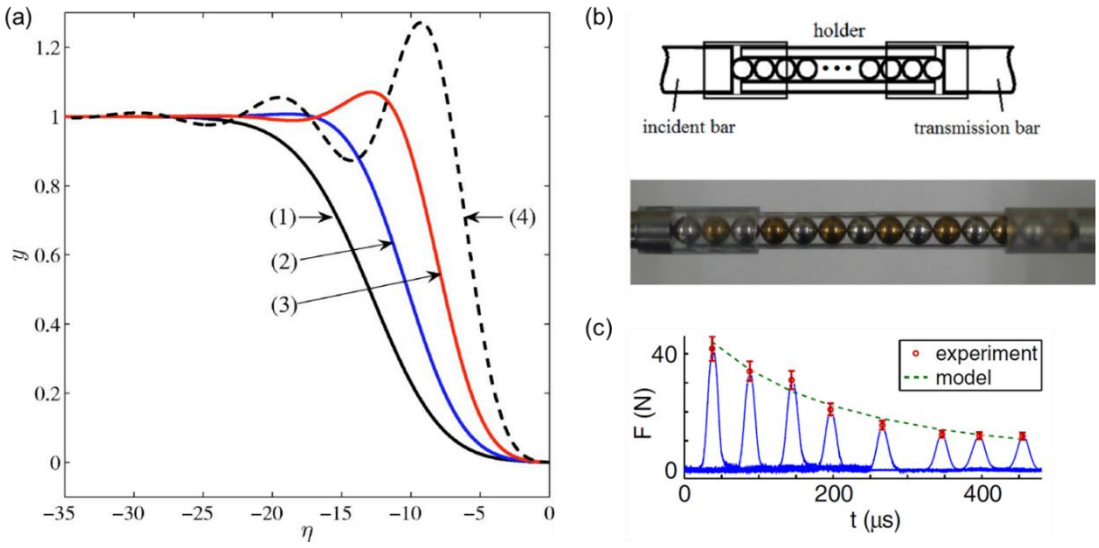

Figure 4 (a) Oscillatory and monotonic shock-like waves in a "Sonic Vacuum" [11]; (b) Experimental setups of a brass-steel dimer chain in SHPB [95]; (c) The comparison between the results from experiments and the dissipative model in a steel granular chain [90].

More complicated models involving both displacements and velocities were subsequently developed on the basis of the viscoelasticity theory [102]. Furthermore, a mesoscopic approach, including a three-dimensional (3D) FE model and a 1D regularized contact model, was established to explore the dissipative losses in 1D granular systems

from the perspective of first principles [103]. However, more sophisticated research is still in demand for uncovering the fundamental mechanisms of stress wave attenuation and realizing quantitative/controllable wave attenuation in 1D granular systems.

CHAPTER 2 SOLITARY WAVE PROPAGATION IN 1D GRANULAR SYSTEMS

In this chapter, the solitary wave propagation within 1D granular crystals based on composite cylinders is systematically investigated. Two types of composite particles are designed by creating a material mismatch within the granular, i.e., core-shell and sandwich types. Such 1D composite granular chains are found to support the formation of strongly nonlinear solitary waves, which is consistent with the observations of traditional 1D granular chains composed of spherical particles. An FE model is developed to describe wave propagation behaviors fully validated by experiments. A theoretical analysis is also conducted, which agrees with numerical results and uncovers the physical mechanisms of solitary wave propagation in 1D composite granular chains through the parametric study. Finally, the fundamental understanding of dynamic responses is extended to more generalized composite granular chains with sandwich configurations. Results provide in-depth physical understanding and engineering design guidance to quantitatively tailor wave properties through simple 1D granular structures.

2.1 Methods

2.1.1 Configurations

In this chapter, two types of composite particles are designed to form 1D cylindrical granular chains, including core-shell and sandwich structures (Fig. 5(a)). A material mismatch between different parts in a specific composite cylinder is created, where

stainless steel and nylon are selected as the “strong” and “weak” materials, respectively. Thus, two different configurations, i.e., “strong shell-weak core (S-W)” and “weak shell-strong core (W-S)”, are achieved for the core-shell type, where a critical parameter is defined based on the core radius *R* and shell thickness *t*, i.e., $\alpha = t / R$. Meanwhile, "strong shell-weak interlayer-strong core (S-W-S)" and “weak shell-strong interlayer-weak core (W-S-W)” configurations are obtained for the sandwich type. Accordingly, the geometric parameter is given by $\alpha^* = t_2 / R$, where t_2 is the interlayer thickness and the core radius is assumed the same as the shell thickness for simplification (i.e., $t_1 = R$). Note that the outer diameter (*a*) and length (*l*) is identical for all the particles (i.e., $a = 2(R + t) = l$).

2.1.2 Experimental setups

Herein, the fabrication approach of composite particles was developed (Fig. 5(b)). Firstly, short cylinders were cut from long rods/tubes for assembly. A PVC cover was employed to fill in the tiny gap between core and shell. Then, they were sealed and glued tightly. After over 24 h curing, the composite particles were completed and ready for testing.

To investigate the dynamic responses of 1D composite granular chains, a series of composite cylinders was vertically arranged in a 3D-printed guide (Fig. 5(c)), where the sliding track (see the top view of the guide) was delicately designed to minimize the contact areas that cause friction during the experiment.

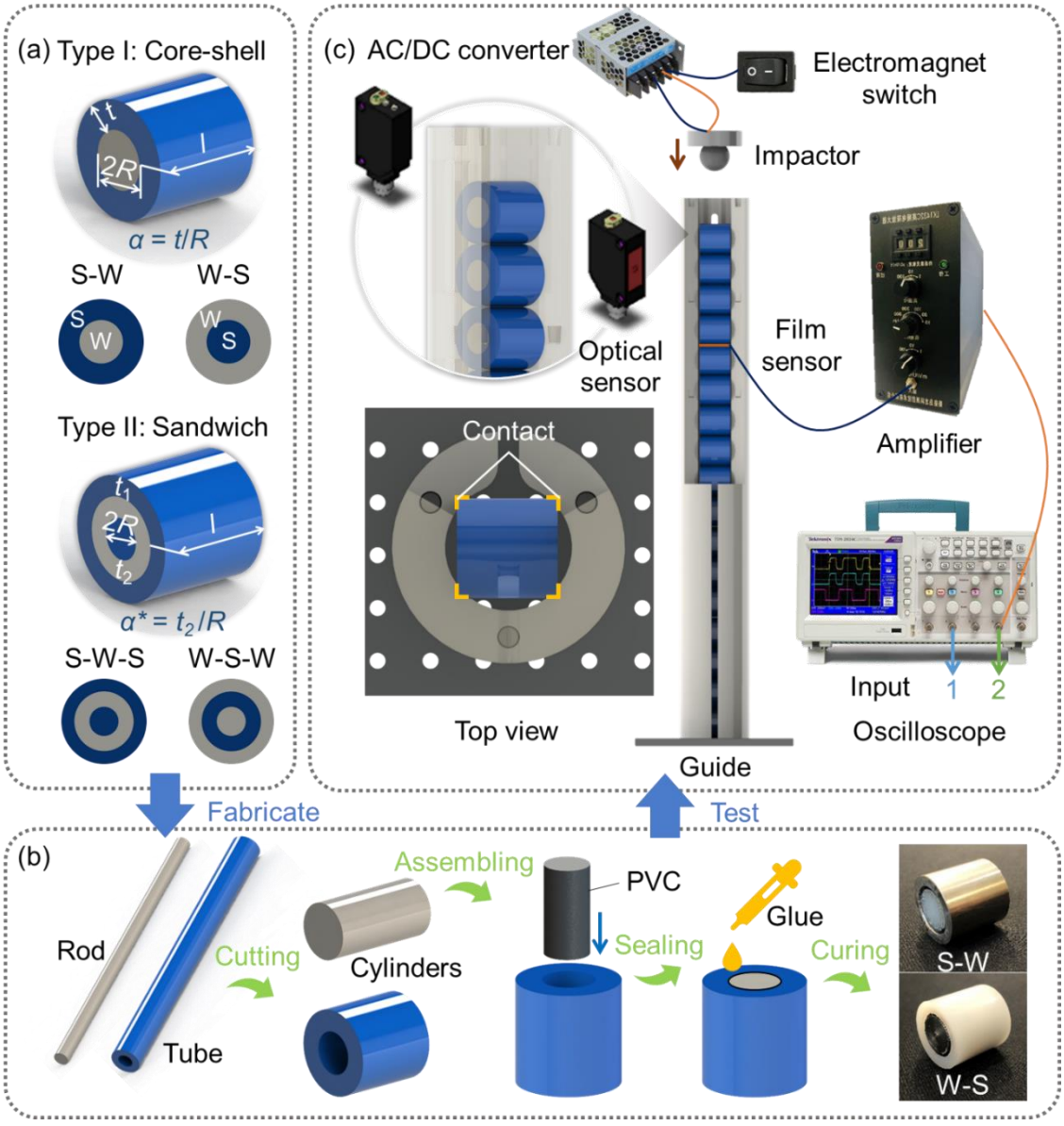

Figure 5 (a) Configuration of cylindrical composite particles. Type I: core-shell structure; Type II: sandwich structure. Schematic of (b) the particle fabrication process and (c) experimental setups. Herein, the contact force waveforms of two different locations were measured, i.e., the 1st and 2nd particle, the 4th and 5th particle.

Controlled by an electromagnet switch, a stainless-steel sphere with a diameter of 19.05 mm was released from an exact height, impacting the 1D composite granular chain

with a velocity of 0.63 m/s to generate an impulse. Meanwhile, the release of the impactor would trigger oppositely aligned photoelectrical sensors (OMRON, E3Z), serving as input 1 to the oscilloscope (i.e., trigger signal). Furthermore, a film sensor was inserted between different composite particles to capture the contact force waveforms during stress wave propagation. The corresponding signal (i.e., input 2) was captured by an amplifier (LK1432C), then visualized and recorded by the oscilloscope (Tektronix, TDS-2024C). More details about the experimental method and film sensor are available in Refs. [13, 50].

2.1.3 Finite element modeling

A three-dimensional FE model is established in ABAQUS/Explicit to explore wave properties in 1D composite granular chains (Fig. 6(a)). According to Ref. [50], only elastic properties are assigned for both materials, and the gravitational effect can be neglected. For stainless-steel, the density $\rho_s = 7800$ kg/m^3, Young's modulus E_s = 200 GPa, and Poisson's ratio v_s = 0.3. For nylon, the density $\rho_n = 1105$ kg/m^3, Young's modulus E_n = 3.55 GPa, and Poisson's ratio v_n = 0.42. All the composite particles possess the same outer diameter and length (i.e., $a = l$ = 19.05 mm), and their lateral movements are restricted by a rigid guide. For the parametric studies in the following sections, a stainless-steel sphere is applied to the granular chain with an initial velocity of 0.1 m/s to generate an impulse, and a rigid wall is fixed at the end of the chain.

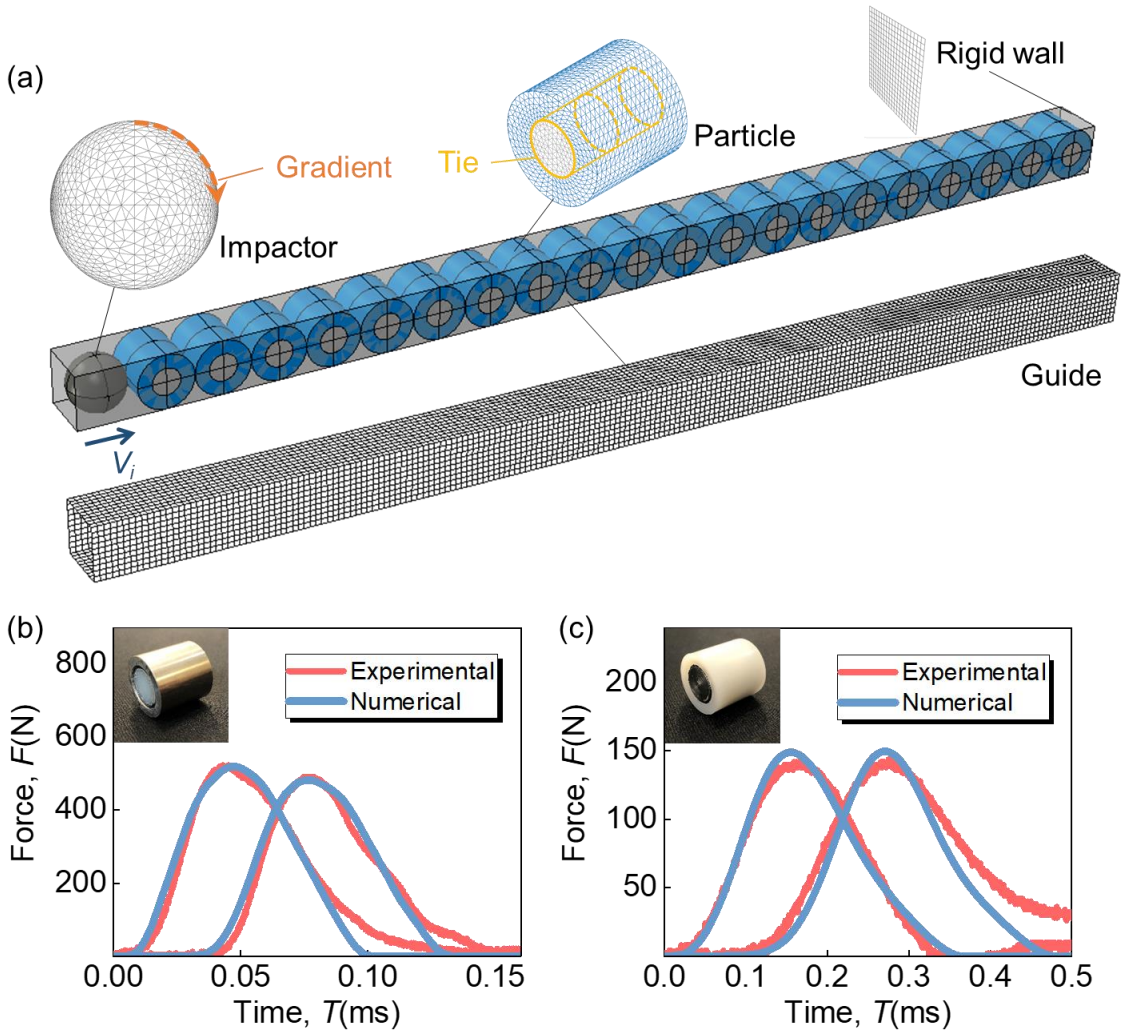

Figure 6 (a) Finite element model of the 1D composite granular chain. Comparison of experimental and numerical results in (b) S-W and (c) W-S granular chains, respectively.

Different parts within each of the composite particles are tied together, and a surface-to-surface hard contact with frictionless tangential property is employed to describe the contact properties between neighboring composite particles and the guide. A C3D10M mesh type is applied to the sphere and composite particles, where a gradient size of 0.3-1.5 mm and a uniform size of 1 mm are used respectively based on a mesh convergence study.

At least two layers of mesh are seeded for each part of composite particles to accurately simulate the dynamic responses. For the rigid wall and guide, an R3D4 mesh type with a uniform size of 1 mm is assigned.

2.1.4 Validation

To validate the FE model, two configurations of the composite granular chain composed of 14 core-shell particles were fabricated and tested, as displayed in Table 1. According to Ref. [21], a minor frictional coefficient (f = 0.02) is applied to the surface-to-surface interaction to mimic the unavoidable frictions between particles and the guide. Furthermore, the PVC cover with the density $\rho_p = 1300\ \text{kg/m}^3$, Young's modulus E_p = 3.4 GPa, and Poisson's ratio v_p = 0.4 is considered to accurately simulate the particle structures. For validation, the impact velocity in FE models is consistent with that in experimental setups (i.e., 0.63 m/s). In both configurations (Figs. 6(b)-(c)), the contact force waveforms between experimental and numerical results agree well with each other although a slight discrepancy can be found in the rear of waveforms. This might originate from the possible rotations (or lateral movements) of cylindrical particles during stress wave propagation in experiments. Herein, the W-S configuration delivers a relatively low wave speed ($V_{\text{W-S}} \approx 0.26 V_{\text{S-W}}$) in contrast to the S-W configuration. The demonstration of solitary waves formation in 1D composite granular chains can be seen in APPENDIX A, and more comprehensive analysis of wave properties will be discussed in Section 2.3.1.

Table 1 Core-shell granular chains fabricated for model validation

Configuration		Material	$a = l$ (mm)	α	Total number
S-W	Shell	Stainless-steel	19.05	0.55	14
	Core	Nylon	19.05		
W-S	Shell	Nylon	19.05	0.57	14
	Core	Stainless-steel	19.05		

2.2 Results

Toward understanding typical wave properties within 1D composite granular chains, two representative cases with core-shell type particles ($\alpha = 0.1$) are selected and analyzed (Fig. 7). Based on the force maps in Figs. 7(a) and (d), the force amplitude (F_m) and wave width (L_s) are evaluated in a selected region (i.e., the white dotted lines), presented in Figs. 7(b) and (e) for S-W and W-S configurations, respectively. The finite spatial size and a consistent amplitude as the wave propagates are observed within both configurations, demonstrating the formation of strongly nonlinear solitary waves (i.e., Nesterenko solitary wave) in 1D composite granular chains.

Furthermore, F_m in S-W configuration (~43 N) is notably higher than that in W-S configuration (~23 N), however, similar L_s (~9 particle diameters) is achieved in the two configurations. Such performances should be attributed to the particle structures in 1D composite granular chains. According to the Mises stress distribution in Figs. 7(c) and (f), a localized compression is mostly observed at the neighboring shells, which demonstrates the dominant role of the shell in wave properties. Hence, a W-S composite chain brings out lower amplitude F_m and wave speed V yet longer duration T of each waveform compared

to an S-W one, which in turn, results in different values of F_m and weakens the discrepancies of L_s (i.e., VT) between the two configurations.

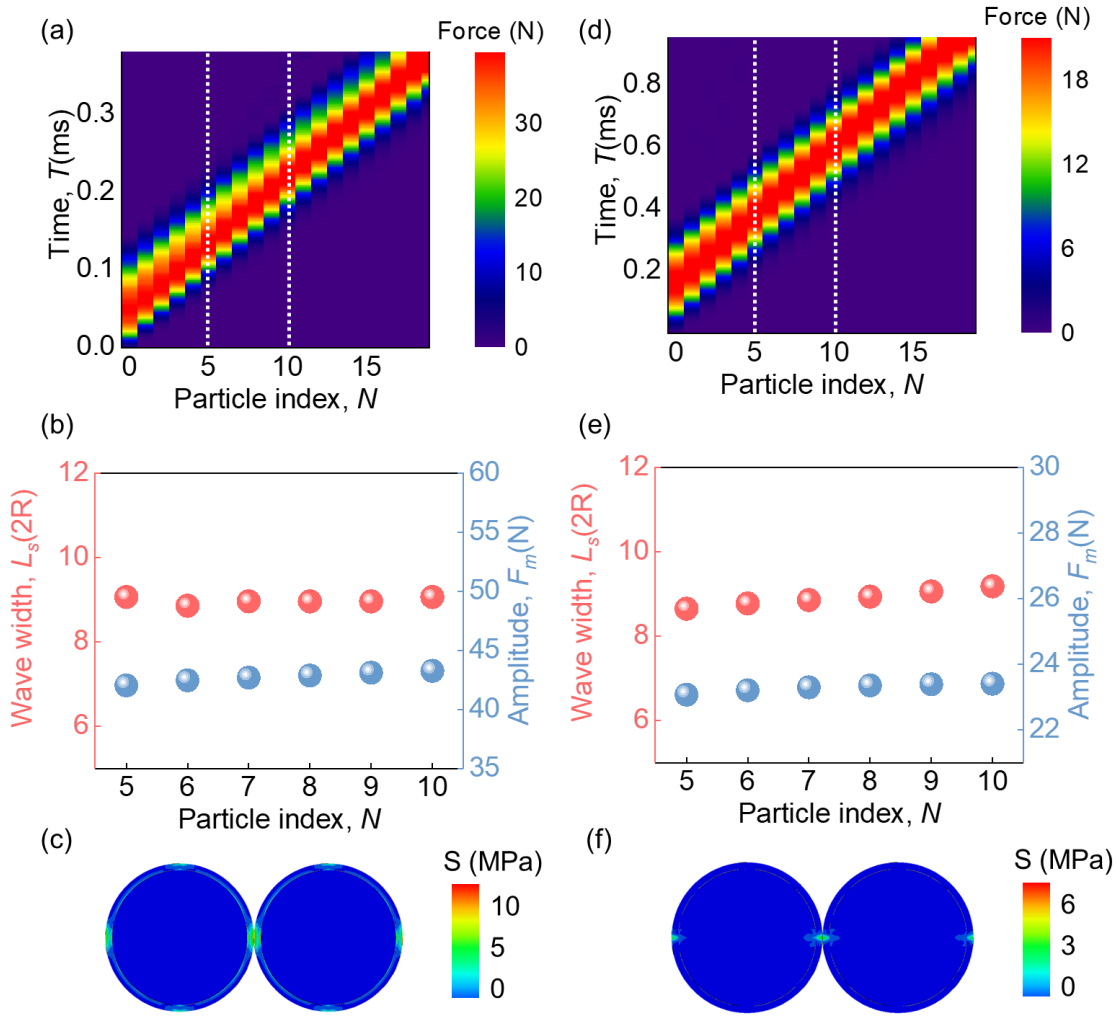

Figure 7 Typical results of wave propagation in 1D granular chains with core-shell particles ($\alpha = 0.1$). Contact force map: (a) S-W and (d) W-S; Wave properties: (b) S-W and (e) W-S; Stress distribution (the 2nd and 3rd particles): (c) S-W and (f) W-S.

2.3 Discussion

2.3.1 Core-shell type

It is natural to investigate solitary wave properties in more generalized composite

chains; thus, based on the validated model, a parametric study is conducted regarding a series of α. As depicted in Fig. 8(a) (solid symbols), the variation of wave speed is different in S-W and W-S configurations.

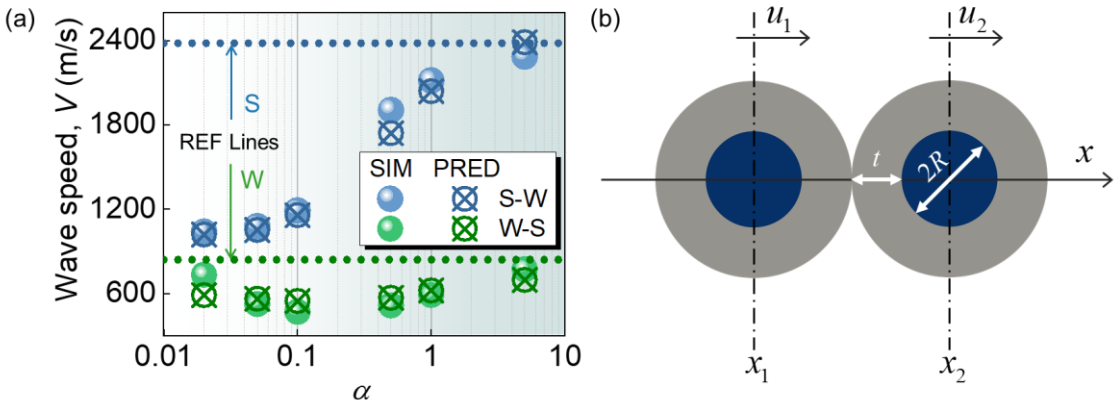

Figure 8 Numerical results (solid symbols) and theoretical prediction (cross symbols) of solitary wave speed variation as a function of α: (a) S-W (blue) and W-S (green) composite granular chains. (b) Illustration of interaction between two neighboring composite particles.

A continuously growing trend of wave speed is observed in the S-W configuration when α increases from 0.02 to 5 and the varying range falls between the "S" and "W" reference lines (i.e., the wave speeds of homogenous stainless-steel and nylon chains with solid cylinders). Nevertheless, in the W-S configuration, the wave speed experiences a decrease at first ($0.02 \le \alpha \le 0.1$) then gradually ascends as α ($0.1 \le \alpha \le 5$). Meanwhile, a rather low range of wave speed is achieved below the "W" reference line. The contributions of core and shell during stress wave propagation are first analyzed to explore the underlying mechanisms. Per Ref. [60], for core-shell type, only elastic properties of the shell need to

be considered if the core can be regarded as a rigid body, and the compressive deformation is much smaller than the shell thickness. In other cases, the contribution of both core and shell parts may be considered. Next, wave propagation in 1D composite granular chains is theoretically explored to elucidate the dependence of wave properties.

Instead of point contact between interacting spheres, a line contact pertains when cylindrical particles are aligned in parallel. An ideal line contact law was determined by Lundberg and Sjövall [104] as

$$d = \frac{2F\left(1-\nu^2\right)}{\pi El}\ln\left[\frac{\pi El^2}{F\left(1-\nu^2\right)\left(1\mp\gamma_s\right)}\right], \tag{15}$$

where F is the normal contact force between two cylindrical bodies, d is the deformation, E is Young's modulus, ν is Poisson's ratio, l is the length of cylindrical bodies, and γ_s is the shear strain. The contact law is quite difficult to be written in a simple and explicit expression. On the basis of laboratory tests of roller bearings, Palmgren explicitly developed an approximation of the line contact law with a sufficient degree of accuracy [44]

$$F = \frac{El^{8/9}d^{10/9}}{2.81\left(1-\nu^2\right)}. \tag{16}$$

Accordingly, quasi-static compressive tests on composite particles were conducted to demonstrate Eq. (16) (APPENDIX B). Considering the proposed 1D composite granular chains, the interaction between cylindrical particles can be described by

$$F = \frac{E_e l^{8/9}}{2.81\left(1-\nu^2\right)}\left[a-\left(x_2-x_1\right)\right]^{10/9}, \tag{17}$$

where x_1 and x_2 are the coordinates of the two cylindrical particle centers (Fig. 8(b)). Given different contributions of the core and shell, an effective modulus E_e is defined

$$E_e = f_c(\alpha)E_c + f_s(\alpha)E_s = \left[f_c(\alpha)s_1 + f_s(\alpha)\right]E_s. \tag{18}$$

Here, E_c and E_s are Young's moduli of the core and shell material, respectively. $f_c(\alpha)$ and $f_s(\alpha)$ are the governing coefficients depending on the geometric parameter α. $s_1 = E_c / E_s$ is the modulus mismatch ratio between core and shell materials. It is noted that the effective modulus is assumed to be constant for a specific configuration of the composite granular chain. However, the effective modulus of composite particles with a very thin shell might be amplitude dependent. Namely, a high amplitude will lead to a notable variation of the effective modulus, which is not considered in view of a relatively low impulse amplitude in the present study.

Thus, the equation of motion for the i^{th} particle in 1D composite granular chains is given by

$$\ddot{u}_i = A\left[\left(\delta_0 - u_i + u_{i-1}\right)^{10/9} - \left(\delta_0 - u_{i+1} + u_i\right)^{10/9}\right], \quad A = \frac{E_e l^{8/9}}{2.81\left(1-\nu^2\right)m_t}, \tag{19}$$

where δ_0 is the static displacement (for "sonic vacuum" systems, $\delta_0 \to 0$). m_t is the total mass of the composite particle and can be calculated by

$$m_t = \pi R^2 l\rho_c + \pi\left[(R+t)^2 - R^2\right] l\rho_s = \frac{\pi}{4} a^2 l\rho_s \left[\frac{s_2 - 1}{(1+\alpha)^2} + 1\right], \tag{20}$$

where ρ_c and ρ_s are densities of the core and shell, respectively, $s_2 = \rho_c / \rho_s$ is the density mismatch ratio. Based on the long-wave approximation [1], a strongly nonlinear wave equation for 1D composite granular chains can be expressed as

$$u_{tt} = -c^2 \left\{ (-u_x)^{10/9} + \frac{5a^2}{57}\left[(-u_x)^{1/18} \left((-u_x)^{19/18} \right)_{xx} \right] \right\}_x, \quad c^2 = Aa^{19/9}, \quad -u_x > 0. \tag{21}$$

Considering a solitary wave in "sonic vacuums", the wave speed is derived as

$$V = c\sqrt{\frac{18}{19}} \xi_m^{1/18}. \tag{22}$$

Here, ξ_m is the maximum strain in solitary waves. Concerning the leading approximation, ξ_m is also related to the force amplitude F_m [60]

$$F_m = \frac{E_e l^{8/9} \left(a\xi_m\right)^{10/9}}{2.81\left(1-\nu^2\right)}. \tag{23}$$

Combining Eqs. (22) and (23), the expression of wave speed V in 1D composite granular chains can be obtained

$$V = \sqrt{\frac{18}{19}} \frac{F_m^{1/20} l^{2/5} a}{\left[2.81\left(1-\nu^2\right)\right]^{9/20}} \frac{E_e^{9/20}}{m_t^{1/2}} = 0.61 \frac{F_m^{1/20} l^{2/5} a}{\left(1-\nu^2\right)^{9/20}} \frac{E_e^{9/20}}{m_t^{1/2}}. \tag{24}$$

The wave speed V has a nonlinear dependence on the amplitude F_m, yet the effect can be neglected due to the small exponent (1/20). Therefore, one may anticipate a constant wave speed during stress wave propagation even if there might be a slight decay of wave amplitude in actual tests. And the wave speed V in a specific composite chain can be

described by a nonlinear relation on the effective modulus E_e and the total mass m_t. Substituting Eqs. (18) and (20) into (24), one may obtain

$$V = S\left[f_c(\alpha)s_1 + f_s(\alpha)\right]^{9/20}\left[(s_2 - 1)(1+\alpha)^{-2} + 1\right]^{-1/2}, \tag{25}$$

where S is the constant and the varying trend of V can be predicted once the two coefficients of E_e are given with respect to α. Herein, the coefficients are intuitively defined by assuming that the total contribution of core and shell is unity (i.e., $f_s(\alpha) + f_c(\alpha) = 1$). Namely, the exact allocation proportion can be determined by defining either $f_c(\alpha)$ or $f_s(\alpha)$ for specific configurations. There are two critical factors to be considered while selecting appropriate functions: First, both core and shell may contribute to the wave dynamics; Second, the composite granular chain will behave like uniform granular chains when α is extremely close to zero or infinity. Therefore, the following functions are selected for S-W configuration,

$$f_c(\alpha) = \frac{1}{1+\alpha^{3/2}},\ f_s(\alpha) = 1 - f_c(\alpha), \tag{26}$$

and W-S configuration,

$$f_c(\alpha) = \frac{1}{1+3\alpha^{1/2}},\ f_s(\alpha) = 1 - f_c(\alpha). \tag{27}$$

The numerical results corroborate the theoretical predictions of the wave speed in both S-W and W-S configurations (Fig. 8(a)), revealing that the solitary wave speed can be efficiently tailored by manipulating the governing factors (i.e., E_e and m_t).

The underlying mechanisms are further explored by evaluating the displacement

difference between the two contact points [50]. Herein, the core and shell deformations of the first particle are compared for composite chains with different α values (Figs. 9-10).

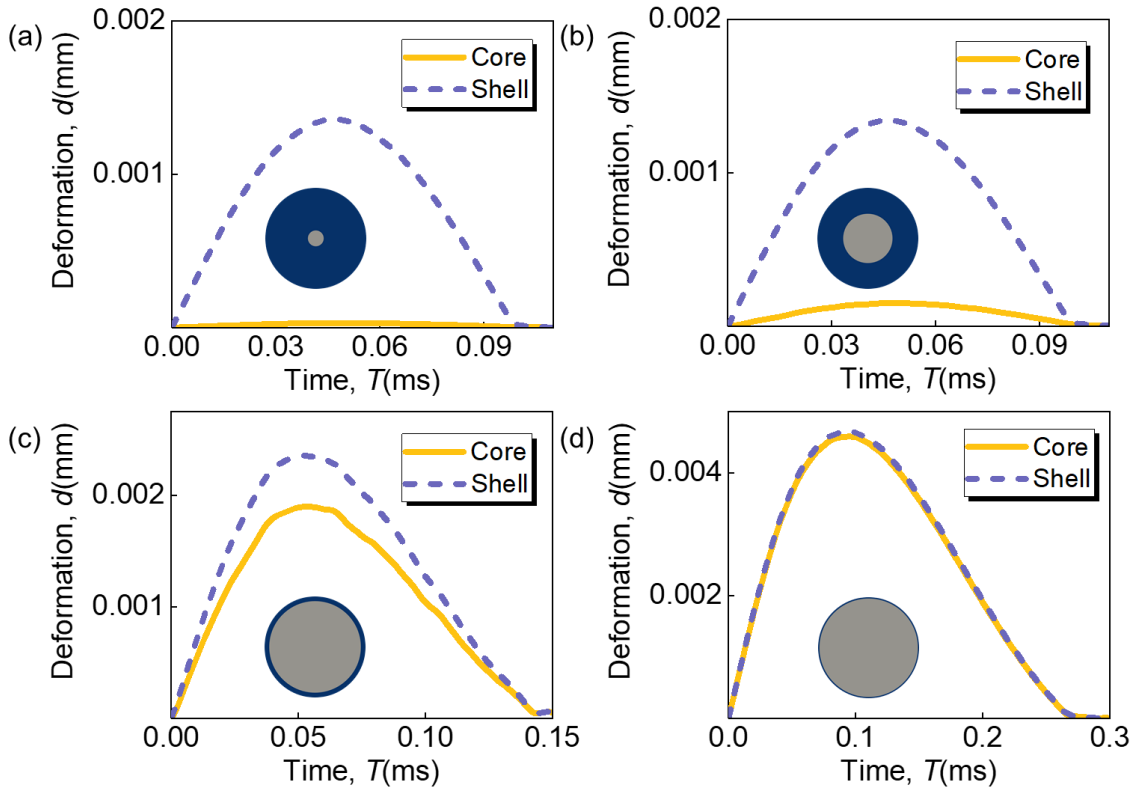

Figure 9 S-W: the deformation waveforms upon (a) $\alpha = 5$, (b) $\alpha = 1$, (c) $\alpha = 0.1$, (d) $\alpha = 0.02$. The blue and gray parts represent strong and weak materials, respectively.

Due to direct contact between neighboring particles, the shell undoubtedly plays a dominant position in both configurations during stress wave propagation. In the S-W configuration, the core deformation is almost zero at $\alpha = 5$ (Fig. 9(a)), indicating that the core can be assumed to be a rigid body. Furthermore, the maximum shell deformation (1.36×10^{-3} mm) is negligible in contrast to the shell thickness (7.94 mm). In that case, one may simply consider the elastic properties of the strong shell, which also explains why the

corresponding wave speed (2286 m/s) is close to the "S" reference line (2381 m/s). When α is decreasing from 5 to 0.02, a waveform of core deformation appears (Fig. 9(b)) and gradually becomes higher (Fig. 9(c)), finally overlaps with the shell deformation when $\alpha = 0.02$ (Fig. 9(d)). Thus, it is necessary to take both the core and shell into account in these cases, leading to a wave speed situated between the two reference lines.

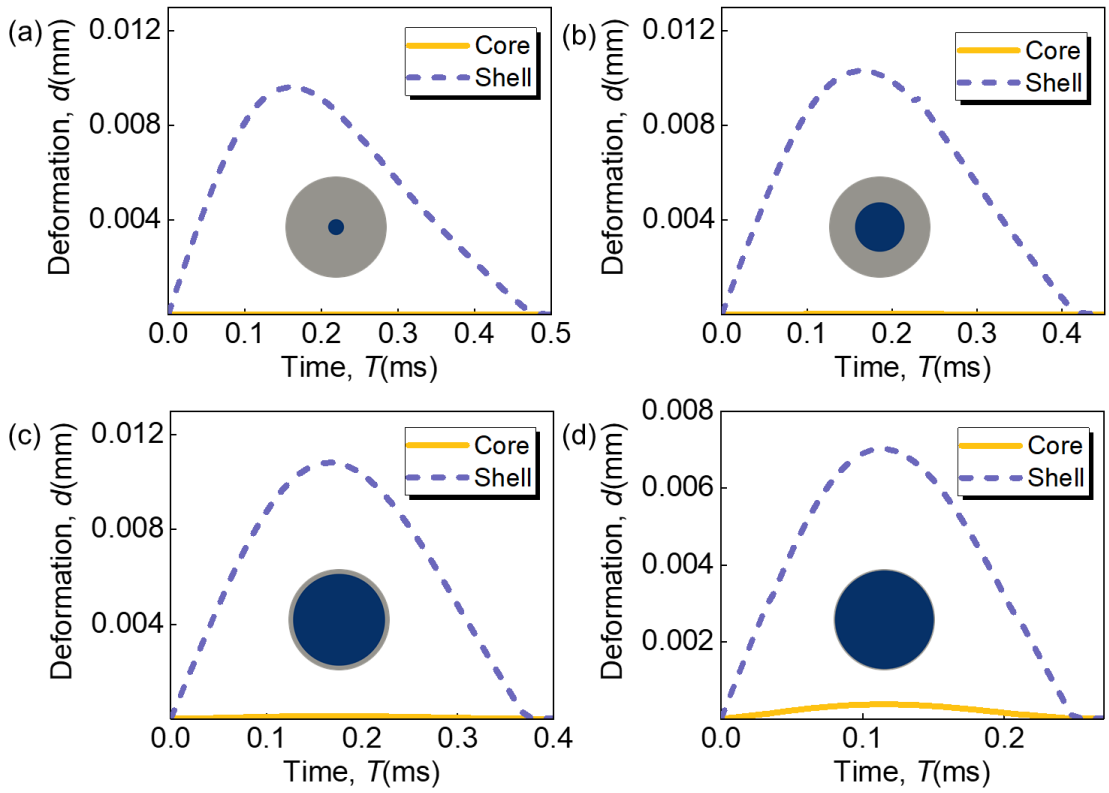

Figure 10 W-S: the deformation waveforms upon (a) $\alpha = 5$, (b) $\alpha = 1$, (c) $\alpha = 0.1$, (d) $\alpha = 0.02$.

In the W-S configuration (Fig. 10), the dependence of the core deformation on α tends to be different. The core deformation always maintains a value close to zero as α decreases from 5 to 0.1 yet shows a small non-zero waveform at $\alpha = 0.02$. The results

manifest that the core only contributes to wave dynamics when α is relatively low ($\alpha \leq 0.1$). Within this region, the core radius will decrease as α increases, which will gradually weaken the impact of the strong core and in turn account for the initial decrease of wave speed in the W-S configuration. Under higher values ($\alpha > 0.1$), the weak shell thickness increases as α, and the strong core can be assumed to be rigid. According to Eqs. (20) and (27), the total mass is decreasing under the increase of α while the effective modulus tends to have minor changes. Based on the nonlinear dependence of wave speed on governing factors (Eq. (24)), a slightly growing trend of wave speed is obtained within this region.

2.3.2 Further Extension to the Sandwich type

Since the effective modulus E_e and the total mass m_t of the composite particles are two critical factors in wave speed, it may be extended to more generalized 1D composite granular chains. In this section, two configurations (i.e., S-W-S and W-S-W) in sandwich-type are analyzed accordingly (Fig. 11), where the presence of an interlayer between core and shell might add more freedom to manipulate solitary wave properties in 1D composite granular chains.

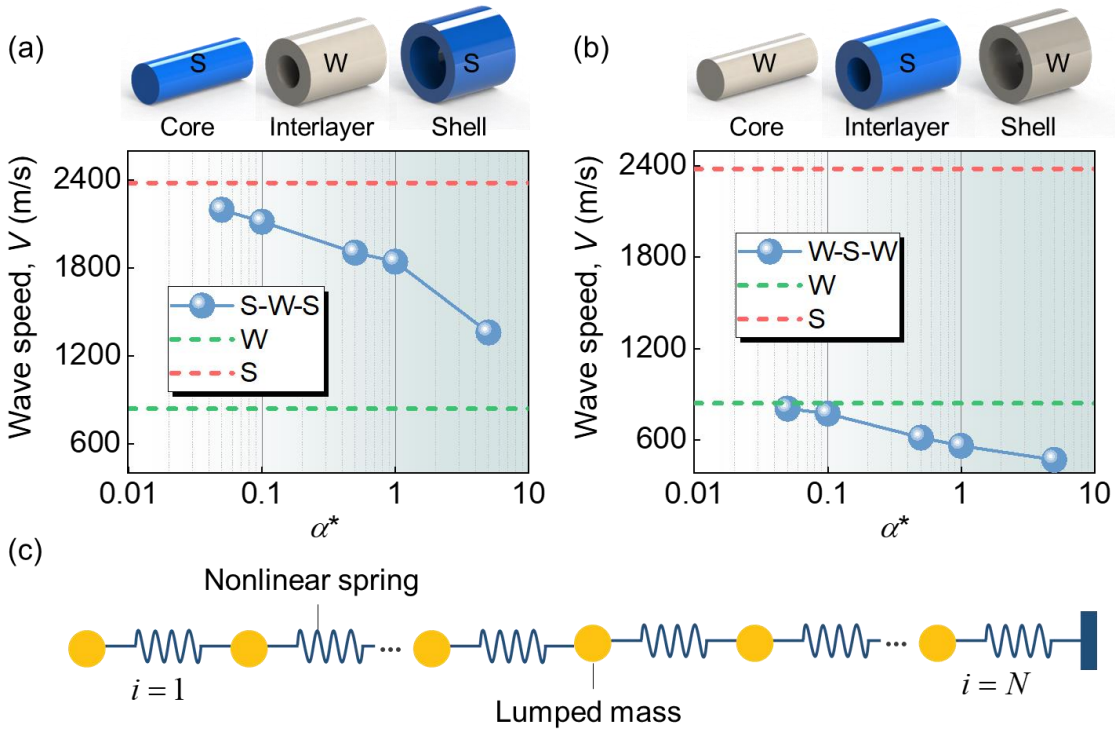

Figure 11 Wave properties in 1D composite granular chains with sandwich particles. The varying trend of wave speed with respect to α^*: (a) S-W-S and (b) W-S-W configurations. (c) A lumped mass-nonlinear spring model describing more generalized 1D granular systems.

Within the investigated range ($0.05 \le \alpha^* \le 5$) of the two configurations, the wave speed shows a shell-dominated behavior, which is consistent with the conclusions in Section 2.3.1. In deformation waveforms of S-W-S configuration (Fig. 12), a decreasing trend of deformation is observed from the outer to inner parts in all the cases and the core can be regarded as a rigid body due to the negligible core deformation. Thus, the shell and interlayer jointly lead to the decrease of wave speed as α^* increases (Fig. 11(a)).

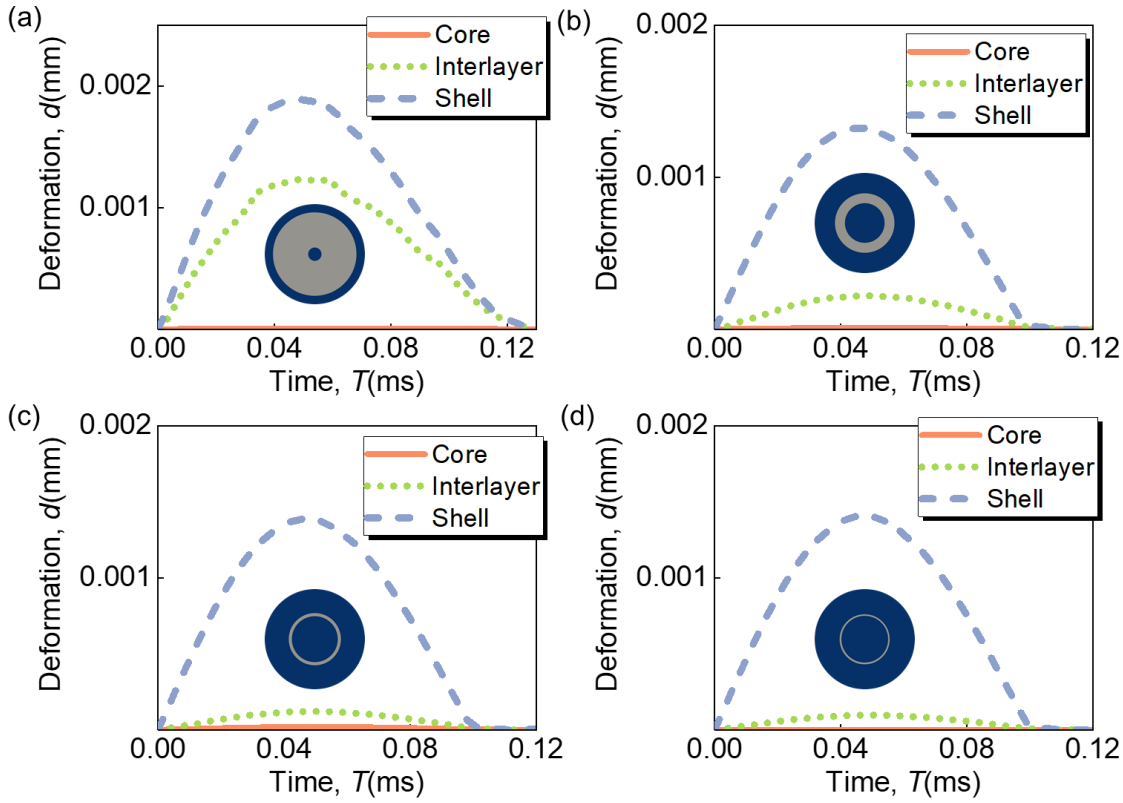

Figure 12 S-W-S: the deformation waveforms upon (a) $\alpha^*=5$, (b) $\alpha^*=0.5$, (c) $\alpha^*=0.1$, (d) $\alpha^*=0.05$.

In the W-S-W configuration (Fig. 13), the interlayer and core deformations overlap with each other and are much smaller compared to the shell deformation that plays a significant effect on wave properties. This degrades into the W-S configuration ($0.1\leq\alpha$), namely, an increase in α^* brings about smaller shell thickness, in turn, a lower wave speed (Fig. 11(b)).

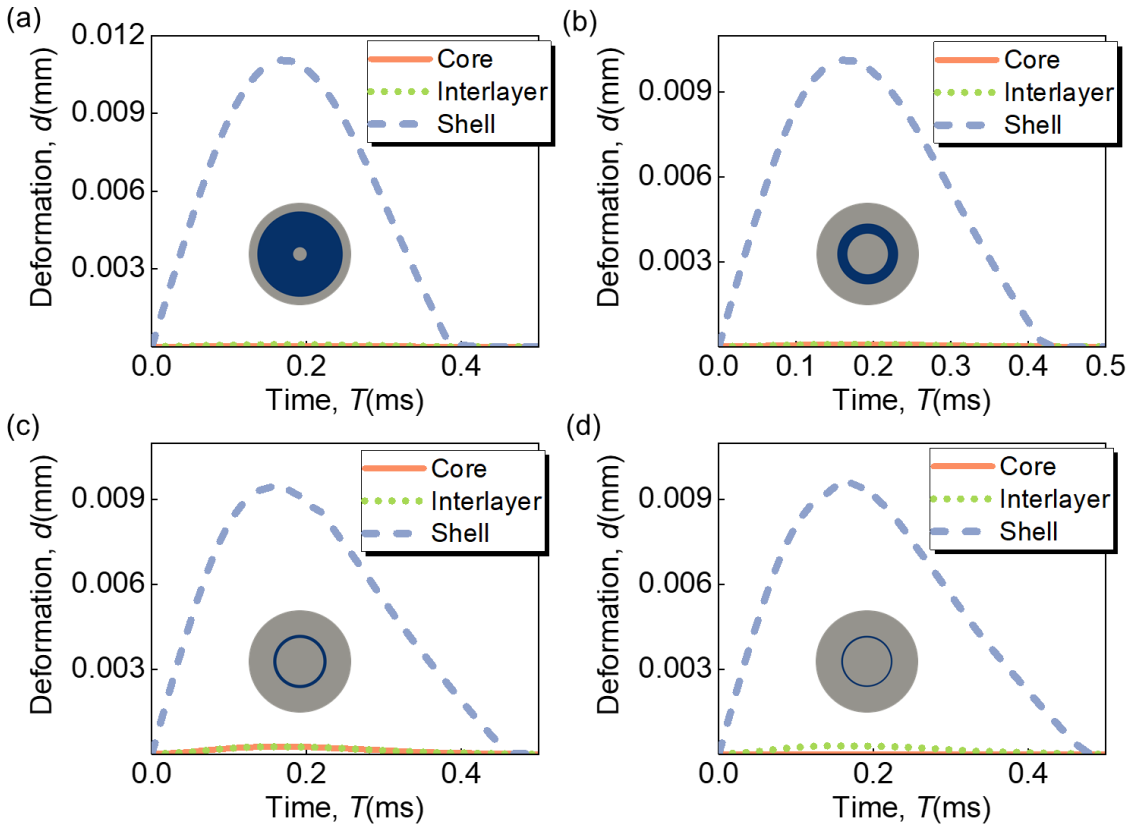

Figure 13 W-S-W: the deformation waveforms upon (a) $\alpha^*=5$, (b) $\alpha^*=0.5$, (c) $\alpha^*=0.1$, (d) $\alpha^*=0.05$.

Considering a more generalized composite granular chain, it can be described by a series of lumped masses connected by nonlinear springs (Fig. 11(c)), where the mass and the nonlinear stiffness are determined by m_t and E_e, respectively. Hence, it is possible to quantitatively manipulate solitary wave properties in composite chains by adjusting the governing factors. Basically, this can be achieved by simply tuning the geometric parameter, while the tailoring range can be greatly extended by selecting an appropriate material system for "strong" and "weak" materials or designing composite particles with a higher hierarchy.

2.4 Conclusions

In this chapter, wave propagation in 1D cylindrical composite granular chains was comprehensively investigated. Two types of composite particles were designed by using "strong" and "weak" materials in different parts, respectively, including core-shell and sandwich structures. Both numerical results and experimental evidence demonstrated the formation of strongly nonlinear solitary waves in chains of core-shell cylindrical particles. A parametric study was conducted by varying the geometric parameter, where the shell-dominated dynamic response was observed 1D composite granular chains. Also, a theoretical analysis of wave propagation was carried out based on the long-wave approximation, which coincided with the numerical results and uncovered the nonlinear dependence of wave properties on the governing factors (i.e., the effective modulus and total mass). Finally, the influencing mechanisms were extended to more generalized composite granular chains. This study has shaped the fundamental understanding of wave propagation in 1D composite granular chains and opened an efficient approach to designing granular systems with exact wave properties.

CHAPTER 3 UNIVERSAL DESIGN OF EQUIVALENT SYSTEM SUPPORTING SOLITARY STRESS WAVES

The initial motivation of the study in this chapter is prompted by how to construct specific granular systems with desired wave properties and particle motions. Here, the methodology to construct equivalent systems (i.e., granular systems with identical output) is systematically studied using theoretical analysis, experiments, and numerical simulation. The properties of Nesterenko solitary wave supported by 1D spherical granular chains are investigated, where an equivalent wave transmission is achieved among various materials and dimensions. The results of typical experiments and finite element analysis fully support the established theoretical predictions based on Hertz contact and long-wavelength approximation theory, which yields a broad class of equivalent systems. Finally, an instructive mechanism map, containing various equivalent systems, is proposed to clarify the relationship between geometric parameters and material properties, providing insights into designing a desired nonlinear dynamic system and guidance for potential engineering applications.

3.1 Methods

Focusing on engineering applications, one may face an important problem on how to construct a granular system to realize desired wave properties and particle motions. Herein equivalent systems refer to those systems with various granular properties (either/both in material properties or/and particle sizes) with the same system output (e.g., particle velocity,

wave speed, and wave width). Therefore, methodologies to obtain equivalent systems are proposed and discussed.

3.1.1 Theoretical analysis

Hertz's seminal work [105] established the relation between force and deformation of two spherical particles. With the assumption of only elastic contact between particles, the equation of motion for a 1D uniform spherical granular chain with dissipation, namely the governing equation of equivalent systems can be written as [1, 15, 39]

$$\ddot{u}_i = \lambda\left[u_{i-1}-u_i\right]_+^{3/2} - \lambda\left[u_i-u_{i+1}\right]_+^{3/2} - \gamma\dot{u}_i,\ \lambda = \frac{R^{-5/2}}{2\sqrt{2}\pi\left(1-\nu^2\right)}\frac{E^*}{\rho}, \tag{28}$$

where u_i is the displacement of the i^{th} particle and closely related to the coordinate x_i, λ is a coefficient related to material properties (i.e. modulus E^*, density ρ, and Poisson's ratio ν) and geometric parameters (i.e. radius R) of particles. $c=\sqrt{E^*/\rho}$ is 1D elastic wave speed of particles material. The dissipative effect caused by friction is taken into consideration by the last term in Eq. (28) [100]. γ is a damping coefficient, depending on particle properties in 1D granular systems. Meanwhile, the viscosity of material can be described by a dissipative term depending on the relative velocities of contacting particles [11]. However, an analytical relation between the dissipative coefficient and characteristics of a specific granular chain is required to include viscous effect in developing equivalent systems. Coefficient of restitution (COR) has been

demonstrated as an indicator of the relative energy loss and is closely related to viscosity without plastic deformation. According to previous studies, the CORs of materials mainly considered in this chapter (e.g., aluminum, stainless steel) are quite close to unity upon low initial velocities. In addition, Nesterenko solitary waves were achieved in viscoelastic particle materials as well, such as Teflon [14] and Nylon [66] granular chains. Therefore, the dissipation caused by viscosity was neglected for simplicity.

To apply the quasi-static Hertz law for dynamic problems, the characteristic times of contact deformation t_c are required to be significantly longer than the characteristic period of grain oscillations T_c [1], which is

$$t_c \gg T_c \approx 2.5\frac{R}{c}. \tag{29}$$

The following variables are introduced to make it nondimensional.

$$\bar{u} = \frac{u}{2R},\ \bar{t} = \frac{t}{2R/c},\ \bar{x} = \frac{x}{2R}. \tag{30}$$

Substituting these dimensionless variables into the equation of motion gives

$$\frac{\partial^2 \bar{u}}{\partial \bar{t}^2} = \tilde{\lambda}\left[\left(\bar{u}_{i-1} - \bar{u}_i\right)^{3/2} - \left(\bar{u}_i - \bar{u}_{i+1}\right)^{3/2}\right] - \tilde{\gamma}\frac{\partial \bar{u}}{\partial \bar{t}},\ \tilde{\lambda} = \frac{2}{\pi\left(1-\nu^2\right)},\ \tilde{\gamma} = \frac{2R\gamma}{c}. \tag{31}$$

In the long-wave approximation, the wave equation for the chain of spherical particles can be written in the nondimensional form [106]

$$\frac{\partial^2 \bar{u}}{\partial \bar{t}^2} + \tilde{\gamma}\frac{\partial \bar{u}}{\partial \bar{t}} = \tilde{\lambda}\left[\frac{3}{2}\left(-\bar{u}_{\bar{x}}\right)^{1/2}\bar{u}_{\bar{x}\bar{x}} + \frac{1}{8}\left(-\bar{u}_{\bar{x}}\right)^{1/2}\bar{u}_{\bar{x}\bar{x}\bar{x}\bar{x}} - \frac{1}{8}\frac{\bar{u}_{\bar{x}\bar{x}}\bar{u}_{\bar{x}\bar{x}\bar{x}}}{\left(-\bar{u}_{\bar{x}}\right)^{1/2}} - \frac{1}{64}\frac{\left(\bar{u}_{\bar{x}\bar{x}}\right)^3}{\left(-\bar{u}_{\bar{x}}\right)^{3/2}}\right]. \tag{32}$$

Considering the problem where the initial strain (ξ_0) equals zero (sonic vacuum case),

Nesterenko discovered the analytical solution of Eq. (32) for frictionless granular systems with a general power-law interaction ($\xi = -u_x = -\overline{u}_{\bar{x}}$) [1, 106]:

$$\xi = A_0 \left| \sin\left(\frac{n-1}{n+1}\sqrt{\frac{6(n+1)}{n}}\,\frac{(x-V_0 t)}{2R} \right) \right|^{\frac{2}{n-1}} = A_0 \sin^p \omega(x-V_0 t), \tag{33}$$

where A_0 , p and ω are constants. Since n is 3/2 for spherical particles (following Hertzian contact law), p would be 4 in this study. For small values of $\tilde{\gamma}$, Rosas and Lindenberg [100] proposed a modified solution by considering the decay in both energy and pulse velocity, which gives

$$\xi = A(t)\sin^p \omega\left(x - \int_0^t V(t)\,dt\right), \tag{34}$$

For spherical particles subjected to weak dissipation, the amplitude and phase speed of waves can be denoted by [100]

$$A(t) = A_0 e^{-\frac{4}{9}\tilde{\gamma}t},\ V(t) = V_0 e^{-\frac{1}{9}\tilde{\gamma}t}. \tag{35}$$

Obviously, both the amplitude and phase speed of the wave will decrease exponentially as a function of time. It should be noted that the shape and width of the wave are assumed to be constant during wave propagation. In the meantime, the granular chain discussed here is relatively short, including 10-20 spherical particles. This yields the total transmission time in the interval of 10-100 microseconds in experiments for steel particles with a diameter of about 5-10 millimeters and Nesterenko solitary wave amplitude about a few hundred Newtons [7, 8]. Furthermore, in some materials, the damping can be neglected

in the first approximation with prevailing nonlinear and dispersive effects described by Eq. (32) [1]. Therefore, the weak dissipative effect will be ignored in the analysis of equivalent systems. A striker identical to particles in the granular chain was adopted to generate a propagating pulse.

Herein, two types of equivalent systems are investigated respectively, i.e., generalized equivalent systems and restricted equivalent systems. The generalized equivalent systems refer to a group of granular systems with different granular properties but identical particle motions. More rigorously, the restricted equivalent systems, consisting of various granular systems sharing the same wave properties (especially wave speed) with identical particle motions, are further developed. Note that the physical systems themselves are not equivalent, but rather the idealized Hertzian systems, in which dissipation is neglected, are equivalent.

(1) Generalized equivalent systems

Provided those different granular systems have identical λ, it is possible to obtain equivalent motions of particles in 1D granular chains. Namely, identical dynamic particle motions can be achieved in equivalent systems with different combinations of material properties and geometric parameters, which yields an approach to decoupling material and particle size of granular crystals and developing generalized equivalent systems according to Eq. (28).

(2) Restricted equivalent system

In the above-mentioned generalized equivalent systems, two equivalent systems share the same particle velocity but may not have the same wave properties. To further explore the possibility to have equivalent systems, one may focus on a granular system where Nesterenko solitary wave propagates with phase speed V_s having the shape described by one hump of the periodic function. [1, 106]

$$\xi = \frac{25}{16}\frac{\bar{V}_s^4}{\tilde{\lambda}^2}\cos^4\left(\frac{\sqrt{10}}{5}\bar{x}\right), \tag{36}$$

where $\bar{V}_s = V_s / c$ is the nondimensional phase speed of solitary waves, which nonlinearly depends on the nondimensional maximum particle velocity $\bar{v}_m = v_m / c$, according to [1, 106]

$$\bar{V}_s = \left(\frac{16}{25}\right)^{1/5} \tilde{\lambda}^{2/5} \bar{v}_{\mathrm{m}}^{1/5} \quad . \tag{37}$$

Indeed, some previous works have significantly improved Eq. (36), such as, providing an analytical method via Padé approximation [107] and calculating in a numerically exact way [108]. In terms of the virial theorem for particles interacting according to the Hertz law, the relationship between kinetic energy E_k and potential energy E_p during the propagation of Nesterenko solitary wave is given by [1]

$$\frac{E_k}{E_p} = 5/4. \tag{38}$$

The excitation of the Nesterenko solitary wave is considered using a striker with mass equal to the particle mass in the chain. Thus,

$$\frac{E_k}{E_t} = 5/9. \tag{39}$$

Note that the total energy of the granular system E_t is determined by the amplitude of the impact velocity of the striker $\overline{v}_i$, which is

$$E_{\mathrm{t}} = \frac{1}{2} m \overline{v}_i^2. \tag{40}$$

According to the solution of Nesterenko solitary wave given in Eq. (36), the kinetic energy of the central particle of the hump is

$$E_k^{\mathrm{Central}} = \frac{1}{2} m \overline{v}_{\mathrm{m}}^2 = \frac{1}{1+2\cos^8\left(\pi/4\right)} E_k. \tag{41}$$

Therefore, the relation between the impact velocity and the maximum particle velocity can be obtained.

$$\frac{\overline{v}_{\mathrm{m}}}{\overline{v}_i} = \sqrt{\frac{5}{9\left[1+2\cos^8\left(\pi/4\right)\right]}} \approx 0.70. \tag{42}$$

Substituting Eq. (42) into Eq. (37), the phase speed (V_s) of Nesterenko solitary waves in the granular chain is only related to the elastic wave speed of material and impact velocity.

Furthermore, it is obvious that the Nesterenko solitary wave is highly localized and its wave width (the characteristic spatial size) in nondimensional form is described by Eq.

(36). It equals

$$L_S = \frac{5\pi}{\sqrt{10}} \approx 5, \tag{43}$$

which indicates that the wave width is only dependent on the geometry of the particles (about 10R) [1, 14, 106].

Therefore, selecting materials (i.e., E^* and ρ) with identical 1D elastic wave speed while keeping consistent in geometric parameters (i.e., R) and initial conditions (i.e., V_i), one may create more rigorous equivalent systems. Theoretically, such systems share identical particle motions and other wave properties (e.g., V_s and L_S).

3.1.2 Experimental setups

As shown in Fig. 14, 1D granular chains composed of $N = 20$ spherical particles were assembled in a horizontal guide where lateral motion was restricted to investigate the Nesterenko solitary waves in equivalent systems. Four 1D granular chain systems were considered in the experiment, i.e., stainless-steel, aluminum, brass, and nylon 1D granular chains. As such, brass and stainless-steel granular chains serve as generalized equivalent systems while stainless steel and aluminum 1D granular chains serve as restricted equivalent systems. The corresponding material and geometric properties are summarized in Table 2.

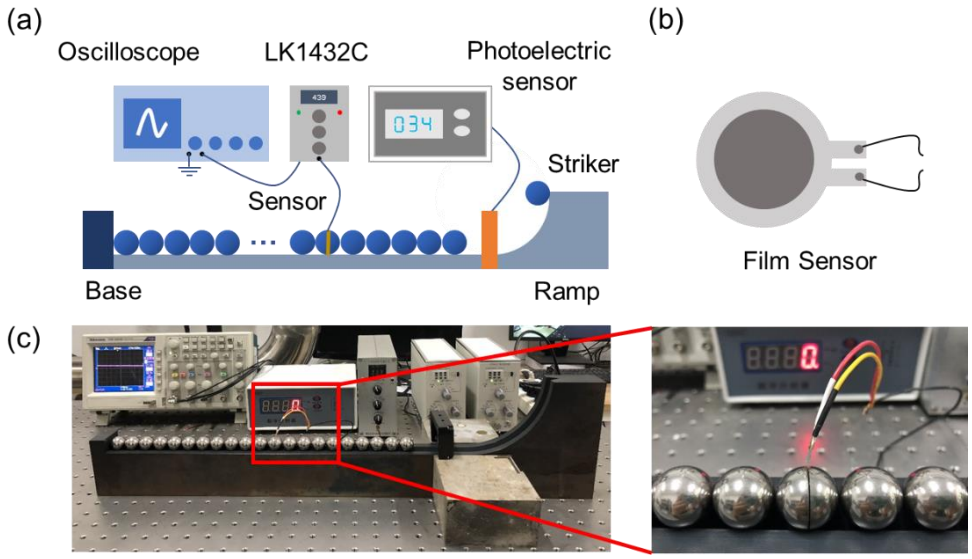

Figure 14 Experimental setups. (a) Overall configuration of a horizontal test platform for 1D spherical granular crystal; (b) Schematic of the film sensor structure; (c) Experimental setup for 1D granular chain consisting of *N* beads, where film sensor was embedded in the bead to obtain the compression force

The particle was initially cut along its diameter direction into two halves via Wire Electrical Discharge Machining (WEDM) and then, a film sensor (Fig. 14(b)) was glued between these two caps. The effect of the glued sensor was not considered due to its ignorable thickness and mass when compared to spherical particles. Connected to a four-channel Tektronix Oscilloscope (TDS-2024C) and two amplifiers, two film sensors were embedded into the particles (the 5^{th} and 10^{th} particles) of the system to obtain the compression force, phase speed, and clear visualization of the propagating wave.

Table 2. Material properties and geometric parameters of granular chains in experiments

Properties	Stainless-steel	Aluminum	Brass	Nylon[66]
Young's modulus (GPa)	200 [109]	68.9 [109]	103 [109]	3[110]
Density (kg/m^3)	7927.5	2699.8	8426.5	1140
Poisson's ratio	0.28 [109]	0.33 [109]	0.34 [109]	0.4
Diameter (mm)	20	20	15	15.875

The film sensor (diameter a = 15 mm, thickness t = 0.3 mm) used in the experimental setup can generate an electric charge in response to applied mechanical stress. The electric charge is proportional to the applied force, which is indicated by the sensitivity of the sensor K_s. In view of different application scenarios, K_s is 43.94 pC/N under high-speed dynamic test and 20 pC/N upon low speed/static test scenarios, respectively. Since the impact velocity was relatively low in this study (< 2 m/s). the sensitivity of the film sensor would be K_s = 20 pC/N. Similar to the calibration method in previous literature [14], the initial velocity and linear momentum conservation law can be used to calibrate the film sensors. The area under the force-time curve (from the initial point to the crest) measured by the film sensor was compared to the initial linear momentum of the particle. The amplifier (LK1432C) used here has a frequency response of up to 600 kHz. Combined with the film sensor and the oscilloscope, the amplifier can be used to detect and record high-speed dynamic/vibration signals. The maximum input charge is 10^5 pC and the noise is less than 10 mV. Herein, the output voltage per unit was set to 1 (O = 1 mV/unit) and the sensitivity was set to K_a = 2.0 pC/unit. Thus, the following equation was applied to obtain applied force (F) corresponding to the output voltage (U) recorded by oscilloscope:

$$F = \frac{U}{O\left(K_s / K_a\right)}, \tag{44}$$

The 1D granular chain was impacted by a striker identical to particles in the system to generate a propagating pulse. The impact velocity was measured by a photoelectric

sensor in the experiment and different impact velocities (0.3 m/s, 0.4 m/s, 0.5 m/s, and 1.654 m/s) were achieved by releasing the striker from various heights along the ramp. To ensure the repeatability of the experiments, 3 repeated tests were performed for each scenario.

3.1.3 Finite element model

The finite element code ABAQUS/EXPLICIT is employed to analyze the Nesterenko solitary waves propagation and localization in equivalent systems. As Fig. 15 shows, a three-dimensional FE model is developed for the 1D granular chain, where tetrahedral second-order elements (C3D10M) are used for the spheres.

A denser mesh (0.05 mm) is adopted within the vicinity of the contact point and a relatively coarser mesh (2.00 mm) is used in other areas to reduce computational costs while maintaining accuracy. A mesh size convergence test was carried out to obtain computational confidence [59] (APPENDIX C). A base plate is set to rigid and fixed at the end of the granular chain. The surface-to-surface interaction with the kinematic contact method is applied to model the contact between particles, where the tangential direction is frictionless, and the normal direction is hard contact to prevent the overlap between surfaces. Impact pulses are generated by a striker with different initial velocities. The particles in the 1D granular chain have free axial vibrations but are restricted in other directions. The material properties (i.e., Young’s modulus, density, and Poisson’s ratio)

used in numerical analysis are consistent with those in experimental setups.

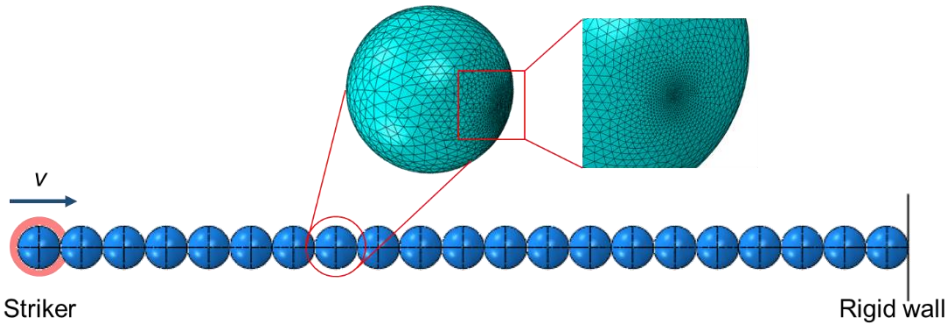

Figure 15 Finite element model of 1D spherical granular chain. Impact pulses were generated with a striker under different impact velocities.

3.1.4 Validation

Force-time responses captured by sensors embedded in specific particles (5th and 10th particle) are compared with the corresponding responses obtained from the simulations to validate the FE model (Fig. 16). Both metal (stainless steel) and polymer (nylon) granular chains were considered.

The results imply that a solitary wave is developed via the initial excited impulse in the granular chain. In Fig. 16(a) and (c), a tail with small amplitude can be observed in experimental results, which may result from dissipation on the shape of short pulses. The wave speed is calculated by considering the distance between two specified particles with the sensor and the corresponding interval. Accordingly, the wave speeds in experimental, theoretical, and numerical cases were shown in Table 3. Obviously, the experiment results are in good agreement with the theoretical and numerical ones. Therefore, the developed

FE model is reliable to explore the Nesterenko solitary wave properties in 1D spherical granular chains.

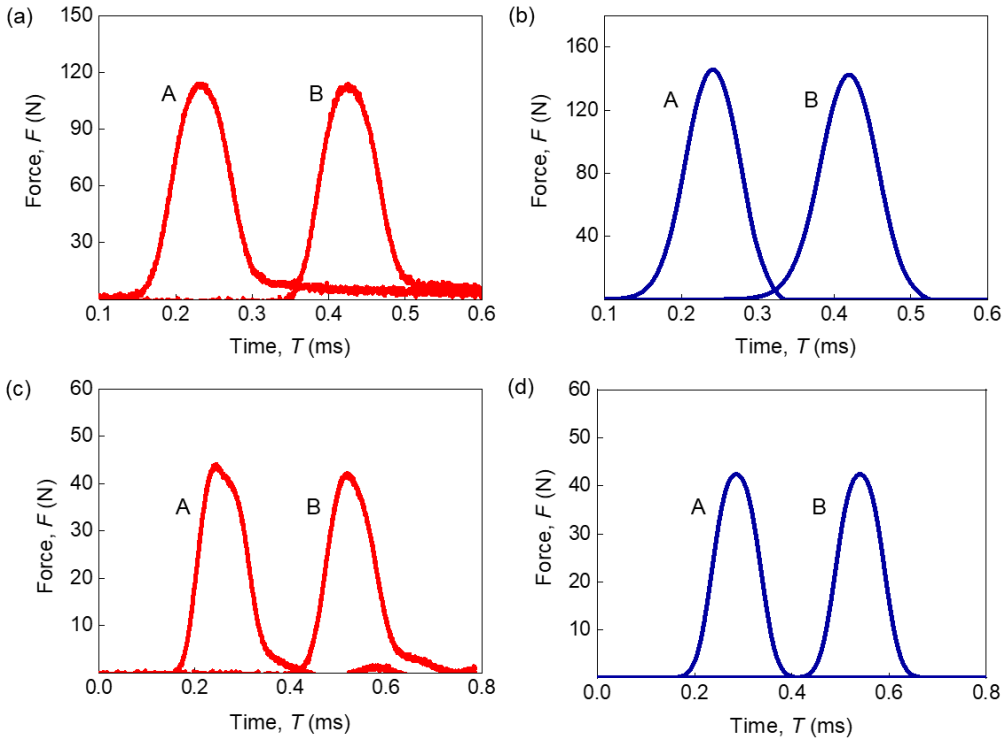

Figure 16 Comparison of force-time responses of (a) (c) experiments and (b) (d) finite element analysis of Nesterenko solitary wave. Herein, (a) and (b) are results of 1D stainless steel granular chain with an impact velocity of 0.3 m/s, while (c) and (d) are results of 1D nylon granular chain with an impact velocity of 1.654 m/s. The curves in group A and group B show the responses of 5th particle and 10th particle in the 1D granular chain, respectively

The experiments of three types of granular chains (i.e., stainless steel, aluminum, and brass) were carried out under different impact velocities (0.3 m/s, 0.4 m/s, and 0.5 m/s) to investigate the wave properties of different equivalent systems. The repeated testing results are presented in Fig. 17. All the testing results for analysis are the averages of experimental

measurements.

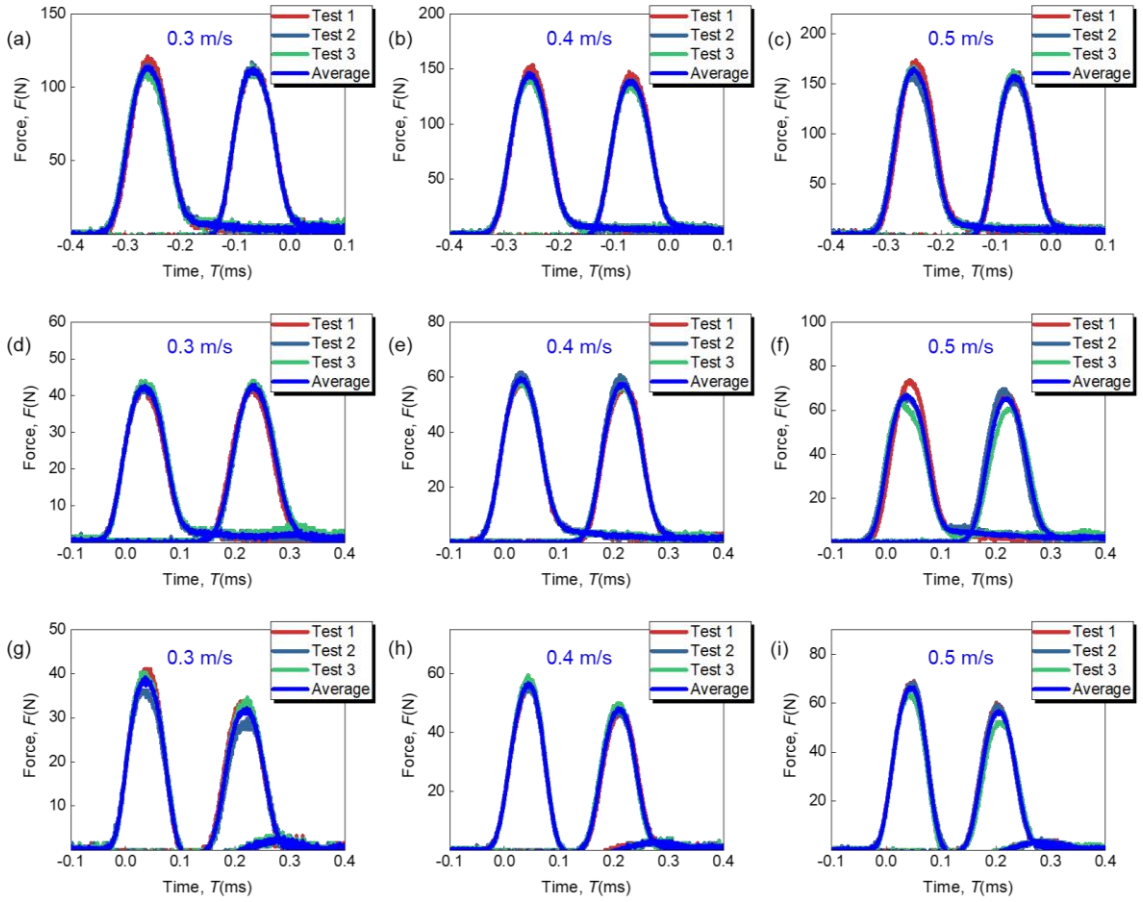

Figure 17 Repeated testing results of three types of granular systems under different impact velocities. (a)-(c) Stainless steel; (d)-(f) Brass; (g)-(i) Aluminum

Table 3 Comparison of wave speeds in 1D granular chains

Wave speed	Theoretical (m/s)	Numerical		Experimental	
		V_s (m/s)	Error (%)	V_s (m/s)	Error (%)
Stainless steel	527.4	555.2	5.27	521.25±5.16	1.17
Nylon	311.85	311.28	0.19	310.52±5.25	0.43

3.2 Results and discussions

3.2.1 Mechanism map

Based on the equation of motion and the expression of phase speed V_s obtained in

Section 3.1.1, mechanism maps are presented in Fig. 18, implying the relationship between material and particle size of the 1D granular crystal system. Like theoretical analysis, one may use a dimensionless strategy by comparing V_s and c to obtain a normalized wave speed $\bar{V}_s = V_s / c$. Meanwhile, the radius is normalized with respect to the transient displacement of the specific particle, i.e., $\bar{R} = R / v_m \tau$, where the response distance is determined by the maximum particle velocity (v_m) and unit time (τ).

Figure 18(a) predicts that there is a nonlinear dependence on the normalized phase speed and radius. Together with corresponding properties of Nesterenko solitary waves and granular systems, the distribution of equivalent systems is also shown per the variation of λ. It is evident that the transmitted wave properties through the granular chain are nonlinearly dependent on $\bar{V}_s$ and $\bar{R}$, which enables equivalent performance between different granular systems. In addition, this distinctive response is more sensitive to $\bar{V}_s$. From the energy transmission perspective, the generated compressive pulse propagates between the particles without significant energy dissipation, implying that the most of incident energy is dispensed to different particles in the form of both kinetic energy and potential energy, while they closely relate to materials and geometries. In the real-world scenario, a portion of incident energy is converted to the strain energy of the guide rail and inverse kinetic energy of the striker particles due to the rebounding of the striker together with unavoidable contact between nonlinear chain and linear guides. Nevertheless, it will

not change the dominant energy transmission mechanism between granular particles. These coupling behaviors provide a more extended tuning area for us to design a granular system with desired performance.

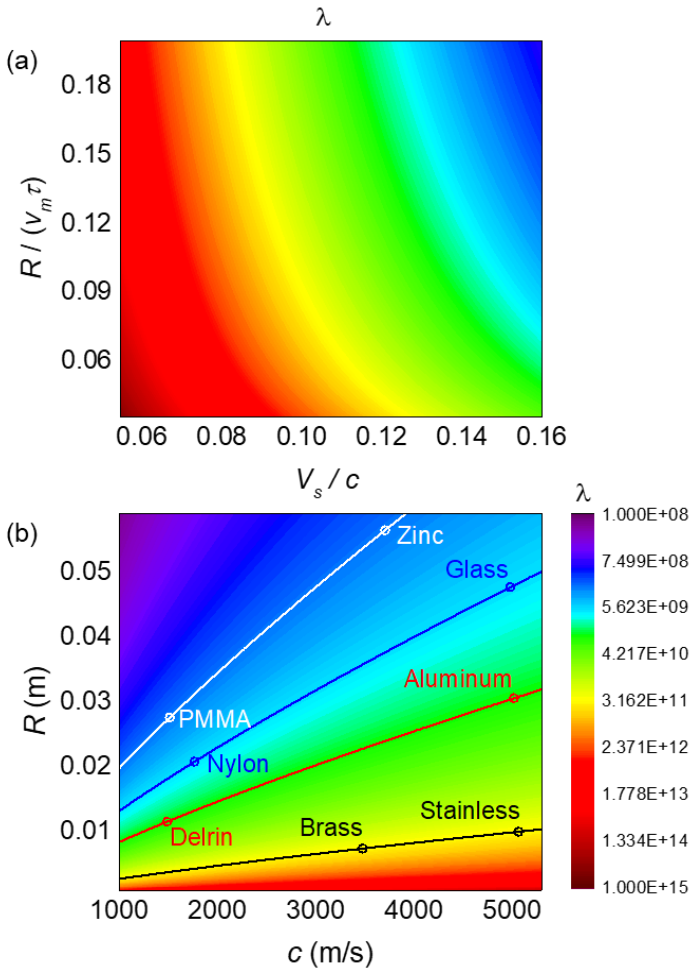

Figure 18 Mechanism maps of equivalent systems. (a) A comprehensive map indicating the normalized properties of Nesterenko solitary waves and granular chains, together with the distribution of equivalent systems and (b) An instructive map to design a granular system. The circle symbols are four selected groups of generalized equivalent systems from specific lines with identical λ.

Figure 18(b) provides more direct instruction on how to use particles with arbitrary

materials or geometries to develop equivalent systems. In this contour plot, all kinds of geometries and materials granular systems are gathered according to their transmitted wave properties. Different bands or lines with an identical magnitude of λ represent a series of equivalent systems. For instance, along the lines with identical λ, it is possible to find particle groups with different materials and geometries to construct generalized equivalent systems as the circle symbols denoted in Fig. 18(b), e.g., brass beads with a diameter of 14.8 mm and stainless beads with a diameter of 20 mm.

3.2.2 Generalized equivalent system

3.2.2.1 Experimental results

The experimental results of generalized equivalent systems are presented in Fig. 19. It is evident that both the 1D granular chains (i.e., Brass and stainless steel chains) considered in experiments support the formation and propagation of Nesterenko solitary wave. Several effective evaluation criteria are introduced to further analyze the experimental results, i.e., the maximum particle velocity v_m and interval between two specific peaks ΔT (See APPENDIX D). Table 4 is a summary of experimental results of brass and stainless granular chains in terms of ΔT and v_m, where 1D brass and stainless steel granular chains are verified to be generalized equivalent systems.

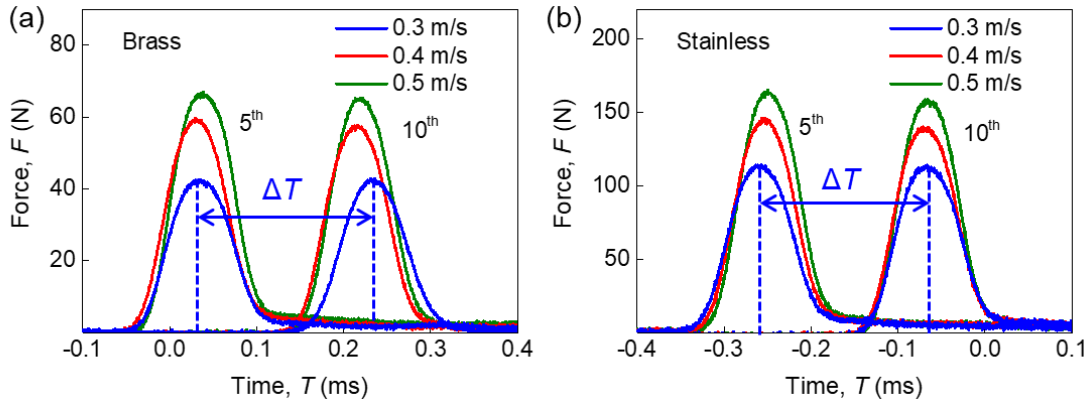

Figure 19 Experimental results of generalized equivalent systems. Force-time curves of 5th and 10th particles in (a) 1D brass granular chain and (b) 1D stainless steel granular chain at three different impact velocities (0.3 m/s, 0.4 m/s, 0.5 m/s)

Table 4 Testing results of generalized equivalent systems under various impact velocities.

Impact velocity (m/s)	Brass		Stainless steel	
	v_m (m/s)	ΔT (ms)	v_m (m/s)	ΔT (ms)
0.3	0.1251±0.0043	0.1967±0.0013	0.1402±0.0076	0.1919±0.0019
0.4	0.1796±0.0083	0.1841±0.0015	0.1868±0.0104	0.1831±0.0013
0.5	0.1833±0.0123	0.1817±0.0096	0.1912±0.0019	0.1800±0.0012

3.2.2.2 Numerical analysis

As shown in Fig. 20, the particle velocity-time responses of four different groups marked in Fig. 18(b) are compared. Group 1: stainless steel ($2R$ = 20 mm) and brass ($2R$ = 14.8 mm) granular chains; Group 2: aluminum ($2R$ = 61.1 mm) and Delrin ($2R$ = 23.1 mm) granular chains; Group 3: glass ($2R$ = 95.32 mm) and nylon ($2R$ = 41.56 mm) granular chains; Group 4: zinc ($2R$ = 112.9 mm) and PMMA ($2R$ = 55.16 mm) granular chains. Note that all the granular chains (composed of 10 particles) discussed here are excited with the same type of dynamic loading (impacted by a striker with a velocity of 0.4 m/s). Consequently, the equivalent performance of the two selected systems is demonstrated.

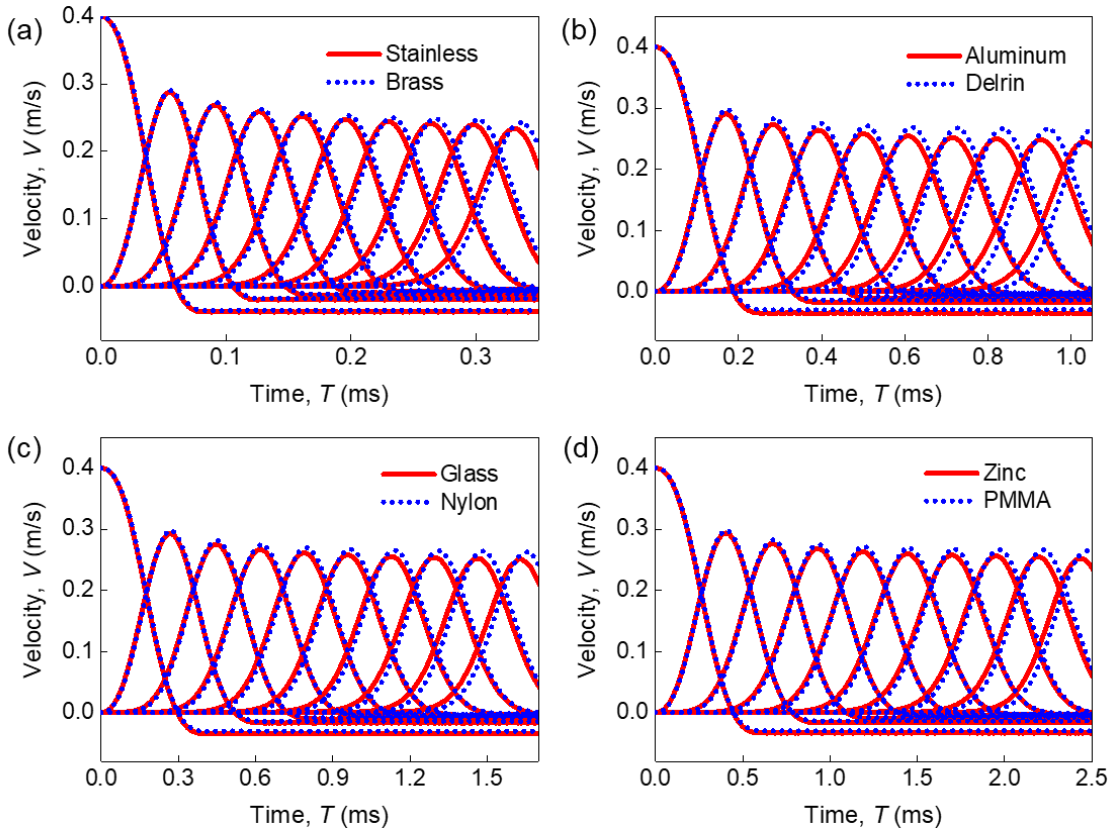

Figure 20 Numerical results (particle velocity-time curve) of generalized equivalent systems. (a) Group 1; (b) Group 2; (c) Group 3; (d) Group 4.

3.2.3 Restricted equivalent system

3.2.3.1 Experimental results

The experimental results of restricted equivalent systems are shown in Fig. 21. where the slight decay in the amplitude of the 10th particle is observed. It is probably related to the friction and tiny gap between the particles during the experiments. Here, the phase speed of the Nesterenko solitary wave is selected as the evaluation criterion, which can be easily obtained by considering the interval between two specific particles.

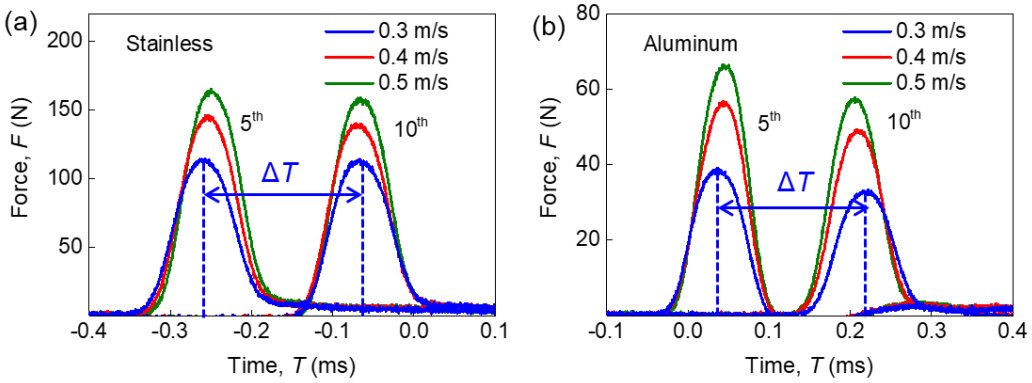

Figure 21 Experimental results of restricted equivalent systems. Force-time curves of 5^{th} and 10^{th} particles in (a) 1D stainless steel granular chain and (b) 1D aluminum granular chain at three different impact velocities (0.3 m/s, 0.4 m/s, 0.5 m/s)

Table 5 shows the experimental phase speed of Nesterenko solitary waves in 1D stainless and aluminum granular systems under different impact velocities. All the phase speeds are obtained by measuring the time interval and distance ($10R$) between 5^{th} and 10^{th} particles in granular chains. Except for the dissipative effect in experiments (APPENDIX E), 1D stainless steel and aluminum granular systems can be regarded as restricted equivalent systems.

Table 5 Phase speed of restricted equivalent systems under different impact velocities.

Impact velocity (m/s)	0.3	0.4	0.5
Stainless steel (m/s)	521.25±5.16	546.08±3.80	555.58±3.65
Aluminum (m/s)	539.91±13.77	598.22±8.85	621.06±11.15

3.2.3.2 Numerical analysis

Four groups of materials with similar 1D elastic wave speeds are selected to construct restricted equivalent systems. Group 1: PP and ABS granular chains ($2R$ = 5.67 mm); Group 2: Delrin and PMMA granular chains ($2R$ = 7.64 mm); Group 3: titanium and nickel

granular chains ($2R$ = 20 mm); Group 4: magnesium and glass granular chains ($2R$ = 20 mm). Each granular chain consists of 10 particles. Figure 22 displays the particle velocity-time responses of these four groups, where the excellent agreement of two granular systems is found in each group. It is evident that the two granular systems in each group appear in the same location in the mechanism map (Fig. 18), indicating that restricted equivalent systems can be regarded as a specific group of generalized equivalent systems. In addition, the return pass in equivalent systems is numerically explored (APPENDIX F) to discuss the effect of other properties (e.g., reflected waves).

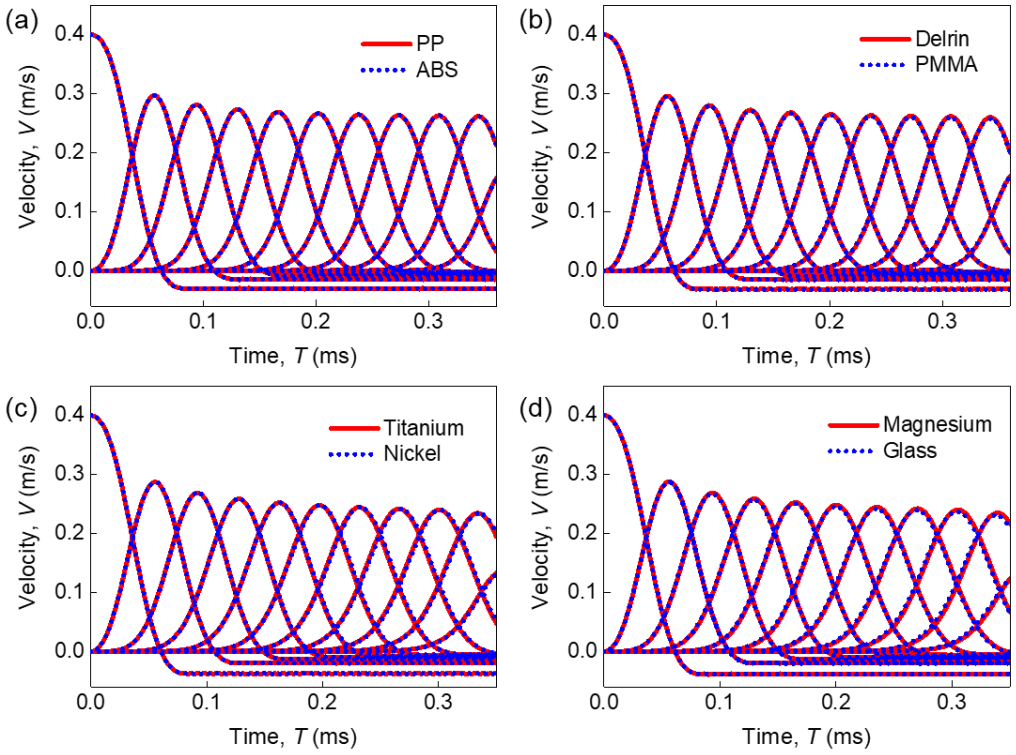

Figure 22 Numerical results (particle velocity-time curve) of restricted equivalent systems. (a) Group 1; (b) Group 2; (c) Group 3; (d) Group 4.

In summary, both the experimental and numerical results strongly support that by following the established models, one can obtain equivalent systems according to the specific system design requirement. Thus, such a mechanism map shown in Fig. 18 may extensively serve as an instruction providing insights for engineers to design a granular system.

3.3 Conclusions

In this chapter, the construction of Nesterenko solitary wave in equivalent systems (1D spherical granular chains) was studied. Theoretical models were established to offer a featured methodology for designing both generalized and restricted equivalent systems. Furthermore, a mechanism map containing both the geometric parameters and material properties was developed, serving as a guideline for engineers to develop corresponding equivalent systems. Numerical simulation and experimental work both strongly supported the validity of proposed models. Consequently, this work expands the understanding of governing factors in wave tuning. It also offers novel ideas for designing 1D nonlinear systems with tailored properties, especially when the available material type or particle size is limited.

CHAPTER 4 STRESS WAVE ATTENUATION IN 1D GRANULAR SYSTEMS

In this chapter, efficient and controllable stress wave attenuation approaches are developed by considering I. Strain-softening behaviors; II. Kirigami-based structures. In the first approach, a hollow cylindrical (HC) granular system is reported to support highly tunable compression and rarefaction waves by varying the particle thickness ratio. Soliton-like and mitigating waves are observed in the proposed granular chain with strain hardening and softening contact behaviors, respectively. Moreover, validated FE models describing the contact behaviors and wave dynamics are adopted and specific relation between the contact behavior (i.e., nonlinear exponent) and geometric parameter (i.e., thickness ratio) is analyzed. The tunability of 1D HC granular chains is demonstrated by carrying out parametric studies for governing factors, including the impact velocity, impactor-to-particle mass ratio, particle thickness ratio, and particle number. An optimal impact mitigating efficiency can be obtained within a quite short chain, which is exceedingly favorable for the design and construction of impact mitigation systems. Results provide a novel design and methodology for various wave tuning and mitigation purposes.

In the second approach, the kirigami lanterns are tailored and fabricated using simple paper sheets yet an exceptional impact mitigation capability is achieved (orders of magnitude lower transmission compared to various existing metamaterials). Detailed experimental and numerical exploration uncovers that the unique folding-unfolding motion

of kirigami lanterns during stress wave propagation contributes to the outstanding performances. Based on a validated FE model, the governing laws of critical parameters, including impact energy, cell number, petal number, and hinge number, are systematically explored, where the mitigation capacity can be further boosted by appropriately increasing the impact energy. Furthermore, an adaptable design of kirigami chain length and other geometric parameters is exploited to realize highly efficient and controllable mitigation when subjected to specific impact energy. This study illustrates a new route to designing superior impact mitigation structures with lightweight materials, offering insights for the innovation of next-generation impact protection strategies in the automotive and aerospace industries.

4.1 Tunable traveling wave properties in 1D chains composed from hollow cylinders

4.1.1 Materials and methods

4.1.1.1 Experimental setups

A 1D HC granular chain with N = 20 particles was vertically assembled in a 3D-printed tube composed of a series of enclosures (using standard grey resin in Formlabs Form 2) (Fig. 23(a)). The inner diameter of the tube was 19.50 mm, which was designed to restrict the lateral movements of HC particles and to minimize the transitional friction. The thickness ratio of HC particle is defined as R/t (Note that R is fixed here and various R/t can be achieved by varying t, see the side inset of Fig. 23(a)) and the particles (diameter

$2R$ = 19.05 mm, thickness ratio R/t = 5.77, mass m = 5.00 g, Young's modulus E_c = 68.90 GPa and Poisson's ratio ν_c = 0.33 [86]) were cut from a standard 6061-T6 aluminum round tube (McMaster-Carr).

Propagating waves were generated by impacting the top of the 1D granular chain and the impactor was released from a specific height, resulting in an impact velocity of 0.30 m/s to the granular chain (PTFE ball, $2R_s$ = 15.88 mm, M = 4.50 g, E_s = 1.46 GPa, ν_s = 0.46 [20]). The impactor triggered a photoelectric sensor (OMRON, E3Z), serving as an external input by connecting the sensor to the oscilloscope. Under a specific loading scenario (i.e., same impact velocity and mass), the actual time difference can be obtained corresponding to various locations of the film sensor such that the stress wave propagation can be precisely captured. Further details for obtaining the waveforms are in APPENDIX G.

Combined with an amplifier (LK1432C) and the oscilloscope (Tektronix, TDS-2024C), a film sensor bonded between two HC particles was used to detect and record the waveform of contact force during the tests. Compared to the aluminum HC particles in the chain, the thickness (0.30 mm) and mass (< 5%m) of the film sensor were negligible such that the measurement of contact force waveforms between two interacting particles would be acceptable. Two tests per experimental setup were conducted to ensure the repeatability of the experiments.

Similar to Ref. [14], this film sensor was calibrated by comparing the area under the force-time curve (from the initial point to the peak) captured by the sensor to the linear momentum of the particle. The sensitivity of the film sensor K_s upon low-speed tests was 20.00 pC/N. Thus, the sensitivity of the amplifier K_o was set to 2.00 pC/unit, and the output voltage per unit O was 1.00 mV/unit accordingly. The contact force (F) corresponding to the output voltage (U) from the oscilloscope is given by Eq. (44) [13].

To investigate the contact properties between the two HC particles, a 3D-printed hollow cubic box (inner length 19.10 mm) was designed to restrict the lateral motions of two vertically aligned particles (Fig. 23(b)). A quasi-static loading (0.20 mm/min) test was conducted on the INSTRON E3000 material testing machine to obtain the force-displacement relation. Herein, two repeated tests were performed to achieve consistency and accuracy.

4.1.1.2 Finite element model

A three-dimensional FE model of the HC granular chain is developed in ABAQUS/Explicit (Fig. 23(c)). A rigid wall (fixed at the end of the granular chain) and a cubic tube (for lateral constraints) are constructed to simulate the base and guide in the experiment, respectively. Only elastic properties are considered in this study, consistent with the experimental setups.

For neighboring particles, the surface-to-surface contact type with a frictionless property is applied in the tangential direction. A 10-node modified quadratic tetrahedron element (C3D10M) is used for both the impactor and particles in the granular chain. The convergence study is conducted to ensure the proper mesh size (APPENDIX H). A mesh size of 1.00 mm is selected for the particle to balance the computational costs and accuracy. Considering the thin wall for HC particles with large thickness ratios, at least two layers of elements are seeded along the thickness direction. Meanwhile, a gradient mesh (0.30-1.50 mm) is set for the impactor varying from the contact point to the middle plane of the sphere [59]. The effect of gravity is fully included in FE models to ensure the accuracy of the experiment setups (APPENDIX I).

As for the contact behaviors of neighboring particles, a three-dimensional HC contact model is constructed based on ABAQUS/Standard (Fig. 23(b)). A rigid platen is positioned at the top of the two particles by using a displacement control (the maximum displacement is set to 0.30 mm), while the bottom rigid platen is fixed. The lateral movements of particles are constrained to simulate the 1D quasi-static compressive test. A 10-node-quadratic tetrahedron standard mesh type (C3D10) is selected for the two interacting particles, and the mesh size is 0.50 mm which corresponds to the order of the maximum displacement set for compressive loading. The contact type and material properties are consistent with the settings in the granular chain model discussed above.

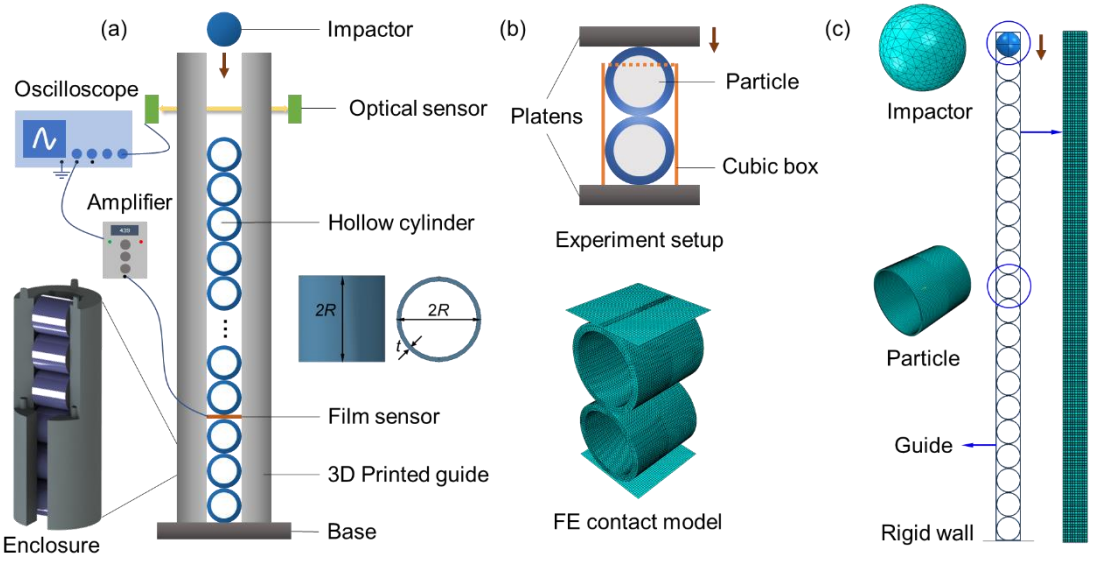

Figure 23 Schematic of setups. (a) Experimental setups of the proposed 1D HC granular chain. (b) Experimental setups and FE models were developed to investigate the contact properties between HC particles. A 3D-printed cubic box was adopted to keep two HC particles vertically aligned in experiments. (c) FE model of the 1D HC granular chain, which is consistent with the settings in experiments.

4.1.2 Results

Firstly, the quasi-static compression results from two HC cylinders are obtained (Fig. 24(a), where tests 1 and 2 refer to two repeated tests) and a power-law type relation is applied to approximately describe the contact force (F) and the elastic deformation (d) [1]:

$$F = kd^n, \tag{45}$$

where k is the contact coefficient and n is the power-law exponent (for interacting spherical particles; the power-law equation will evolve into Hertz contact, i.e., n = 3/2). Combined with experimental and numerical results, the fitting curve (the dotted green line in Fig. 24(a) with a strain-softening exponent n = 0.985 < 1) demonstrates the validity of the

power-law approximation in HC granular systems. However, the power-law exponent of contacting solid cylinders is 1.15 reported in Ref. [42] and 1.11 in Ref. [111], respectively which indicates that one may expand the tunable space to a large extent by varying the thickness ratio of HC particles (where $R/t = 1$ refers to the solid cylindrical particle). Based on the results of granular chain tests (Fig. 24(b)), a mild waveform expansion phenomenon can be observed. Meanwhile, the numerical results agree well with the experimental ones, proving the reliability of the numerical models for investigating the tunable stress waves in various HC granular chains.

A baseline model is proposed and analyzed to explore the typical wave properties in HC granular chains, with an impact velocity of $V_i = 0.1$ m/s, a thickness ratio of $R/t = 20$, an impactor-to-particle mass ratio of $M/m = 1$, and a total particle number of $N = 20$. The particle force is obtained from measured contact forces between neighboring particles identically to the method used in [14]. Meanwhile, the nondimensional kinetic energy (KE*) is defined as KE*(N^{th})/ KE_m (1^{st}) (KE_m (1^{st}) is the maximum kinetic energy of the 1^{st} particle) to ensure a fair comparison among granular systems with different parameters. In force/energy surface maps, the results of the impactor are not considered for a better understanding of the stress wave transmission within the 1D HC granular chain.

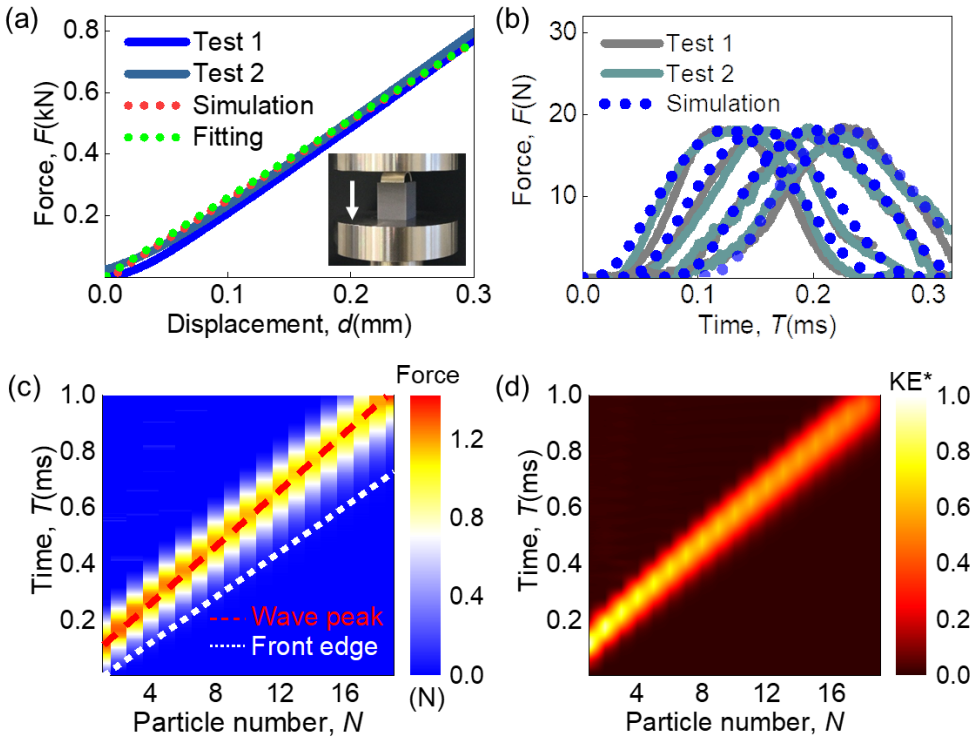

Figure 24 Typical results. (a) Contact behaviors of HC granular crystals ($2R$ = 19.05 mm, R/t = 5.77). A 3D-printed box was applied to ensure purely vertical displacement during the experiments. (b) Validation of the FE granular chain model. Contact forces at four different positions (i.e., the 1st and 2nd particles, the 3rd and 4th particles, the 6th and 7th particles, the 8th and 9th particles) obtained from the experiment and numerical simulation are compared. (c) Particle force and (d) Nondimensional kinetic energy maps in time and space domains from the numerical simulation. The red dashed and white dotted lines represent the wave peak and front edge of the stress wave during the propagation process, respectively.

An increasing separation among wave peaks (the red dashed line) and the front edge (the white dotted line) can be observed in Fig. 24(c), which is consistent with the results from hollow elliptical cylinder chains in Ref. [18]. The shape of the leading pulse tends to be wider and lower as the stress wave propagates, which results in a long wave tail at the end of the granular chain. Inevitably, there is an evident increase in the particle force values

close to the distal end because of the fixed rigid wall. With the evolution of the normalized energy in Fig. 24(d), the amplitude of nondimensional kinetic energy gradually decreases and the waveform becomes wider (corresponding to the features of the particle force) which is evidence of the formation of a typical rarefaction wave.

Unlike the Nesterenko compression solitary waves previously discussed in traditional granular systems, e.g., spherical granular chains [6, 55], these unique characteristics (especially the variation of stress waves from compact to sparse distribution) yield the potential mitigation mechanism of 1D HC granular systems. The fundamental difference regarding stress wave properties comes from the distinct contact properties among various granular chains.

4.1.3 Discussion

A parametric study is numerically carried out by analyzing the effects of different governing parameters. In addition to the thickness ratio introduced in the previous section, three other critical parameters are considered, including the impact velocity (V_i), the total particle number (N), and the impactor-to-particle mass ratio (defined as M/m, various density values of the impactor are adopted to achieve desired mass ratio in FE models).

4.1.3.1 The effect of impact velocity

Given the fact that the yield velocity of aluminum is $V_Y = Y_c / \sqrt{E_c \rho_c} = 19.80$ m/s (Y_c is the yield strength of 6061-T6 aluminum) [112, 113], the impact velocity range (0.1-1 m/s)

is set below the yield velocity to achieve purely elastic stress waves in the granular chains. Meanwhile, the dynamic deformation of a hollow cylinder is demonstrated to be local and elastic when the impact velocity is less than $0.2V_Y$ [112]. Thus, numerical simulations (R/t = 20, M/m = 1 and N = 20) were conducted upon three different impact velocities, i.e., 0.1 m/s, 0.5 m/s and 1 m/s, respectively. The demonstration of elastic assumption is further investigated in APPENDIX J. Three characteristic parameters are defined to quantitatively investigate the various wave amplitudes at different impact velocities on 1D HC granular chain (Fig. 25(a)), i.e., the temporal width T_s, wave speed V_s, and wave width L_s. Here, T_s is the time difference between two specific points (5% maximum force) of a hump (blue hump in Fig. 25(a)). V_s is given by the ratio of the spatial distance between two crests to the corresponding temporal distance (ΔT). Since the variation of V_s is negligible in given short HC chains (N = 20) [18], the constant wave speed is considered during the wave propagation by using the humps of the 6^{th} and 11^{th} particles for each loading scenario. Consequently, the wave width (or characteristic spatial width) can be defined as $L_s = T_s V_s$ to describe the pulse profiles as the stress wave propagates.

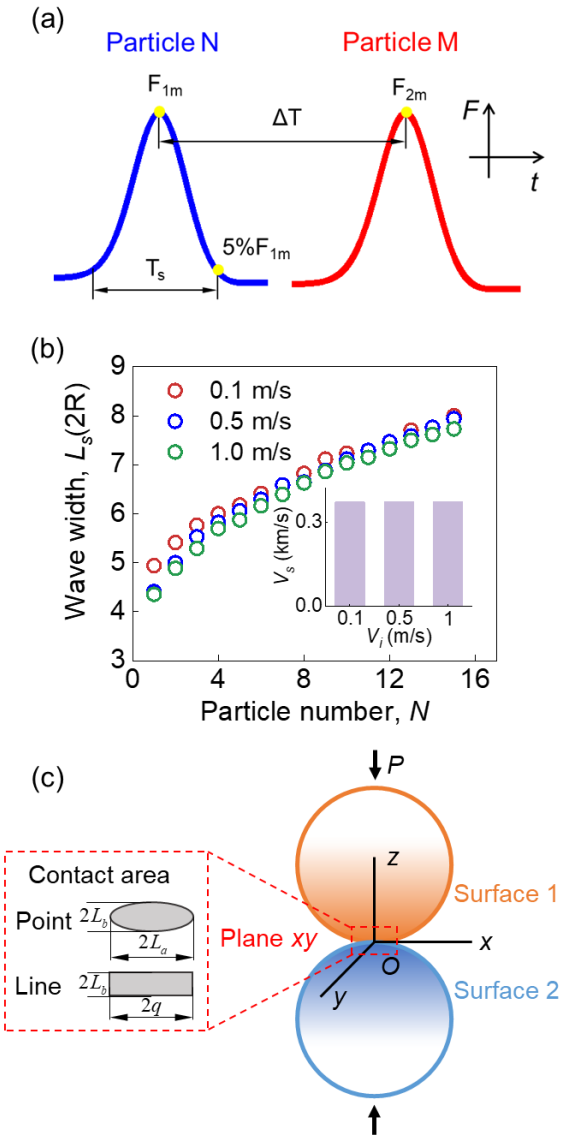

Figure 25 Effects of impact velocities. (a) Definitions of characteristic parameters in stress wave propagation. (b) Wave width variation in space domain under different impact velocities. The inset shows wave speeds of different cases. (c) The geometry of the contact region corresponding to two contact types: point contact (sphere-to-sphere) and line contact (cylinder-to-cylinder).

Generally, when one applies higher external excitation to a traditional spherical chain, the wave speed of the resultant Nesterenko solitary wave tends to increase and is

demonstrated to have a relation of $V_s \sim v_m^{1/5}$, where v_m is the maximum particle velocity, which is directly related to the impact velocity [1]. However, this is not the case for a 1D HC chain. Identical wave speed is observed regardless of external excitations (see the inset of Fig. 25(b)). This unique feature of the designed HC chains results from the unconventional contact behaviors of HC particles (the exponent being very close to 1). This appears to be consistent with the phenomena observed in solid cylindrical chains (0^o orientation aligned) [42].

A point contact is obtained for interacting spherical particles, i.e., the initial contact is a single point without external load, and applying load will lead to a finite elliptical contact area (Fig. 25(c)) [38]. The pressure distribution in plane *xy*, $p(x, y)$ can be described by [114]

$$p(x,y) = \frac{3P}{2\pi L_a L_b}\left(1 - \frac{x^2}{L_a^2} - \frac{y^2}{L_b^2}\right)^{1/2}, \tag{46}$$

where P is the load, L_a and L_b are the two semi-axes of the elliptical area in Fig. 25(c). This leads to the Hertzian contact relation between the P and d [1]

$$P = \frac{2E}{3\left(1-\nu^2\right)}\left(\frac{R_1 R_2}{R_1 + R_2}\right)^{1/2} d^{3/2}, \tag{47}$$

where E and ν represent Young's modulus and Poisson's ratio, while R_1 and R_2 are the radii of two particles, respectively.

For neighboring HC particles parallel to each other, the point contact will evolve into a line contact. In that case, an elongated rectangle will substitute the elliptical contact area as the load is applied, resulting in an infinite L_a. If both L_a and P are close to infinity, P/L_a will remain finite. Thus, by allowing the major axis to become infinite, one may determine the load per unit $\bar{P}$ instead of P to achieve the load-displacement relation for line contact, which gives [114]

$$d = 4\bar{P}\frac{\left(1-\nu^2\right)}{\pi E}\left[\left(1+\ln 4\right)/2+\ln 2q-\ln L_b\right], \tag{48}$$

where $2q$ is the length of the rectangular contact region and $\ln L_b$ can be obtained by

$$\ln L_b = \frac{1}{2}\ln\left[4\bar{P}\frac{\left(1-\nu^2\right)}{\pi E}\frac{2R_1R_2}{R_1+R_2}\right]. \tag{49}$$

Unlike the point contact case, the load-displacement relation for the line contact cannot be solved explicitly. The length of the contact area ($2q$) will keep constant with the increase of wave amplitude (or the impact velocity). With the exponent being very close to 1, the dependence of Nesterenko solitary wave speed on its amplitude would be rather small (unlike being 1/5 for exponent 3/2 for Hertzian interaction of spherical beads [1]), making the dependence of wave speed on amplitude very weak and non-observable. In other words, the HC granular chains can deliver stress waves with amplitude-independent wave speed.

Another interesting feature that can be observed in Fig. 25(b) is that the variation of waveforms (i.e., wave width) shows a similar trend under different impact velocities. The wave width, for the case with R/t = 20, M/m = 1, and N = 20, increases from about 9R to 16R as the stress wave propagates, which is notably different from that of Nesterenko solitary waves in spherical granular chains (~10R) [1, 45]. This is also due to the exponent being very close to 1. According to Eq. 1.130 in Ref. [1], the characteristic spatial scale of the Nesterenko solitary wave can be larger than 10R if the exponent is close to 1.

Furthermore, an outstanding force mitigation effect can be observed in all cases (Fig. 26). While evaluating the effectiveness of force mitigation, it is quite straightforward to define a force mitigation ratio $\mu(N^{\text{th}}) = F_{Nm}/F_{1m}$ (the subscripts "N" and "m" denote the specific particle number and maximum, respectively) in the space domain and make a fair comparison among cases with different impact velocities. A specific ratio $\mu(16^{\text{th}})$ is adopted to evaluate the force mitigation effect among these cases. Herein, $\mu(16^{\text{th}})$ has values of 75.50%, 67.37% and 62.08% for loading scenarios with impact velocities of 0.1 m/s, 0.5 m/s and 1 m/s, respectively. Namely, the force mitigation effect tends to be enhanced as the external excitation increases. Note that the ratios of the last four particles are not considered to avoid the influence of the rigid wall (or the reflected waves). An additional case with a higher impact velocity is also discussed in APPENDIX K to demonstrate the universality of existing results.

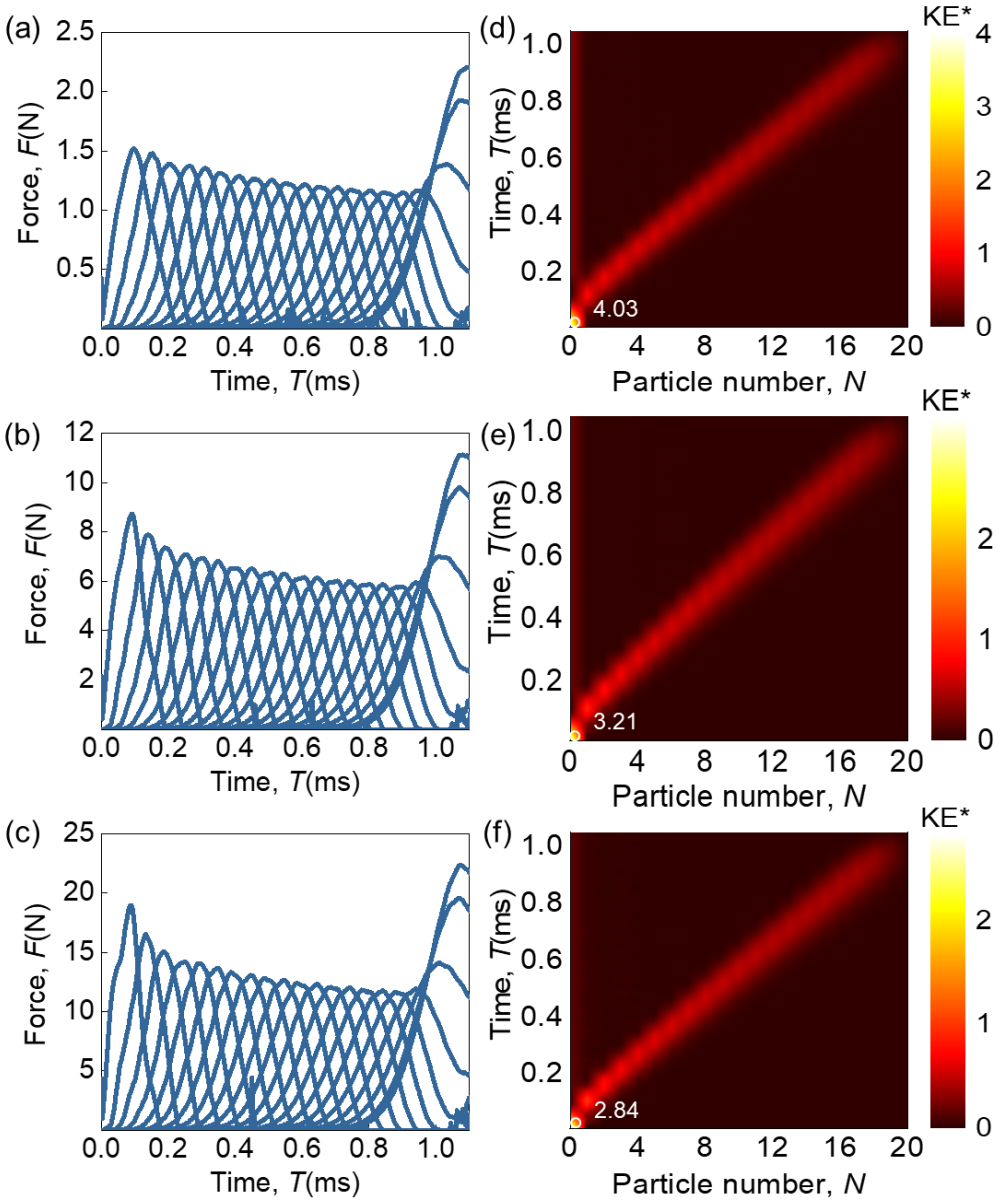

Figure 26 Contact forces of different particles (R/t = 20, M/m = 1, N = 20) illustrate stress wave propagation under the impact velocity of (a) 0.1 m/s, (b) 0.5 m/s and (c) 1 m/s. Nondimensional kinetic energy maps were plotted to investigate energy transmission in HC granular chains under different impact velocities: (d) 0.1 m/s, (e) 0.5 m/s, and (f) 1 m/s. The input energies of each system, i.e., the initial kinetic energy of the impactor, were marked by white circles in the energy maps.

The KE* of the impactor (i.e., the input energy, marked as white circles) is included in the energy map to further assess the energy transmission within a 1D HC granular chain (Figs. 26(d)-(f)). The rebound of the impactor is less evident in those cases with higher impact velocities. Therefore, one may achieve an increasing wave width together with decreasing wave amplitude in 1D HC granular chains, making them potential mitigating systems.

4.1.3.2 The effect of impactor-to-particle mass ratio

In addition to the wave amplitude (or impact velocity), the duration of impulses can have a substantial effect on the traveling waves within granular chains as well [1]. Various impactor-to-particle mass ratios ranging from 0.2 to 10 are selected to generate a series of impulse durations (M/m = 0.2, 0.5, 1, 2, 3, 4, 5, 10, and R/t = 20, V_i = 0.1 m/s, N = 20).

According to the evolutions of leading waveforms in Fig. 27, a larger impactor-to-particle mass ratio (i.e., a longer initial excitation) gives wider leading waveforms while decreasing wave duration makes them converge to a specific width (~3 elements for this case). Note that a “short (< 0.2 ms)” or “long (> 0.2 ms)” duration can lead to a train of solitary waves or shock wave impulse for traditional “sonic vacuum” type granular systems, respectively [14].

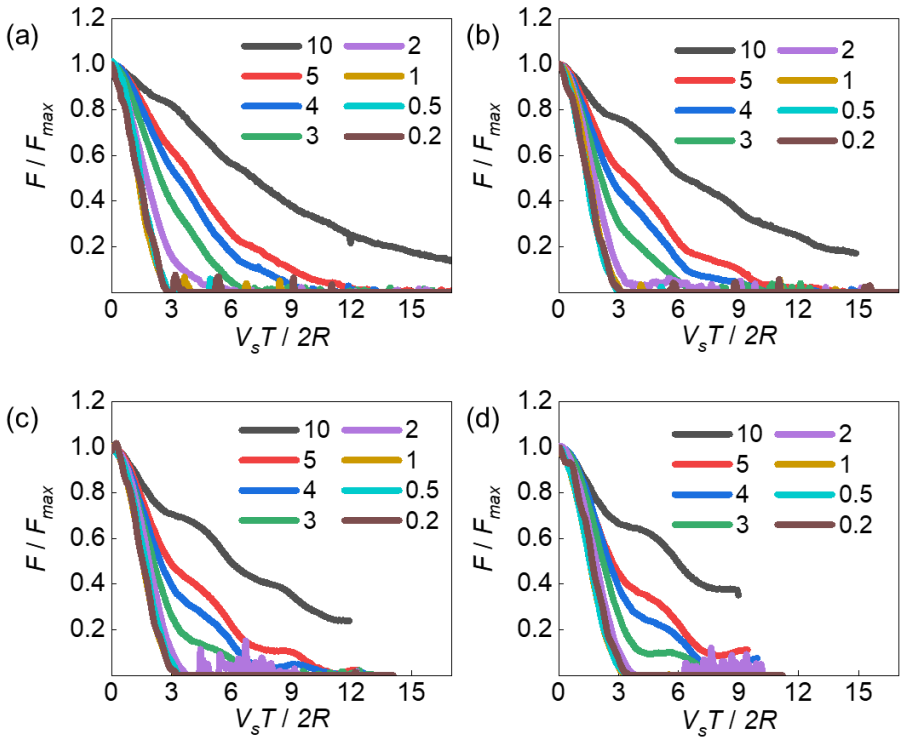

Figure 27 The evolution of leading waveforms at different spatial positions (R/t = 20, V_i = 0.1 m/s, N = 20): (a) N = 3, (b) N = 6, (c) N = 9, (d) N = 12. The normalized force (F/F_{max}) is plotted versus nondimensional time ($V_sT/2R$) and the right halves of the curves have been shifted to the origin for comparison.

The durations of impulses relating to different impactor-to-particle mass ratios are evaluated in Table 6 to explore the wave duration-induced behaviors. For those cases with impactor-to-particle mass ratios higher than 1 (or impulse duration larger than 0.2 ms), a long wave tail is observed in HC chains, resulting in an asymmetric waveform in the corresponding granular chains. This serves as more evidence of the wave mitigation and wave dispersion of traveling shock waves in 1D HC chains. Moreover, for small impactor-to-particle mass ratios (or impulse duration lower than 0.2 ms), there is no long wave tail

and the nondimensional time tends to be convergent owing to the short interacting period among granular particles.

Table 6 Durations corresponding to different impactor-to-particle mass ratios

Mass ratios	0.2	0.5	1	2	3	4	5	10
Duration (ms)	0.108	0.153	0.213	0.333	0.432	0.558	0.660	1.194

4.1.3.3 The effect of thickness ratio

Based on the validated contact model, the varying contact properties of HC particles are analyzed with thickness ratio R/t ranging from 1 to 20. Following the power-law presented in Eq. (45), different groups of critical parameter values (k, n) are obtained corresponding to each thickness ratio (Fig. 28). It is notable that both $n > 1$ and $n < 1$ can be achieved here, and an approximately inverse proportional trend can be observed between the thickness ratio (R/t) and power-law parameters (n). To classify all scenarios into two groups, i.e., $n > 1$ and $n < 1$, a dashed red line is marked in Fig. 28, indicating the boundary between the strain-hardening and softening systems.

Given different properties in these two classes of materials, four typical HC granular systems with thickness ratios R/t = 2, 4, 16, and 20 are selected. Note that Nesterenko solitary wave solution is valid even for slightly nonlinear material ($n \rightarrow 1$) cases, i.e., the nonlinear power law is close to the linear contact law [1]. In that case, the effective strain-hardening group consists of granular systems with thickness ratio R/t = 2, 4, while the other two cases (R/t = 16, 20) are in the strain-softening group. This also implies it is possible to

achieve highly tunable traveling wave properties (e.g., switching from compression to rarefaction) via adjusting the thickness ratio of the particles in 1D HC granular chains.

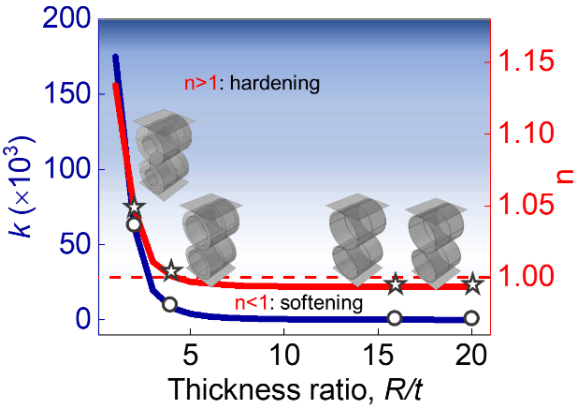

Figure 28 Contact behaviors of HC granular crystals with a thickness ratio R/t varying from 1 to 20. The behaviors of HC granular chains can switch from strain-hardening to softening based on different values of exponent n. Four thickness ratios (R/t = 2, 4, 16, 20, star markers in the graph) were selected to investigate the tunable wave properties.

Results from two classes of HC granular chains (strain-hardening and softening) are compared to further verify the analysis of contact behaviors. According to the evolution of contact force with different thickness ratios (Fig. 29), significant differences in the stress waveforms are revealed between the two groups. The traveling waves within the strain-hardening group (R/t = 2, 4) show soliton-like properties while mitigating rarefaction waves are formed in the strain-softening group (R/t = 16, 20). This is more evident when comparing the force mitigation ratios ($\mu(16^{th})$) of these cases in Table 7, where the force amplitude remains constant in the strain-hardening group while it shows a decreasing trend

in the strain-softening group. Meanwhile, the force mitigation ratio is closely related to the thickness ratio, i.e., a higher thickness ratio gives a superior mitigating effect.

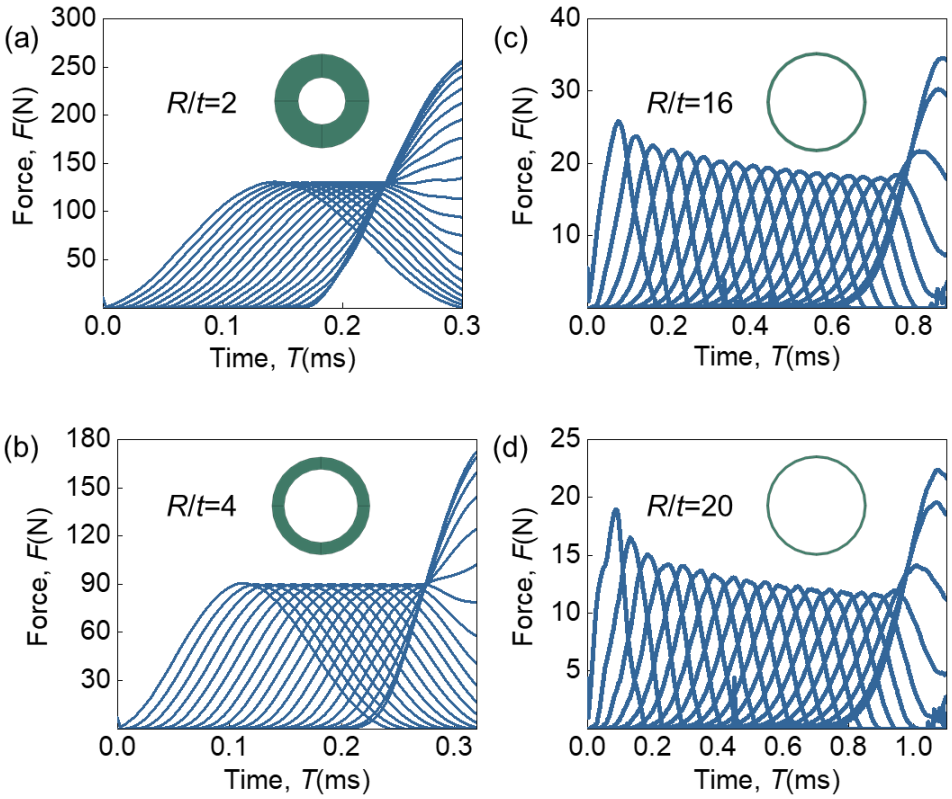

Figure 29 Wave propagation in 1D HC granular chains with different thickness ratios (M/m = *1*, V_i = 1 m/s, N = 20): (a) R/t = 2, (b) R/t = 4, (c) R/t = 16, (d) R/t = 20.

Furthermore, mitigating properties are investigated via the nondimensional kinetic energy of particles with different R/t (Fig. 30(a)). The wave width in the spatial domain is calculated, yielding that the strain-hardening group supports traveling waves without profile variation (Fig. 30(b)) while expanded waveforms in the strain-softening group are observed (Fig. 30(c)). Given wave width at specific spatial positions (e.g., N^* = 4), it decreases as the increase of thickness ratio (corresponding to the decrease of exponent n).

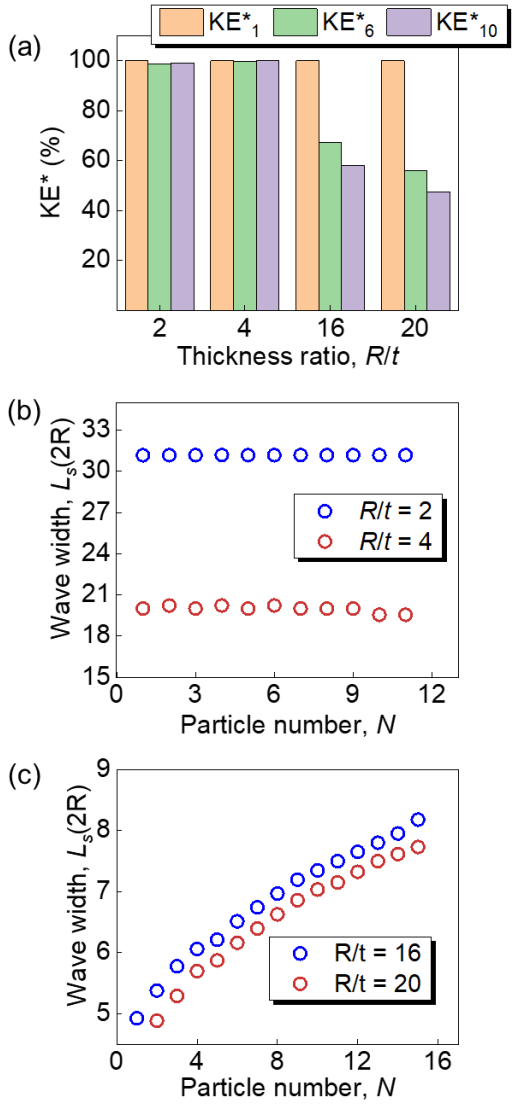

Figure 30 Effects of thickness ratios. (a) The nondimensional kinetic energy of particles with different thickness ratios. Three positions (1st, 6th, and 10th) were considered. Wave widths of 1D HC granular chains with (b) low and (c) high thickness ratios.

Table 7 The force mitigation ratios of 1D HC chains with different thickness ratios

HC granular chains	Strain-hardening group		Strain-softening group	
Thickness ratio (*R/t*)	2	4	16	20
Force mitigation ratios, $\mu(16^{th})$	97.43%	97.93%	70.23%	62.08%

4.1.3.4 The effect of particle number

Based on established numerical models, an HC granular chain (R/t = 20, M/m = 1, V_i = 0.1 m/s) with 50 particles is simulated to explore the force mitigation effects in terms of the chain length, and the force mitigation ratio μ is calculated in the spatial domain as shown in Fig. 31(a) (i.e., for every single particle in this HC chain). A power-law function is used to track the spatial trend:

$$\mu = yN^z, \tag{50}$$

where y and z are critical constants of the fitting curve.

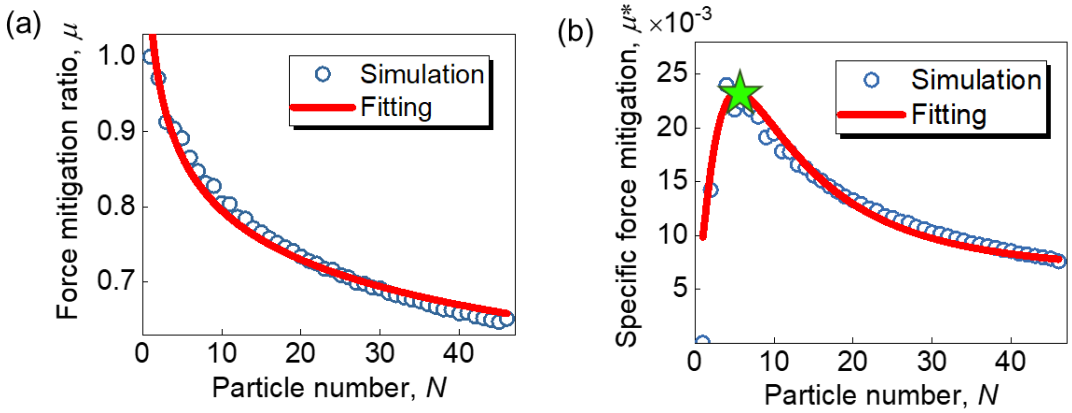

Figure 31 Effects of particle numbers. A 1D HC granular chain (R/t = 20, M/m = 1, V_i = 0.1 m/s) with particle number N = 50 was considered. (a) Force mitigation (defined as F_{Nm}/F_{1m}) decreases as the stress wave propagates. (b) Specific force mitigation variation shows that good specific mitigation results can be achieved within a very short chain (~5.46 particles in this case).

In addition, a specific force mitigation factor is defined as $\mu^* = (1-\mu)/N^*$, where N^* represents the specific spatial position for each particle in the HC chain. The specific force mitigation is calculated in the spatial domain and a log-normal distribution is adopted to describe the variation accordingly (Fig. 31(b)):

$$\mu^* = \mu_0 + \frac{B}{\sqrt{2\pi}wN} e^{\frac{-\left(\ln\frac{N}{Nb}\right)^2}{2w^2}}, \tag{51}$$

where B, b, w, and μ_0 are fitting constants.

A peak value of μ^* is discovered around the spatial position of 5.46 particles (as marked by a star in Fig. 31(b)). With a longer HC chain, one will achieve better mitigating effects but not necessarily the optimal mitigating efficiency. To explore the effects of the wave amplitude and duration, the corresponding spatial distances with optimal mitigating efficiency are evaluated under various impact velocities (N = 20, R/t = 20, M/m = 1) and impactor-to-particle mass ratios (N = 20, R/t = 20, V_i = 0.1 m/s) in Table 8.

Table 8 Amplitude and duration induced spatial positions of optimal mitigating efficiency

Optimal efficiency	Impact velocity (m/s)		
	0.1	0.5	1
Spatial distance (particles)	5.46	4.06	3.37
Optimal efficiency	Impactor-to-particle mass ratio		
	0.1	0.5	1
Spatial distance (particles)	3.19	4.56	5.46

A decreasing trend of spatial distance (from 5.46 to 3.37 particles) is observed as the impact velocity increases, indicating that one may achieve the optimal mitigating efficiency in a shorter granular chain under higher wave amplitudes. Furthermore, the spatial distance of the optimal mitigating efficiency will increase as the impactor-to-particle mass ratio increases (from 3.19 to 5.46 particles). While for a higher impactor-to-particle mass ratio (e.g., M/m = 5), the spatial distance (18 particles) is close to the total

length of the granular chain (20 particles). This is induced by the longer interaction period among granular particles under larger mass ratios (or wave duration).

The optimized mitigation effect can be achieved within a short HC granular chain, which is of great significance to the design of the granular system and manifests great potential in engineering applications.

4.1.4 Conclusions

In this study, both soliton-like compression and mitigating rarefaction waves were investigated within 1D HC granular chains, where different contact behaviors (i.e., $n > 1$ and $n < 1$) were achieved by tuning the thickness ratios of the particles. Owing to the unique contact properties of HC particles, a consistent wave speed for each HC granular chain was observed upon different external excitations. Furthermore, wider leading waveforms followed by a long wave tail were demonstrated in cases with large impactor-to-particle mass ratios which corresponded to a longer impulse duration. Finally, an optimized mitigating efficiency was achieved in a short distance by analyzing specific mitigating effects in the space domain of a longer chain ($N = 50$). The high tunability and novel features of the proposed HC granular systems provide insights into mitigating granular system design and understanding of unprecedented nonlinear phenomena.

4.2 Kirigami-based lantern chain for superior impact mitigation

4.2.1 Methods

4.2.1.1 Kirigami fabrication

Inspired by classic paper lanterns for the Chinese New Year, watercolor paper sheets with a thickness of 0.47 mm and a density of 300 g/m^2 (Strathmore, 300 series, cold press) were used to fabricate single kirigami lanterns (Fig. 32(a)). One may start with a rectangular paper sheet (height H = 60 mm, length L = 80 mm) tailored by a paper cutting machine. A pre-cut was designed and applied along the horizontal midline before folding the paper sheet in half (lengthwise) to accurately create the central crease lines for each kirigami lantern. Subsequently, a horizontal stop line and evenly distributed vertical cutting lines were drawn on the folded paper sheet to indicate the cutting plane and length for each kirigami lantern. Note that the cutting length is fixed (i.e., h = 20 mm) for all kirigami lanterns, and the number of cutting lines/planes directly relates to the petal number of kirigami lanterns. After cutting all slits, the paper sheet was unfolded and transformed into a lantern by gluing the edges (Gorilla micro precise super glue gel) and forming it into a tubular shape. Following the fabrication of kirigami lanterns, a cylindrical plastic panel was carefully designed (ID = 11.5 mm, OD = 40 mm, and t = 2 mm), 3D-printed (Form 2, Tough 1500 resin), and glued to both the top and bottom edges of the cell, making it possible to connect different kirigami lanterns and construct a 1D kirigami-based lantern chain (Fig. 32(a)).

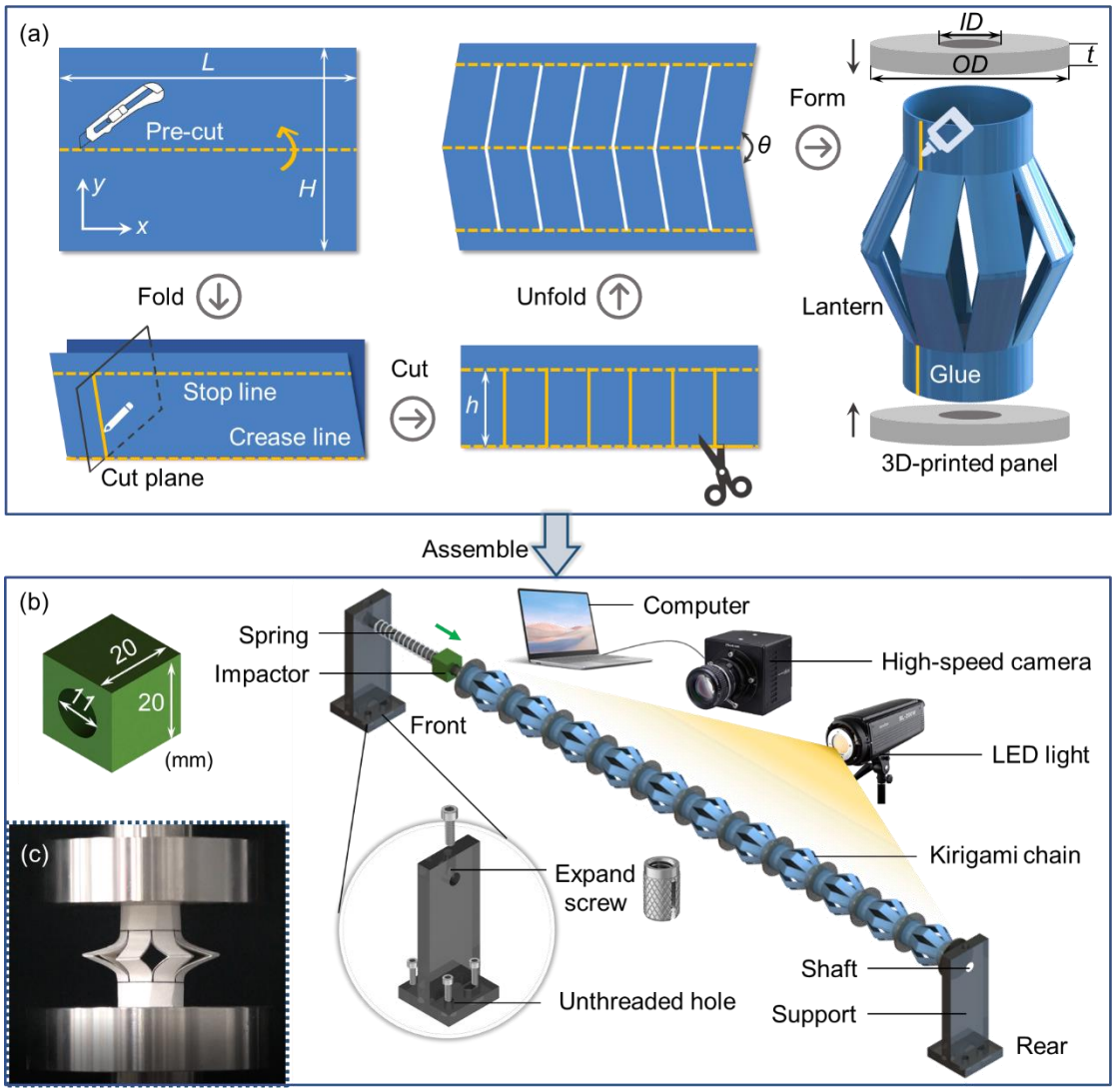

Figure 32 (a) Fabrication process of a single kirigami lantern; (b) Schematic of the setup for impact experiments. An expand screw was inserted into the top of two supports to fix the round shaft. Four unthreaded holes were designed at the base to secure the supports on the optical table. Both the cubic impactor and kirigami lanterns can freely slide along the shaft; (c) Cyclic tests on kirigami lanterns for preconditioning.

4.2.1.2 Experimental setup

For investigation on the dynamics of the 1D kirigami-based lantern chain, 11 kirigami lanterns were horizontally aligned on a round shaft with a diameter of 10 mm (McMaster-

Carr, polished 304 stainless steel), which was placed on two 3D-printed supports (Fig. 32(b)). The last kirigami lantern of the chain ($N = 11$) was fixed to the rear support (serving as a rigid wall). Meanwhile, both supports were secured on an optical table with vibration isolation (Newport) and two compression springs were attached to the front support (McMaster-Carr, 316 stainless steel, rate 0.31 N/mm, 80.5 mm long, 13.5 mm outer diameter, and 11.5 mm inner diameter). By fully compressing the springs, a 3D-printed cubic impactor can be ejected and in turn impact the 1D kirigami-based lantern chain, namely, the conversion of the elastic potential energy of springs to the kinetic energy of the impactor can generate an initial impulse.

For capturing the dynamic responses (e.g., deformation modes and motions) of kirigami lanterns, a high-speed camera (Photron, FASTCAM Mini UX100) was set up at the same height level of the 1D kirigami-based lantern chain, which was then connected to a laptop for visualization and control. Furthermore, an LED video light (Godox SL200 W) was adopted to guarantee a high light brightness environment for the camera during experiments. The high-speed camera was triggered for data acquisition (4000 fps) as the impactor was ejected by the springs, enabling us to record the initiation and propagation of stress waves within the chain.

Considering that all the kirigami lanterns were hand-fabricated, the folding behaviors and mechanical performance may vary among different cells, making it difficult to explore

the reliable responses of the whole kirigami lantern chain [115]. Thus, a preconditioning process, including 200 cycles of loading-unloading (frequency 2 Hz, amplitude 10 mm) based on INSTRON E3000 material testing machine, was carried out on each kirigami lantern to ensure repeatable and uniform folding behaviors during the dynamic tests (Fig. 32(c)).

4.2.1.3 Finite element model

According to the experimental setup (Fig. 33(a)), a three-dimensional FE model is developed in ABAQUS/Explicit to comprehensively investigate the dynamic responses of the proposed 1D kirigami lantern chain (Fig. 33(b)). Note that the round shaft and two supports are neglected in the FE model for necessary simplification. Accordingly, all the kirigami lanterns and panels are tied together while a surface-to-surface contact (hard contact for normal behavior and frictionless tangential property) is adopted to describe the interaction between the impactor and the first panel. Furthermore, a general contact is also defined for the whole FE model since there may exist self-contact in kirigami lanterns under relatively large deformation. Only axial deformation is allowed to mimic the 1D motion status of the chain in experiments and the last panel of the chain is fixed. Converted from the elastic potential energy of the springs, an initial velocity of 13.39 m/s is assigned to the cubic impactor for generating an identical initial impulse as experiments.

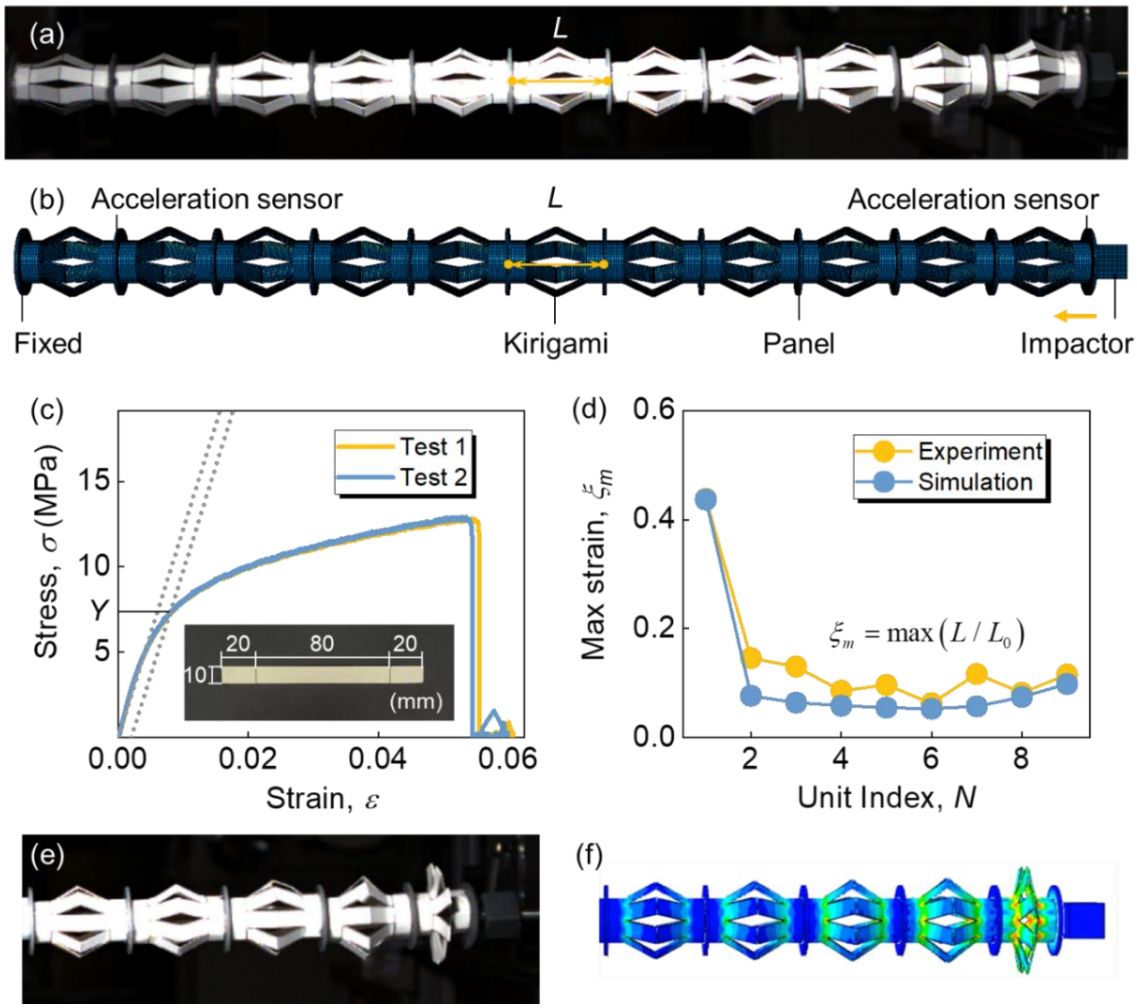

Figure 33 (a) Experimental setup captured by the high-speed camera; (b) FE model; (c) Quasi-static tensile testing of the watercolor paper specimens used in fabrication. Young's modulus and yield strength can be obtained from the elastic stage and 0.2% plastic strain offset respectively; (d) Comparison of the maximum nominal strain between experimental and numerical results; Deformation modes from the (e) experiment and (f) simulation.

Both the 3D-printed panels and the cubic impactor are made from Tough 1500 resin with post-curing and the corresponding material properties are given by the manufacturer (Formlabs), i.e., the density of 1150 kg/m^3, Young's modulus of 1.5 GPa, and Poisson's

ratio of 0.4. A quasi-static tensile test of paper strip specimens was carried out on the INSTRON E3000 material testing machine with a loading rate of 5 mm/min (two repeated tests) to characterize the material properties of the watercolor paper sheets used for kirigami lanterns in experiments. Stress-strain relations yield Young's modulus of 1.22 GPa and yield strength of 7.31 MPa (Fig. 33(c)). Thus, an elastic-plastic model is used to characterize the constitutive behaviors of the paper materials in the FE model.

Herein, an 8-node linear brick element type with reduced integration (C3D8R) is used and the mesh sizes of the cubic impactor, kirigami lantern, and panel are 1 mm, 1.5 mm, and 1 mm respectively to balance the computational costs and accuracy. Particularly, the mesh near the crease lines of kirigami lanterns is refined to achieve a denser mesh distribution at critical areas. Two acceleration sensors are set on the first and last kirigami lanterns (located at the center of front panels) to capture the input and output axial acceleration-time curves, respectively.

4.2.1.4 Model validation

During the impact tests, the motion and deformation of kirigami cells can be traced by measuring the length variation of each kirigami lantern at different frames. A nominal strain is then defined as L / L_0 in view of the actual length (L) and original length (L_0) of kirigami lanterns. The maximum nominal strain (ξ_m) of each kirigami lantern is compared between the experiment and simulation to validate the developed FE model, where a good

agreement is achieved with sufficient accuracy (Fig. 33(d)). Also, the experimental (Fig. 33(e)) and numerical (Fig. 33(f)) deformation modes match well with each other. The slight discrepancy may be attributed to possible distortion in experimental measurement and the friction between the round shaft and components.

Furthermore, the reusability of the tailored 1D kirigami lantern chain is investigated by applying five repeated impacts sequentially (Appendix L). Compared to the first impact, an increase of ξ_m in the first few kirigami lanterns (especially the first one) is found during the following impacts (Fig. 66), which manifests that the kirigami lantern may experience plastic deformations during the first impact. Specifically, permanent deformation formed in the first impact leads to a decrease of the kirigami lantern's overall length and in turn produces a more prominent buckling upon repeated impacts (with identical input energy). A more systematic discussion about the plastic deformation after impact will be presented in section 4.2.3 via numerical simulations. Nevertheless, the proposed 1D kirigami lantern chain is competent in the reusable challenge, thereby overcoming the trade-off between impact mitigation capability and material efficiency in traditional impact protection materials.

4.2.2 Results

Based on the validated FE model, the impact mitigation performances of the 1D kirigami lantern chain are evaluated and a critical indicator, i.e., transmission, is defined as

the ratio between the maximum output and input accelerations (Fig. 34(a)). Toward understanding the transmission behaviors of the 1D kirigami lantern chain, the representative input and output accelerations-time curves under impact energy of 1.6 J are presented (Fig. 34(b)), where both waveforms are normalized by the maximum input acceleration.

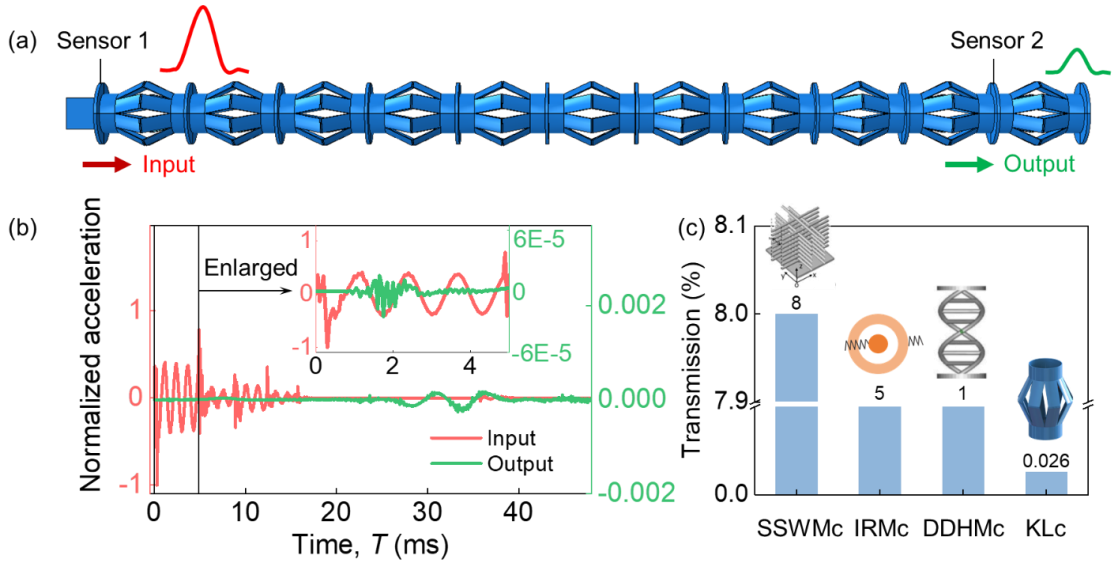

Figure 34 (a) Definition of transmission ratio; (b) Acceleration (normalized by the maximum input acceleration) of input and output waves under impact energy of 1.6 J (corresponding to an impact velocity of 21.17 m/s); (c) Comparison of transmission ratio of the kirigami lantern chain (KLc) with existing structures from previous publications (The impact energy is 1.6 J). Note that an axis break is added at 7.9% due to the large difference between the transmission values of the structures.

Regarding the input wave, a strong shock with high amplitudes appears at the beginning stage, following which an obvious and fast impact wave attenuation is observed after about 10 ms. However, the output wave behaves differently and possesses a rather low amplitude during the whole process. More specifically, after the kirigami lantern chain

is impacted, a minor oscillation of the output wave arises rapidly due to the overall structural response (see the enlarged view of the first 5 ms). As the stress wave further propagates within the 1D kirigami lantern chain and eventually arrives at the last kirigami lantern, a major peak can be found, followed by additional peaks resulting from the reflective waves (the interaction between the input waves and the fixed end).

Compared to various existing metamaterials from previous literature (Fig. 34(c)), including sandwich structure woodpile metamaterials (SSWMc) [116, 117], internal resonator metamaterials (IRMc) [118, 119], and DNA-inspired metamaterials (DDHMc) [120], the transmission of the proposed 1D kirigami lantern chain (KLc) is two orders of magnitude lower than other metamaterials (0.026%) under the same impact energy of 1.6 J, indicating a superior impact mitigation performance. Therefore, one may use lightweight materials (e.g., paper sheets) to achieve outstanding mitigation effects via delicately structural design, which is especially essential for aerospace and automotive industries.

4.2.3 Discussion

4.2.3.1 Impact energy

The mitigation performances of the 1D kirigami lantern chain under a variety of impact energies ranging from 0.13 J to 1.60 J (Fig. 35) are analyzed to comprehensively investigate the impact mitigation mechanisms. With the increase of the impact energy, the transmission will decrease rapidly at the beginning stage, whereas the decreasing rate is

lower as the impact energy further grows (Fig. 35(a)), demonstrating that an enhanced impact mitigation capability can be achieved in the 1D kirigami lantern chain under higher impact energy. The folding-unfolding law of kirigami lanterns in the chain may fundamentally account for the underlying mechanisms of impact mitigation. Notably, the folding pattern of the first two kirigami lanterns exhibits different characteristics at ξ_m (the insets of Fig. 35(a)), where a more distinct compression is observed in the first kirigami lantern (N = 1) under higher impact energy while the second kirigami lantern (N = 2) maintains a constant folding deformation until the impact energy reaches a rather high level (1.60 J).

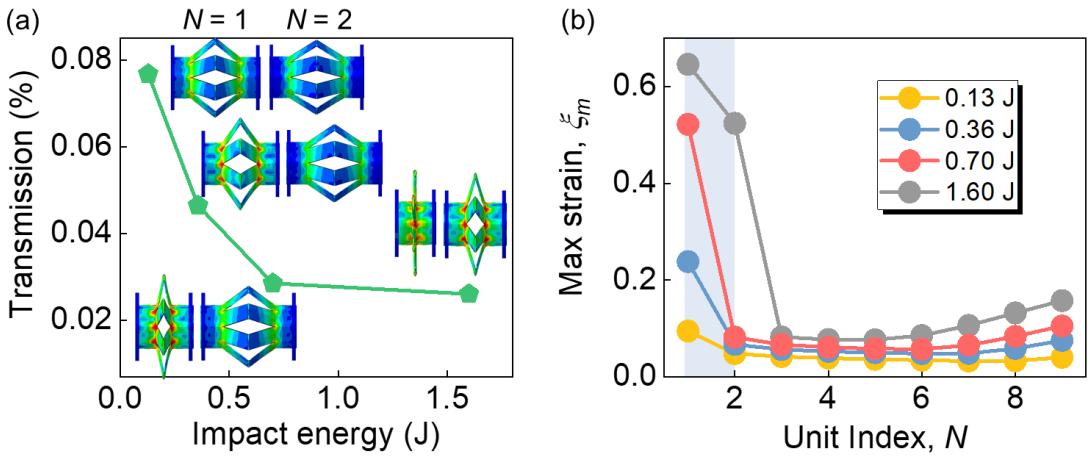

Figure 35 The effect of impact energy. (a) The variation of transmission as impact energy increases from 0.13 J to 1.60 J. The insets exhibit the deformation modes of the 1st and 2nd kirigami cells at ξ_m during the stress wave propagation. (b) The evolution of ξ_m with respect to unit index under different impact energies.

To quantify the folding patterns of kirigami lanterns across the chain, one may explore the evolution of ξ_m as a function of the unit index (N) under different impact energies

(Fig. 35(b)). Except for the case with an impact energy of 1.6 J, all the curves undergo a rapid transition from a large folding deformation in the first kirigami lantern to much smaller deformations in the following kirigami lanterns, accompanied by a slight increase of deformation near the fixed end. Nevertheless, under impact energy of 1.6 J, the above transition occurs after the second kirigami lantern, which is consistent with the observation of the progressively folding pattern in Fig. 35(a).

Revisiting the definition of nominal strain in section 4.2.1.4, the allowed ξ_m in the kirigami lantern is theoretically determined, i.e., $[L_0 - (H\text{-}2h)]/L_0 = 0.64$, revealing that there may exist critical impact energy. At this point, the first kirigami lantern is fully buckled after impacts and presents a maximum nominal strain of 0.64. When exceeding the threshold, the buckling of the first kirigami lantern cannot withstand the additional energy, giving rise to the apparent buckling of the second kirigami lantern. By analogy, the folding characteristics of the subsequent kirigami lanterns may vary if the impact energy further increases, implying that one may customize the required length of 1D kirigami chain aiming at a specific impact energy to achieve more efficient and adaptive impact mitigation.

Based on the complete waveforms of the first four kirigami lanterns (Fig. 36), a clearer picture of the exclusive impact mitigation mechanism is uncovered, where three crucial conclusions can be made: 1. Consistent with experimental observations, a residual

deformation (denoted by the blue arrows) is found in kirigami lanterns close to the impact end and higher impact energy yields larger residual deformation, demonstrating that part of the input energy is dissipated by plastic deformations of the paper materials; 2. An expanded waveform with decreasing amplitude may effectively mitigate the impact during stress wave propagation in 1D kirigami lantern chains. Meanwhile, a wider waveform tends to emerge to accommodate higher impact energy, which is identical to the conclusions of conventional 1D granular systems [1, 50]; 3. Owing to the continuously folding-unfolding motion of kirigami lanterns (corresponding to the compressive-tensile deformations), a series of oscillating tails appears on the waveforms, which allows energy redistribution and storage in kirigami lanterns through elastic deformations. Consequently, the integration of these three mitigation mechanisms contributes to outstanding impact mitigation performances in 1D kirigami lantern chains.

Moreover, multiple peaks can be observed on the waveforms due to repeated contacts between the cubic impactor and the first kirigami lantern, resulting in more complicated dynamic responses of the 1D kirigami lantern chain. For instance, the slight increase of ξ_m near the fixed end (Fig. 35(b)) may be attributed to the reflective waves and accumulative input energy coming from repeated impacts.

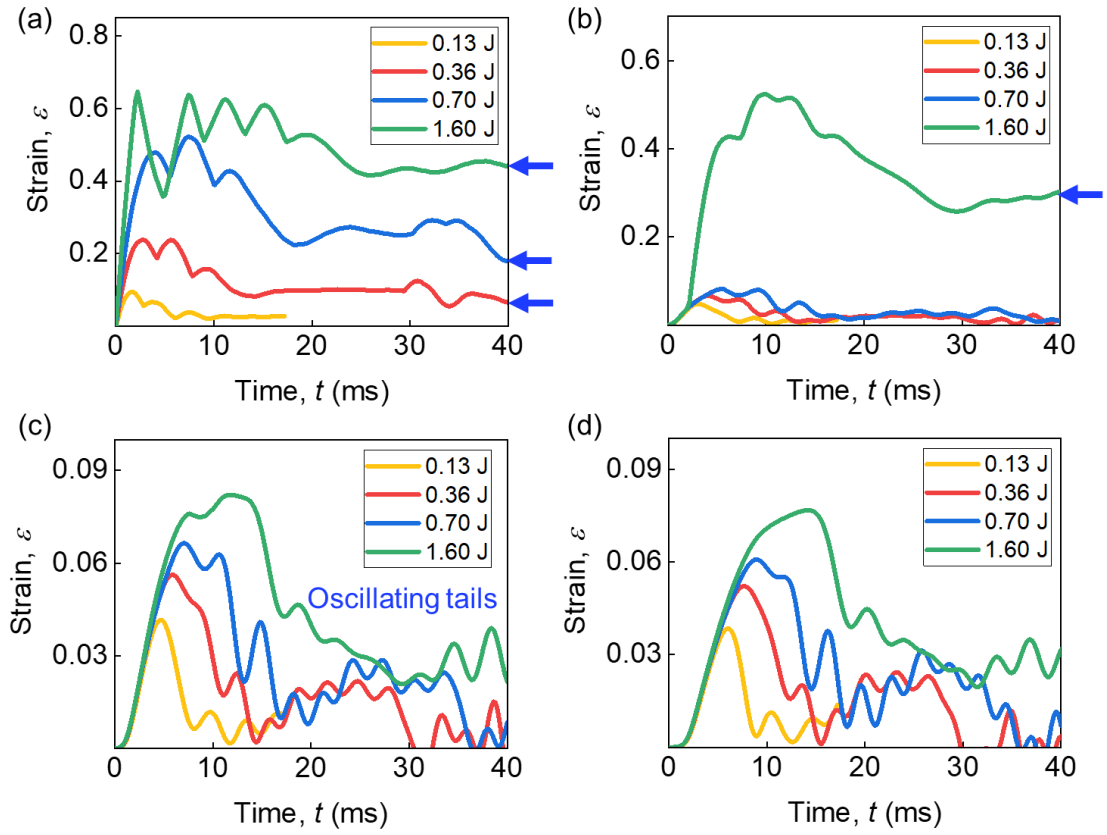

Figure 36 The evolution of nominal strain in the first four kirigami lanterns during stress wave propagation. (a) N = 1; (b) N = 2; (c) N = 3; (d) N = 4.

4.2.3.2 Cell number

The effect of kirigami lantern chain length is further explored by considering different cell numbers under the same impact energy of 0.64 J (coinciding with experimental setups). Inspired by the characteristic spatial width of the wave perturbation in conventional 1D granular systems [1, 50], a 25% wave width L_s (measured by the full width at 25% maximum and normalized by the original length of kirigami lantern L_0, Fig. 37(a)) is defined to eliminate the influence of oscillating wave tails and thus characterize the

dominant spatial size of stress waves. Accordingly, L_s of the 2nd kirigami lantern is measured and analyzed for all the kirigami lantern chains in this study for a fair comparison. Considering that the input acceleration may be different in kirigami lantern chains with various configurations, a normalized input is given by the maximum input acceleration ratio between specific kirigami lantern chains and the baseline discussed in section 4.2.1.4 (11 cells and 0.64 J impact energy).

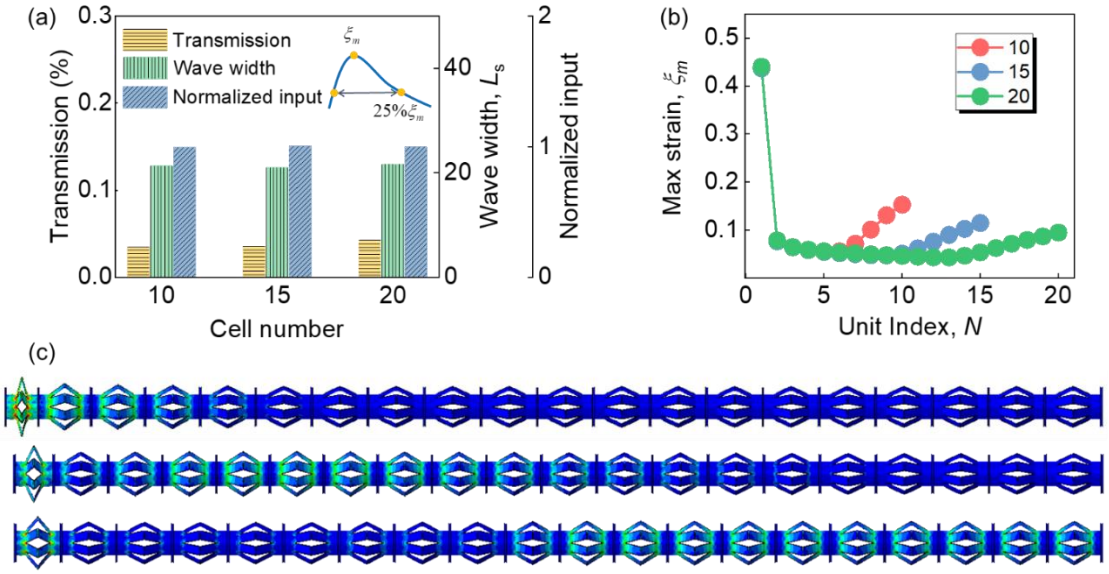

Figure 37 Comparison of (a) transmission, wave width, normalized input amplitude, and (b) maximum strain of the kirigami chains with different cell numbers. (c) Deformation modes of the kirigami lantern chain with 20 cells at different times (From top to the bottom: 4 ms, 12 ms, and 20 ms).

Remarkably, when the cell number varies from 10 to 20, the overall dynamic responses keep consistent among kirigami lantern chains despite a minor increase of transmission in the case with 20 kirigami lanterns (Fig. 37(a)), confirming that a relatively

short chain can fulfill the impact mitigation yet maintain quite a low transmission. When the kirigami lantern chain is further shortened, the transmission may grow sharply and become much higher than those of long chains. Even if the transmission rises to 0.16% in a 5-kirigami lantern chain (4.5 times that in a 10-kirigami lantern chain), it is still highly competitive and efficient in contrast to existing impact protection materials.

Deformation behaviors of kirigami lantern chains with different cell numbers are compared as well (Fig. 37(b)), where the general trends of ξ_m for different chains overlap in kirigami lanterns neighboring the impact end, yet the kirigami lanterns close to the fixed end behave differently. The increase of cell number can largely alleviate the eventual increase of ξ_m in 1D kirigami lantern chains owing to the redistribution of accumulative energy from multiple impacts. The detailed folding-unfolding deformations of the 1D kirigami lantern chain with 20 cells at different time points (Fig. 37(c)) verify the efficacy of kirigami lantern chains in impact mitigation again. Namely, the residual deformation in the first few kirigami lanterns and a wide wave profile may produce a combination of plastic and dispersive effects for efficient impact mitigation.

4.2.3.3 Petal number

During the fabrication process of kirigami lanterns, the petal number can be altered by selecting an appropriate spacing distance between different cutting lines (the petal number of the baseline is 8 in Fig. 32(a)), and thereby change the dynamic responses of 1D

chains (e.g., the critical buckling force). It is natural to explore how the petal number affects the impact mitigation performance of 1D kirigami lantern chains. Herein, three types of kirigami lanterns are considered with a petal number of 6, 8, and 10, respectively, where a superior mitigation performance is obtained in 1D kirigami lantern chains with a higher petal number (Fig. 38(a)).

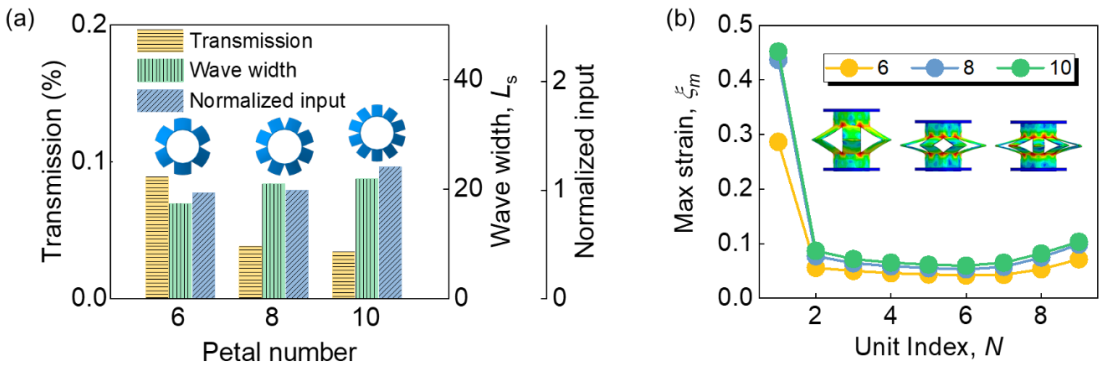

Figure 38 Comparison of (a) transmission, wave width, normalized input amplitude, and (b) maximum nominal strain of the kirigami chains with different petal numbers.

Given an exact paper sheet for fabrication, a lower petal number leads to a wider area for each petal (i.e., more materials on each petal) and subsequently a higher critical buckling force of the kirigami lanterns, making it more difficult to trigger the buckling of these cells. Thus, even if the kirigami chains are subjected to identical impact loading, a lower normalized input (Fig. 38(a)) and nominal strain amplitude (Fig. 38(b)) are observed in the configuration with a petal number of 6. Meanwhile, a relatively narrow wave width is also formed, whereas it may further limit the impact mitigation performance.

Although the increase of the petal number can effectively improve the mitigation capability of 1D kirigami lantern chains to some extent, this law is not applicable when the petal number is continuously increasing. With each petal being ultra-narrow under a rather high petal number. these kirigami lanterns are not capable of withstanding the impact force, eventually resulting in a high transmission. For instance, the transmission of a kirigami lantern chain with a petal number of 16 reaches 0.2 %. Therefore, it is possible to achieve an optimal petal number of kirigami lanterns for specific impact energies.

4.2.3.4 Hinge number

The folding-unfolding deformation of kirigami lanterns during stress wave propagation plays a significant role in impact mitigation, which impels us to explore the influencing law of hinge number N_h. Based on the fabricated kirigami lantern with $N_h = 1$ (Fig. 39(a)), two multi-layered kirigami lanterns with $N_h = 2$ (Fig. 39(b)) and $N_h = 3$ (Fig. 39(c)) are tailored, where the initial hinge angle θ and the original length L_0 are kept consistent among different kirigami lanterns. In comparison to the baseline, the resulting mass difference between these kirigami cells is as low as 2% and can be neglected (Fig. 39(b)). With additional hinges in a single kirigami lantern under higher N_h, one may intuitively anticipate a superior impact mitigation capability. However, unlike improved mechanical characteristics obtained in traditional multi-layered/hierarchical structures [21,

121], the increase in hinge number of kirigami cells contrarily restricts the mitigation performance of the 1D kirigami lantern chain (Fig. 39(b)).

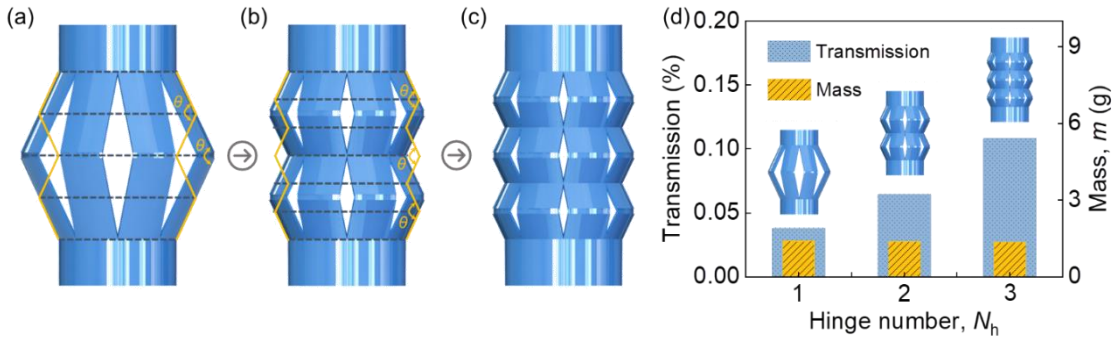

Figure 39 Configuration of kirigami cells with different hinge numbers (N_h): (a) N_h = 1; (b) N_h = 2; (c) N_h = 3. (d) Comparison of transmission (blue columns) and mass of unit cell (yellow columns) in kirigami chains with different N_h.

In consideration of the identical mass and initial hinge angle, the normalized input shows a minor discrepancy in different configurations under impact energy of 0.64 J (Fig. 40(a)), whereas a sequentially buckling behavior is triggered within each kirigami lantern when $N_h > 1$ (insets of Fig. 40(b)). Originated from the multi-layered structures, the total allowable buckling deformation for each hinge is reduced and not all hinges can fully buckle during the stress wave propagation (e.g., the intermediate hinge of kirigami lanterns with $N_h = 3$), bringing about lower wave width (Fig. 40(a)) and folding-unfolding deformation (Fig. 40(b)) under a higher hinge number. Therefore, the detrimental effect on mitigation capacity is primarily ascribed to the reducing mitigation efficiency with the growth of N_h. Namely, the proposed 1D kirigami lantern chains may yield an exceptional

impact mitigation performance with a simpler design, corroborating the concept of "less is more" in structural design.

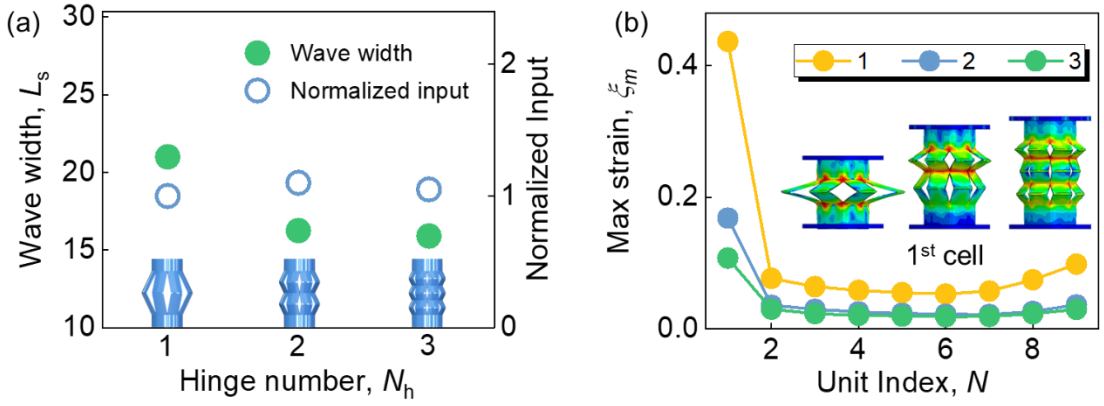

Figure 40 (a) Wave width and normalized input of the kirigami chains with different N_h. (b) The evolution of the maximum nominal strain of the kirigami chains during stress wave propagation.

4.2.4 Conclusion

In this paper, the stress wave propagation in a 1D kirigami lantern chain that can be simply fabricated from flat paper sheets was experimentally and numerically explored. The unique folding-unfolding motions of kirigami lanterns resulted in an enhanced impact mitigation capability (transmission < 0.1%), which is orders of magnitude lower than that of metamaterials reported in previous publications. The fundamental mechanism lay in the integration of plastic deformation of kirigami lanterns and redistribution/storage of elastic energy. A comprehensive parametric study indicated that the impact mitigation capability can be further improved under higher impact energy. Also, by carefully structured kirigami lantern chains, it is possible to offer a controllable and efficient impact mitigation strategy

for customized tasks in engineering, paving a new way to designing effective yet lightweight impact protection materials.

CHAPTER 5 TUNABILITY OF STRESS WAVE PROPAGATION IN 1D GRANULAR SYSTEMS

In this chapter, a 1D cylindrical granular system is designed, where solitary wave tuning strategies can be achieved through mass, modulus, and thickness mismatch. The experiment setups are vertically established to observe the basic solitary wave traveling behavior as well as to validate the numerical simulation model. By considering the three governing wave tuning strategies, i.e., mass, modulus, and thickness mismatch, the relations between the compression ratio and the mismatch values of different indicators are parametrically explored. Based on the simple single-layer 1D chain, a multi-layered 1D chain is further designed where the middle layers serve as tuning layers such that both ‘‘strong-weak’’ and ‘‘weak–strong’’ interfaces are created. A full tuning range is obtained by coupling different strategies based on the multilayer granular chains. Particularly, for a single layer granular chain, a mechanism map is established according to a normalized Ashby plot and numerical results of compression ratios, providing insights into precisely designing highly intelligent and efficient wave attenuation systems.

5.1 Method

5.1.1 1D granular chain setups

A 1D cylindrical granular chain is designed to attest and evaluate the performance of different solitary wave tuning strategies (Fig. 41). Three parts, i.e., launching part, tuning part, and receiving part, together compose the granular chain. Each part has ten particles in

total, where two topological interfaces “strong-weak” and “weak-strong” are created (Fig. 41). Identical particles in both launching and receiving parts are assigned with the brass material (i.e., $\rho_1 = \rho_3$, $E_1 = E_3$, $t_1 = t_3$) with the tuning part changeable to create the mismatch. A sphere serves as the impactor to generate impulses, and a guide is set to ensure the 1D motion of cylindrical particles. Furthermore, to make a fair comparison among different strategies, the compression ratio α_c is defined as an evaluation indicator, i.e., $\alpha_c = F_3 / F_1$, where F_1 and F_3 are the contact force amplitudes obtained between the first two particles in launching and receiving parts, respectively. A lower compression ratio represents a superior solitary wave attenuation effect.

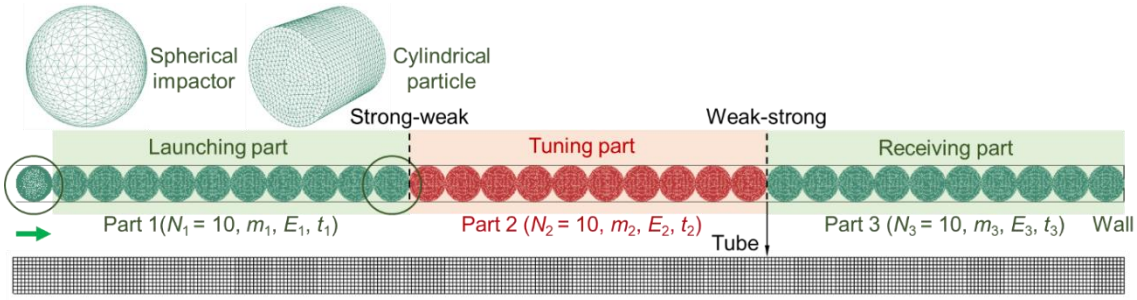

Figure 41 Configurations of the proposed solitary wave tuning strategies and a three-dimensional FE model of the cylindrical granular chain. Parts 1, 2, and 3 represent the launching part, tuning part and receiving part, respectively. Two distinct types of interfaces, “strong-weak” and “weak-strong”, are marked as black dashed lines accordingly.

5.1.2 Configurations of solitary wave tuning strategies

Three wave tuning strategies, including mass mismatch, modulus mismatch, and thickness mismatch are developed corresponding to the mismatch of critical indicators, i.e.,

the mass m, Young's modulus E, and the thickness t of cylindrical particles. For solid cylindrical particles, $t = R_s$, where R_s is the radius of the solid cylinder.

Firstly, to obtain a mass mismatch, the density of particles in the tuning part (ρ_2) is varying while Young's moduli and thicknesses are kept identical to the brass material used in launching and receiving parts. Similarly, the settings of configurations with a modulus mismatch are achieved with the varying indicator E_2 while keeping the other two variables the same. Note that all the particles in configurations with a mass or modulus mismatch are solid cylinders. As for a thickness mismatch, the thickness of particles in the launching part and the tuning part is fixed to $t_{1,3} = 3.175$ mm, and t_2 is changing. Since the thickness mismatch can lead to different particle volumes, ρ_2 is adjusted accordingly for each case to obtain equivalent mass properties in different parts, and Young's modulus is still consistent in all three parts (i.e., $E_1 = E_2 = E_3$).

5.1.3 Finite element modeling

Based on ABAQUS/Explicit, an FE model of the cylindrical granular chain is constructed to investigate the stress wave behaviors of the granular system (Fig. 41). Due to the limited deformation of the particles (see Ref. [79]), only elastic properties (i.e., Young's modulus E, Poisson's ratio ν, and density ρ) are considered, and the material is brass in both launching and receiving parts ($E_b = 103$ GPa, $\nu_b = 0.34$ and $\rho_b = 8500$ kg/m^3). A brass sphere ($2R_i = 19.05$ mm) with an initial velocity of 0.1 m/s is applied to impact the

remaining cylindrical granular chain for generating an impulse. All the cylindrical particles have the same height and outer diameter of $H_c = 2R_c = 19.05$ mm. A rigid wall is fixed at the end of the cylindrical granular chain, and a cubic tube is used to restrict the lateral movements of particles.

A surface-to-surface hard contact with frictionless property in the tangential direction is adopted to accurately describe the contact behaviors between adjacent particles, and there are 155 contact pairs in total. Besides, a 10-node modified quadratic tetrahedron (C3D10M) element type is applied to the spherical impactor and cylindrical particles, while a 4-node 3-D bilinear rigid quadrilateral (R3D4) is used to simulate the rigid wall and the cubic tube. Mesh convergence is also ensured to achieve optimal mesh size and reasonable computational costs, and consequently, a mesh size of 1 mm is selected for the cylindrical particle. A gradient-varying mesh size of 0.3-1.5 mm is set for the spherical impactor (see the enlarged view of particles in Fig. 41). The total numbers of elements and nodes are 1,325,232 and 1,879,984, respectively.

5.1.4 Experimental setups

1D cylindrical granular chains were assembled in a vertical guide composed of a series of 3D-printed enclosures (Fig. 42), where lateral movements of particles were restricted. To minimize the experimental friction, the combination of circle and square holes is designed (see the top view of the enclosure in Fig. 42(a)), which greatly reduces the contact

area between particles and enclosures (highlighted area in Fig. 42(a)).

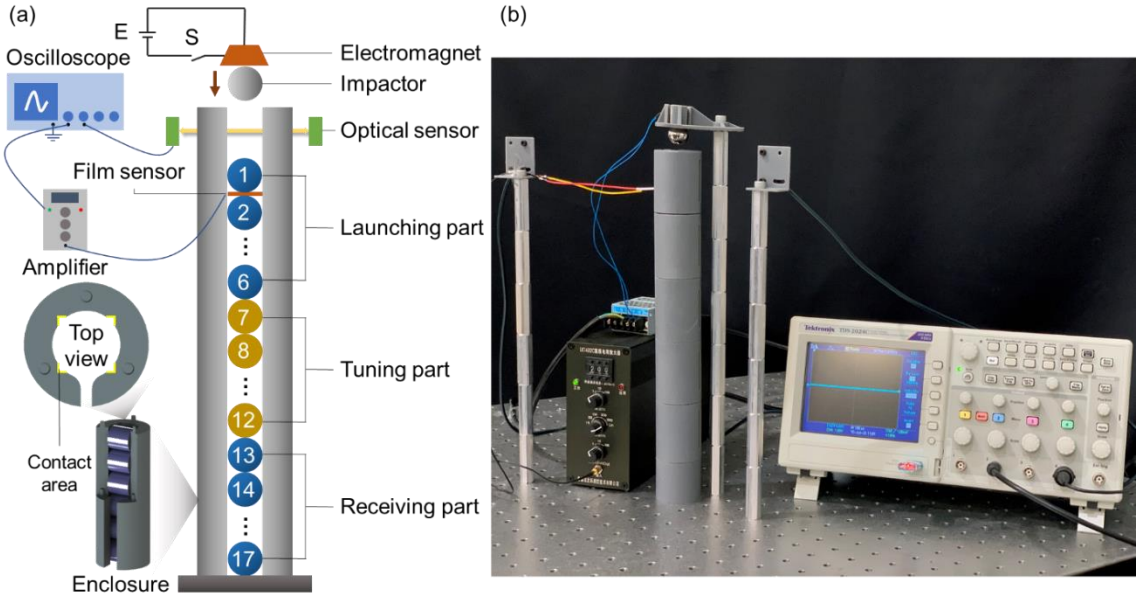

Figure 42 (a) Schematic and (b) actual **e**xperimental setups. 3D-printed enclosures (Formlabs, Form 2) were assembled to serve as a guide for the cylindrical granular chain, and the guide was fixed to an optical table with vibration isolation. The contact area between particles and enclosures is highlighted in the top view of the enclosure. An electromagnet was fixed to a 3D-printed holder for releasing the impactor, and an optical sensor served as an external trigger, ensuring that each test had an identical initial condition. A film sensor was inserted into two different positions in launching part and receiving part (i.e., between 1st and 2nd particles, 13th, and 14th particles), respectively. The effect of thickness and mass of the film sensor can be neglected compared to particles in the granular chain [79].

Five different configurations (Table 9) were delicately designed to demonstrate the concept of the proposed solitary wave tuning strategies. All the particles possess dimensions consistent with the FE model. Since coupling strategies commonly appear in practical applications, different wave tuning strategies were considered simultaneously instead of a single wave tuning strategy. The coupling effect of different strategies will be

systematically discussed in Section 5.3.1.

Table 9 Configurations of 1D cylindrical granular chains in experiments

Configuration		Particle	Number	Material	$m_{1,3}$ / m_2	$E_{1,3}$ / E_2	$t_{1,3}$ / t_2
	Launching	Solid	6	Stainless-steel			
1	Tuning	Solid	6	Aluminum	2.87	2.90	1.00
	Receiving	Solid	5	Stainless-steel			
	Launching	Solid	6	Stainless-steel			
2	Tuning	Solid	6	Nylon	7.17	56.34	1.00
	Receiving	Solid	5	Stainless-steel			
	Launching	Hollow	6	Stainless-steel			
3	Tuning	Hollow	6	Aluminum	2.88	2.90	0.96
	Receiving	Hollow	5	Stainless-steel			
	Launching	Hollow	6	Stainless-steel			
4	Tuning	Hollow	6	Aluminum	5.11	2.90	1.85
	Receiving	Hollow	5	Stainless-steel			
	Launching	Hollow	6	Stainless-steel			
5	Tuning	Hollow	6	Aluminum	6.57	2.90	2.45
	Receiving	Hollow	5	Stainless-steel			

A stainless-steel sphere controlled by an electromagnet was released from a specific height, resulting in an initial velocity of 0.53 m/s when impacting the granular chain. A film sensor was used to detect and capture the waveforms as stress waves propagate. The signals were processed by an amplifier (LK1432C) and then exported to a four-channel oscilloscope (Tektronix, TDS-2024C). Connected to the oscilloscope, an optical sensor (OMRON, E3Z) was aligned oppositely, which could provide external input to the oscilloscope. Since the optical sensor was triggered by the release of the impactor under a specific loading scenario, the time difference could be obtained from different locations of the film sensor, enabling a precise capture of propagating stress waves in the granular chain.

More details about the film sensor and the capture of waveforms in the experiment are available in [13, 79].

5.1.5 Validation

Even if the enclosure is carefully designed, there exist unavoidable friction effects in experiments, and it is difficult to measure the accurate frictional coefficient. Thus, a mild frictional effect (penalty type) is applied to the interaction properties in FE models to mimic the small frictions between the guide and particles in experiments. The comparison of contact forces from experiments and simulations agrees well with each other in Fig. 43.

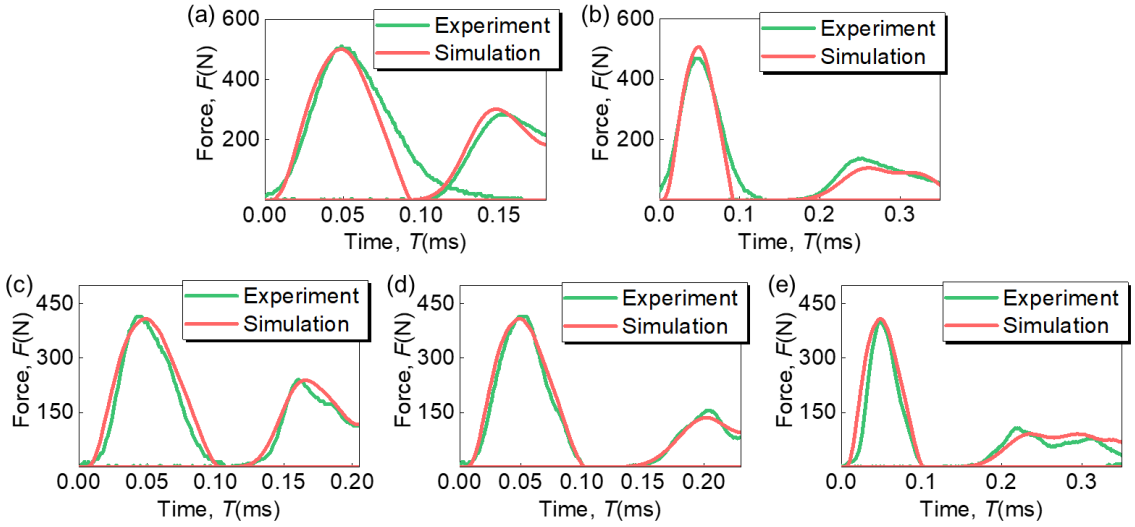

Figure 43 Validation of the FE model by comparing the contact force profiles from experiments and simulations. The frictional effect in experiments is included by introducing a mild frictional coefficient (f) in interaction properties. (a) Configuration 1: $f = 0.05$; (b) Configuration 2: $f = 0.01$; (c) Configurations 3: $f = 0.02$; (d) Configuration 4: $f = 0.02$; (e) Configuration 5: $f = 0.02$.

Furthermore, the values of α_c are calculated in Table 10 to demonstrate the performances of solitary wave attenuation corresponding to different solitary wave tuning

strategies. The attenuation effect improves with higher mass, modulus, and thickness mismatch ratios. Also, both the experimental and numerical results reveal that it is possible to quantitatively tune α_c by precisely selecting appropriate mismatch ratios, which may fundamentally change the traditional way of designing attenuation systems.

Table 10 Compression ratios obtained from different configurations

Configuration	1	2	3	4	5
Experiment	0.56	0.29	0.58	0.38	0.27
Simulation	0.60	0.21	0.59	0.33	0.22

5.2 Results

5.2.1 Mass mismatch

Given the contact forces in a representative mass mismatch case (Fig. 44(a)), solitary waves are observed in both the launching and receiving parts, while the tuning part exhibits expanded waveforms and oscillating tails. A notable decrease in the contact force is also observed in the receiving part, demonstrating the attenuation of solitary waves in mass mismatch systems. Also, a series of mass ratios are adopted to uncover the tuning limit of the mass mismatch, and the values of α_c are evaluated accordingly (Fig. 44(b)). It appears that α_c drops dramatically with an increasing mass ratio at the beginning then turns into a slight decline. As the mass ratio further increases, the tuning part will suffer a longer excitation from the last particle in the launching part. According to Ref. [1, 79], the duration of impulses is closely related to the impactor-to-particle mass ratio and a longer duration (or a larger mass ratio) leads to wider leading waveforms, which will interact with stress

waves in the receiving part and finally a saturated compression ratio is achieved (~0.68).

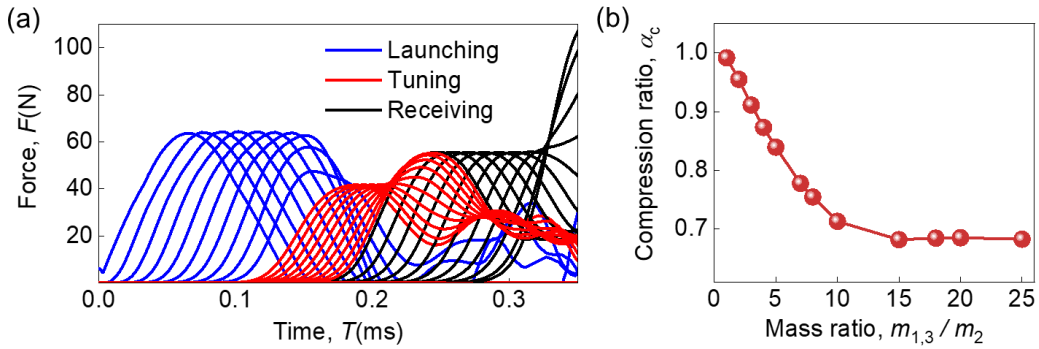

Figure 44 Typical results of the mass mismatch strategy. (a) The evolution of contact forces from different particles as stress waves propagate ($m_{1,3}$ / m_2 = 4); (b) Compression ratios under various mass ratios.

5.2.2 Modulus mismatch

Considering that Young's modulus ratio of available natural or engineering materials can be up to 10^5 [110], the modulus mismatch strategy might be notably feasible and vital in engineering applications. Compared to the mass mismatch case (Fig. 44(a)), the evolution of the waveforms in cases with a modulus mismatch (Fig. 45(a)) is slightly different even if solitary wave attenuation is achieved in both strategies. For the modulus mismatch strategy, no clear expansion is found in the tuning part and there exist regularly oscillating tails as the stress wave propagates. Besides, stress waves in the receiving part behave more like perfectly compressive solitary waves with no wave tail. Also, since there is no expanded leading waveform at a high modulus mismatch ratio, the wave tuning domain in cases with a modulus mismatch is much wider compared to those with a mass mismatch and can reach a limit of 0.28 when the modulus ratio is around 90 (Fig. 45(b)).

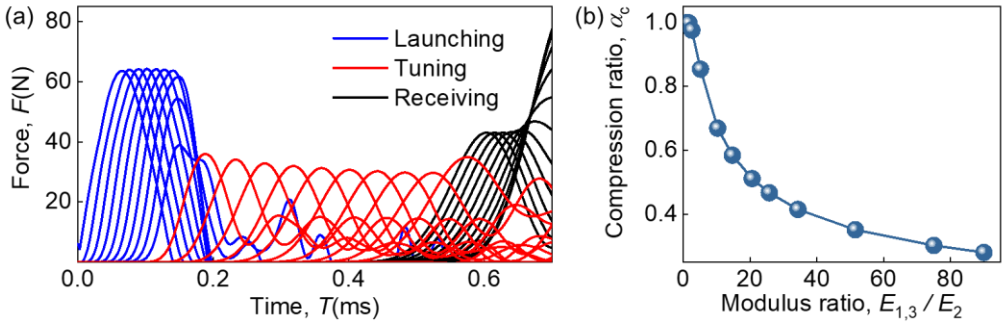

Figure 45 (a) Typical results of the modulus mismatch strategy ($E_{1,3}$ / E_2 = 10); (b) Compression ratios under various modulus ratios.

5.2.3 Thickness mismatch

Herein, an outstanding attenuation effect is achieved with a typical thickness mismatch (Fig. 46(a)), and the corresponding α_c is 0.64. By comparison with wave behaviors from the mass and modulus mismatch strategies, the waveforms of the tuning part in thickness mismatch configurations (where thinner hollow particles are arranged) reveal rarefaction-like performance. Furthermore, certain wave tails are also observed in the tuning part, which does not greatly affect the shapes of stress waves propagating in the receiving part.

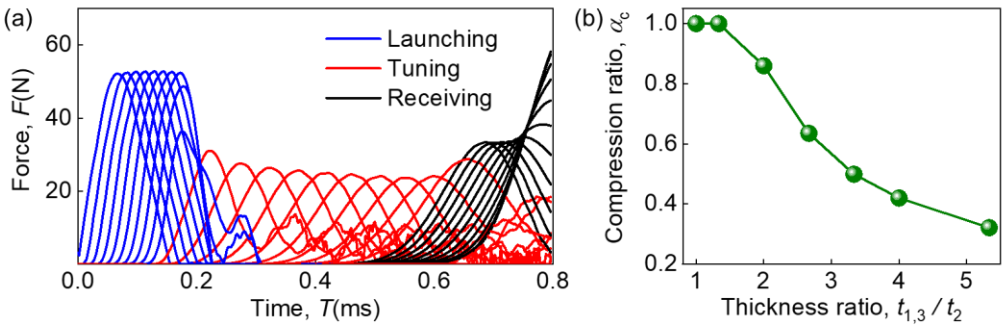

Figure 46 (a) Typical results of the thickness mismatch strategy ($t_{1,3}$ / t_2 = 2.67); (b) Compression ratios under various thickness ratios.

By varying the thickness ratio from 1.00 to 5.33 (Fig. 46(b)), an interesting phenomenon is discovered that the attenuation effect is quite sensitive to the thickness ratio. Since 1D hollow cylindrical chains can support both compressive solitons and rarefaction mitigating waves by varying the thickness of particles [79], a higher thickness ratio along with rarefaction mitigation effects will result in a lower compression ratio. Also, the effective contact stiffness may decrease with the thickness of particles in the tuning part, which will further lower the amplitude of contact forces. However, if the thickness ratio is ultra-high (i.e., when hollow cylinders are evolved into thin-walled structures), the problem may be converted to the study of traditional ring systems with energy dissipated by plastic deformation, which is beyond the scope of the present study.

5.3 Discussion

5.3.1 Coupling strategy

Since all the proposed strategies are demonstrated to be effective and highly efficient for solitary wave attenuation, it is natural to investigate the coupling effect of different strategies and expect to achieve superior performance of solitary wave attenuation. Two different configuration types are designed and simulated to comprehensively understand the coupling effect and influencing mechanisms of wave tuning strategies. In Type I configuration, cylindrical granular chains are investigated by coupling two out of three proposed strategies. In Type II configuration, all the proposed strategies are coupled

together to implement a more systematic and broader solitary wave tuning strategy.

In Type I configuration (Fig. 47), the ranges of mass, modulus, and thickness ratios are set to 1 to 15, 1 to 30, and 1 to 2, respectively. For each coupling strategy, an inversely proportional-like relation is observed between the two mismatch ratios. However, under higher mismatch ratios, the varying law tends to be different, and the tuning regions are greatly expanded. An interesting observation is that with a modulus ratio of $E_{1,3} / E_2 = 25$, the tuning limit of α_c would appear at a mass ratio $m_{1,3} / m_2 > 15$, yet $m_{1,3} / m_2 = 15$ is where the tuning limit occurs within a single mass mismatch (Fig. 44(b)). Similar results are also found in the mass-thickness mismatch (Fig. 47(b)) and the modulus-thickness mismatch (Fig. 47(c)). This may result from the fact that the properties of traveling stress waves at the "strong-weak" and "weak-strong" interfaces are different in various strategies. For example, Ref. [61] clarified that the modulus mismatch would introduce a reflected wave at the "strong-weak" interface compared to that in single mass mismatch cases. Given the investigated range of mismatch ratios, the modulus ratio plays a dominant role, while mass and thickness ratios contribute similarly to Type I configuration. Moreover, the values of α_c are much smaller than those in Section 5.2 with a single tuning strategy, indicating that the attenuation effect is further enhanced in all the coupling strategies. Corresponding to different combinations of mismatch ratios, a broad range of α_c from 0.1 to 1.0 together with the presented full-scale compression ratio maps, are achieved, enabling us to design

quantitatively solitary wave tuning systems for attenuation.

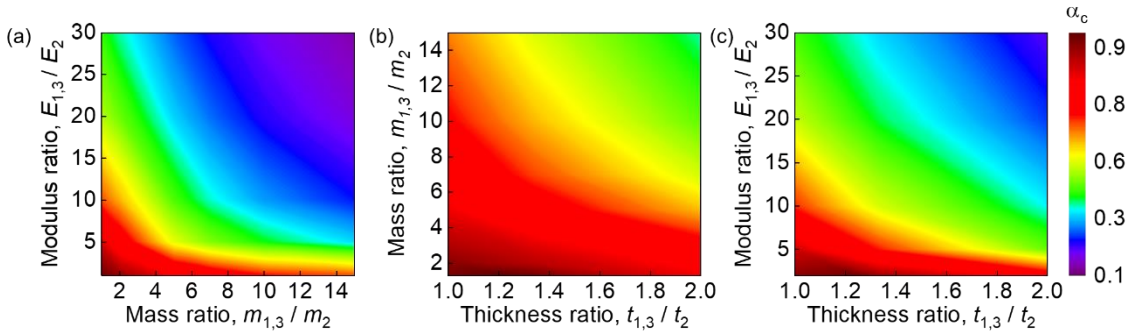

Figure 47 Maps of compression ratios obtained from Type I coupling strategies. (a) Mass-modulus mismatch, (b) mass-thickness mismatch, (c) modulus-thickness mismatch.

In Type II configuration (Fig. 48(a)), the traveling wave decomposes into several oscillating tails at the interface between the tuning and receiving parts, where the main wave and tails are marked as the 1st and 2nd traveling waves, separately. Also, two reflected waves are formed at this interface and the rigid wall. The wave speeds of solitary waves in the launching and receiving parts are 1245.2 m/s and 1322.8 m/s, respectively. A small discrepancy (~5.8%) of the wave speeds may be due to the receiving part being close to the fixed rigid wall. Herein, the impact velocity for the launching part is from the impactor, while for the receiving part, it comes from the last particle in the tuning part. These two impact velocities are different, yet identical wave speed is obtained. The consistency of wave speeds originates from the unique wave dynamics of the 1D cylindrical granular chain, where the wave speed of traveling waves is independent of the impact velocity. This remarkable result indicates that the proposed 1D granular chains can achieve solitary wave

attenuation without changing the wave speed of original impulses, which is highly significant for engineering applications. Namely, instead of the original solitary waves with a high amplitude, the new solitary waves with smaller amplitudes can deliver critical information without any loss.

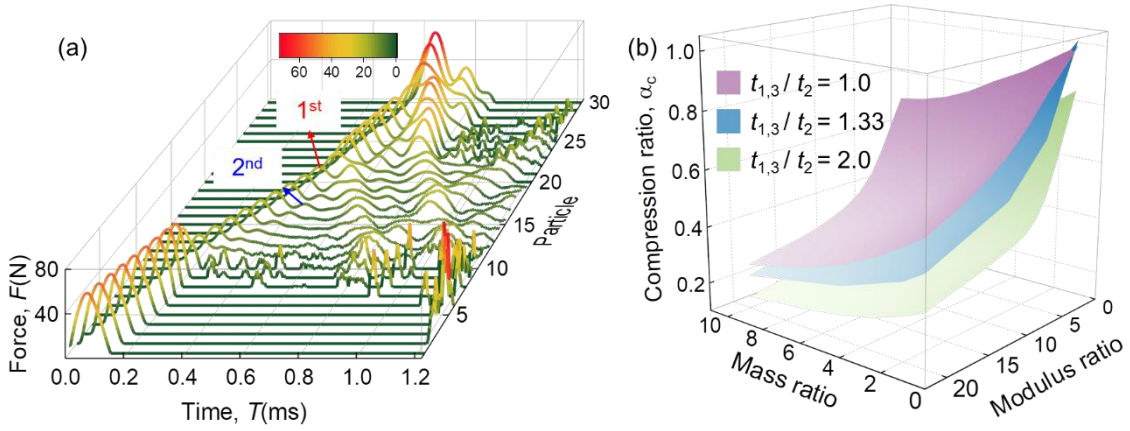

Figure 48 (a) Typical results of Type II coupling strategy ($m_{1,3}$ / m_2 = 2, $E_{1,3}$ / E_2 = 5, $t_{1,3}$ / t_2 = 1.33); (b) Compression ratio maps corresponding to different mass, modulus, and thickness ratios.

Furthermore, two vital results can be obtained by varying the mismatch ratios (Fig. 48(b)). Firstly, the attenuation effect can be further enhanced compared to that of single wave tuning strategies or Type I configuration. For instance, under a configuration with $m_{1,3}$ / m_2 = 10, $E_{1,3}$ / E_2 = 20, $t_{1,3}$ / t_2 = 2, the compression ratio is as low as 0.14 and this value can be lowered by further increasing the mismatch ratios. Ideally, a stress wave switch can be implemented by appropriately selecting the mismatch ratios. In addition, the most violent varying trend of α_c is found in the modulus plane, and it indicates that the modulus ratio is the leading factor among all three influencing ratios, which is consistent

with the observation in Fig. 48(a).

5.3.2 Multilayer granular chain

Herein, a two-layer granular chain is developed and systematically analyzed (Fig. 49(a)). Specifically, it is composed of five parts with ten cylindrical particles in each part, where Part 2 and Part 4 serve as the tuning parts, Part 1 and Part 5 are the launching part and the receiving part, respectively. Referring to the definition of the single-layer solitary wave tuning granular chain, Part 1, Part 2, and Part 3 constitute layer 1 (L_1) while Part 3, Part 4, and Part 5 form layer 2 (L_2).

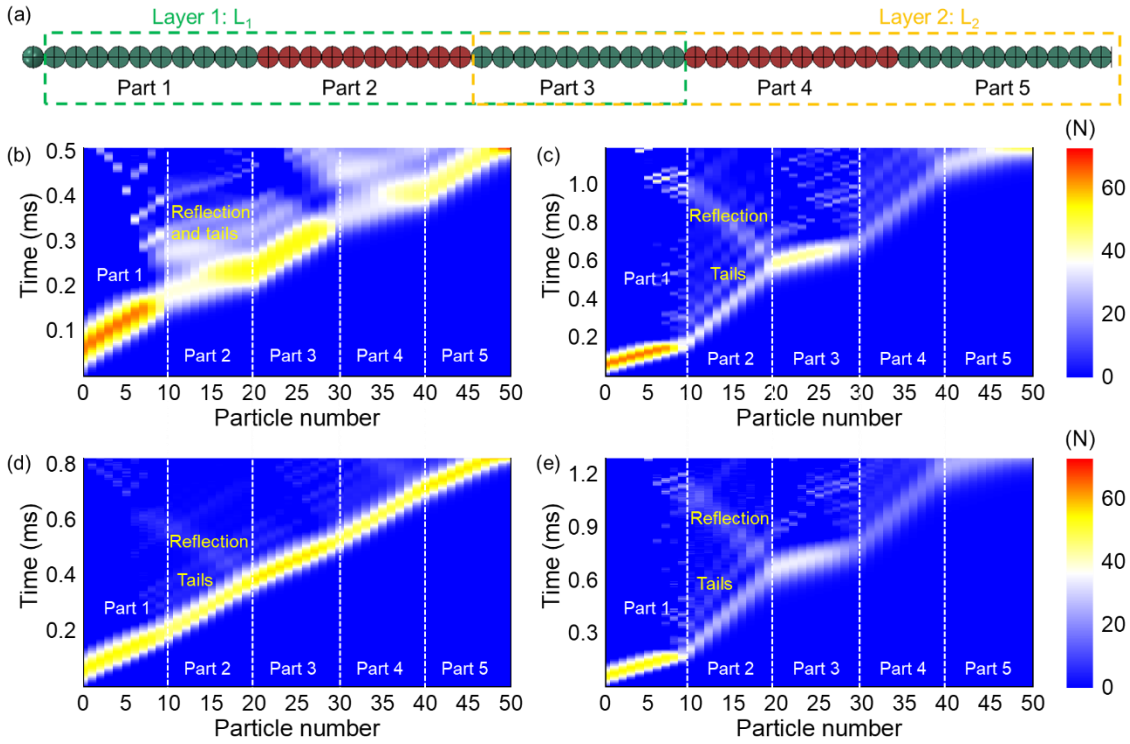

Figure 49 (a) Configuration of the two-layer granular chain. Typical results of two-layer granular chains with (b) mass mismatch ($m_{1,3,5}$ / $m_{2,4}$ = 5), (c) modulus mismatch ($E_{1,3,5}$ / $E_{2,4}$ = 10), and thickness mismatch (d) $t_{1,3,5}$ / $t_{2,4}$ = 1.33, (e) $t_{1,3,5}$ / $t_{2,4}$ = 2.67.

Interestingly, phased solitary wave attenuation behavior is observed in two-layer granular chains with single mismatch strategies (Figs. 49(b)-(e)). The propagating stress waves in each layer behave similarly to those in a single layer wave tuning chain discussed in Section 5.2. The reflection is found at interfaces where stress waves propagate from the tuning part to the receiving part, and oscillating tails (or decomposition) appear at interfaces from the launching part to the tuning part; however, the distribution and intensity of them are notably distinct among different configurations.

In a mass mismatch configuration (Fig. 49(b)), the reflection and decomposition of stress waves are overlapping and interacting with each other, leading to a broad distribution of waveforms in tuning parts. Additionally, there's an increase in the contact forces of the last few particles within tuning parts due to the interfacial effects. Nevertheless, these features are slightly distinct in the cases with a modulus or thickness mismatch (Figs. 49(c)-(e)), where no clear overlap is observed. Thus, the output stress waves are significantly dependent on both the material and geometric properties of particles in the tuning parts. Moreover, the propagating stress waves in the case with a low thickness ratio (Fig. 49(d)) perform solitary-like behaviors throughout the granular chain, whereas apparent rarefaction waves with expanded waveforms are obtained in tuning parts of cases with a higher thickness ratio (Fig. 49(e)).

For further investigation on the phased solitary wave attenuation, the compression

ratio is evaluated for each layer (i.e., $\alpha_{c1} = F_3 / F_1$ and $\alpha_{c2} = F_5 / F_3$ for L_1 and L_2 in Fig. 50, respectively) and the total compression ratio of the whole granular chain ($\alpha_c = F_5 / F_1$) is calculated as well. Indeed, α_{c1} and α_{c2} are almost the same in the two-layer granular chains with various mass ratios (Fig. 50(a)), while this is not the case for the modulus or thickness mismatch (Figs. 50(b)-(c)). α_{c2} is close to α_{c1} when the modulus or thickness ratio is relatively low (e.g., $E_{1,3,5} / E_{2,4} < 10$ and $t_{1,3,5} / t_{2,4} < 2$), and α_{c2} is higher than α_{c1} under higher modulus or thickness ratios, indicating a lowered attenuation effect in L_2 compared to that of L_1 within a two-layer granular chain. Consequently, the mass mismatch strategy will be more sensitive to the changing of α_c than α_{c1} and α_{c2}.

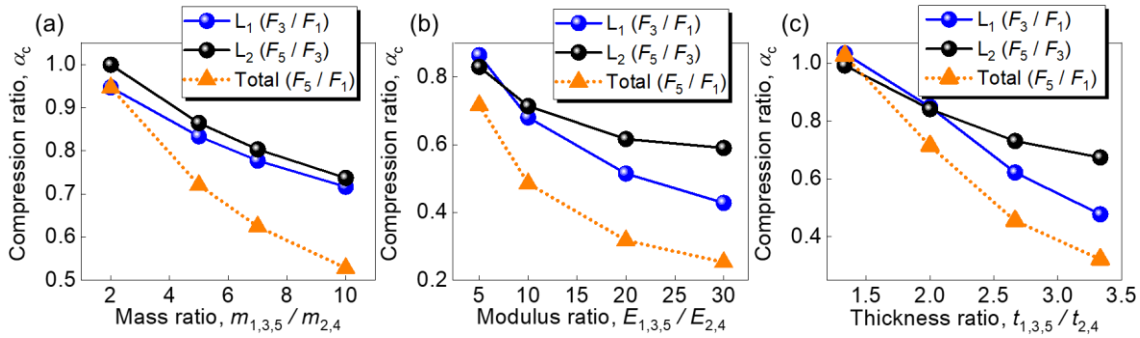

Figure 50 Compression ratios of two-layer granular chains with (a) mass mismatch, (b) modulus mismatch, and (c) thickness mismatch.

This interesting phenomenon is closely related to the behaviors of the stress waves propagating in different configurations. By comparing the contact forces maps in cases with different thickness ratios (Figs. 49(d)-(e)), a longer-lasting or more intense distribution of the oscillating tails in tuning parts may have subsequent influences on the

receiving parts, for instance, the oscillating tails of Part 2 in Fig. 49(e) propagate and enter Part 3, which will, in turn, affect the following parts. The accumulating effect might be more obvious in multilayer granular chains. Nevertheless, all the two-layer granular chains have undeniably achieved a superior attenuation effect regardless of the low efficiency of attenuation in L_2 for modulus or thickness mismatch configurations. Since all the tuning parts share identical properties in current configurations, the tuning range can be further expanded and customized by designing composite multilayer granular chains with different properties set to the tuning parts.

The efficiency of the phased attenuation effect can also be improved in coupling strategies. In mass-modulus and mass-thickness strategies (Figs. 51(a)-(b)), the compression ratios of different layers are consistent under various modulus or thickness ratios. However, the difference in compression ratios between different layers is more distinct in the modulus-thickness strategy (Fig. 51(c)). Note that the total compression ratios of these coupling strategies are as low as 0.09, 0.14, and 0.23, respectively.

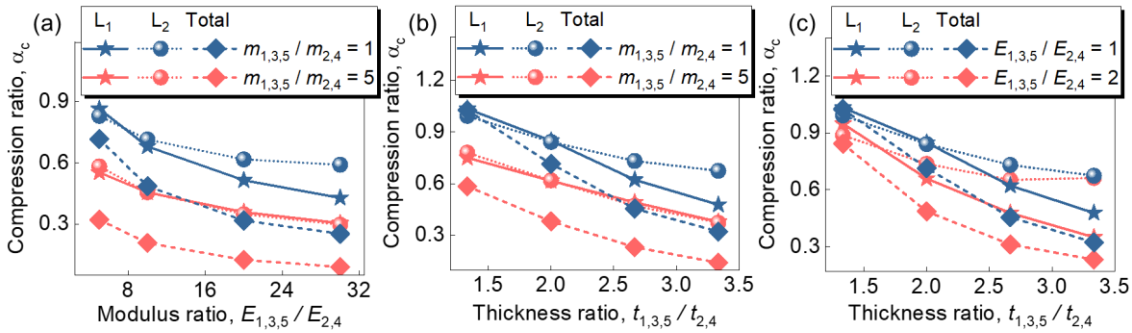

Figure 51 Compression ratios of two-layer granular chains with Type I coupling strategies. (a) Mass-modulus, (b) mass-thickness, (c) modulus-thickness.

5.3.3 Mechanism map

Quantitatively wave tuning strategies are accessible based on a normalized Ashby plot (Fig. 52) [110]. Herein, brass (E_b, m_b) is considered to achieve normalized axes in a conventional Ashby plot (modulus versus density). Consistent with the configurations in previous sections, brass also serves as the material for both launching and receiving parts in designing the solitary wave attenuation systems. For possible engineering applications, one may find the corresponding α_c on contour lines in the map, which cross through a variety of blocks and, in turn, provide candidates for the material selection in the tuning part.

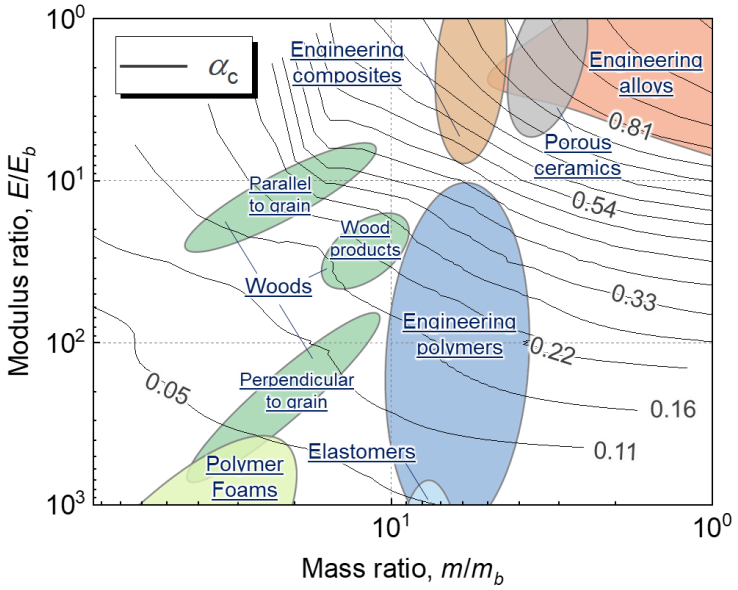

Figure 52 Informative map of materials for the tuning part corresponding to specific compression ratios.

For instance, a solitary wave attenuation system with α_c of approximately 0.81 can

be established by choosing cylindrical particles made from specific engineering alloys, engineering composites, or porous ceramics. Therefore, the presented results allow us to achieve quantitatively wave tuning and provide valuable insights into designing new attenuation systems.

5.4 Conclusions

In this chapter, 1D cylindrical granular chains were designed and constructed to demonstrate various solitary wave tuning strategies for attenuation through both experimental and numerical approaches. The mismatch of mass, modulus, or thickness in different parts of granular chains led to an apparent decrease in the contact force amplitudes, which makes the proposed systems capable of solitary wave attenuation. This solitary wave attenuation ability was further enhanced by coupling different wave tuning strategies and building multilayer granular chains, where the phased solitary wave attenuation was observed in multilayer granular chains. The presented results provide a simple way for quantitatively tailoring the dynamic responses of propagating waves and the attenuation effect in the granular chains. Finally, a mechanism map was proposed to offer the basis to design solitary wave attenuation systems to satisfy specific engineering applications. Results unlock the underlying mechanism of the solitary wave attenuation and provide design guidelines for next-generation stress wave detection, attenuation, and monitoring system.

CHAPTER 6 CONCLUDING REMARKS

In this dissertation work, stress wave propagation and tuning strategies in various 1D granular systems were systematically investigated. Firstly, 1D composite cylindrical granular chains were proposed by applying different materials in core-shell and sandwich-type particles. The formation of strongly nonlinear solitary waves was experimentally, numerically, and analytically demonstrated, where a shell-dominated behavior was obtained by varying the geometric parameters of composite particles. The featured relationship between wave properties and critical parameters (i.e., the effective modulus and total mass) was revealed and then extended to more generalized granular systems. Next, two types of equivalent systems were developed in 1D spherical granular, including generalized and restricted systems, where an equivalent transmission was achieved in 1D granular systems composed of spherical particles with different sizes and materials. Also, an informative mechanism map was given as guidance for designing 1D granular systems to meet specific requirements in engineering applications. Following that, two effective stress attenuation approaches were proposed by engineering a 1D HC granular chain with strain-softening behaviors and a 1D kirigami lantern chain. Particularly, the 1D HC granular chains were proved to support both solitary waves and mitigating waves by simply varying the thickness ratio of HC particles, where an optimized mitigating efficiency can be obtained in a rather short chain. In 1D kirigami lantern chains, an outstanding impact

mitigation performance (orders of magnitude lower transmission in contrast to previous designs) was achieved with lightweight materials, and the underlying mechanism lay in the unique folding-unfolding behaviors of kirigami cells during stress wave propagation. Finally, a series of quantitative wave tuning strategies was presented based on the mass/modulus/thickness mismatch in 1D cylindrical granular chains, where an enhanced wave attenuation effect can be achieved by coupling different wave tuning strategies and developing multilayered granular chains.

Results of this dissertation work offer a comprehensive understanding of the wave dynamics in 1D granular systems and unlock the fundamental mechanisms between wave properties and system characteristics. Also, simple configurations to quantitatively tune the wave behaviors and stress wave attenuation were realized, providing guidelines for designing next-generation impact protection systems, wave detection, and monitoring systems.

REFERENCES

[1] V. Nesterenko, Dynamics of heterogeneous materials, Springer Science & Business Media, 2013.

[2] V. Nesterenko, Solitary waves in discrete medium with anomalous compressibility, Fizika gorenia i vzryva, 29 (1993) 134-136.

[3] S. Sen, M. Manciu, Solitary wave dynamics in generalized Hertz chains: An improved solution of the equation of motion, Physical Review E, 64 (2001) 056605.

[4] S. Job, F. Melo, A. Sokolow, S. Sen, Solitary wave trains in granular chains: experiments, theory and simulations, Granular Matter, 10 (2007) 13-20.

[5] C. Chong, P.G. Kevrekidis, Coherent Structures in Granular Crystals: From Experiment and Modelling to Computation and Mathematical Analysis, Springer, 2018.

[6] M.A. Porter, P.G. Kevrekidis, C. Daraio, Granular crystals: Nonlinear dynamics meets materials engineering, Phys. Today, 68 (2015).

[7] A. Lazaridi, V. Nesterenko, Observation of a new type of solitary waves in a one-dimensional granular medium, Journal of Applied Mechanics and Technical Physics, 26 (1985) 405-408.

[8] C. Coste, E. Falcon, S. Fauve, Solitary waves in a chain of beads under Hertz contact, Physical review E, 56 (1997) 6104.

[9] S. Job, F. Melo, A. Sokolow, S. Sen, How Hertzian solitary waves interact with boundaries in a 1D granular medium, Physical review letters, 94 (2005) 178002.

[10] F. Li, L. Yu, J. Yang, Solitary wave-based strain measurements in one-dimensional granular crystals, Journal of Physics D: Applied Physics, 46 (2013) 155106.

[11] E. Herbold, V. Nesterenko, Shock wave structure in a strongly nonlinear lattice with viscous dissipation, Physical Review E, 75 (2007) 021304.

[12] A. Molinari, C. Daraio, Stationary shocks in periodic highly nonlinear granular chains, Physical Review E, 80 (2009) 056602.

[13] W. Zhang, J. Xu, Universal design law of equivalent systems for Nesterenko solitary waves transmission, Granular Matter, 22 (2020) 1-12.

[14] C. Daraio, V. Nesterenko, E. Herbold, S. Jin, Strongly nonlinear waves in a chain of Teflon beads, Physical Review E, 72 (2005) 016603.

[15] M.A. Porter, C. Daraio, E.B. Herbold, I. Szelengowicz, P. Kevrekidis, Highly nonlinear solitary waves in periodic dimer granular chains, Physical Review E, 77 (2008) 015601.

[16] D. Ngo, D. Khatri, C. Daraio, Highly nonlinear solitary waves in chains of ellipsoidal particles, Physical Review E, 84 (2011) 026610.

[17] D. Ngo, S. Griffiths, D. Khatri, C. Daraio, Highly nonlinear solitary waves in chains of hollow spherical particles, Granular Matter, 15 (2013) 149-155.

[18] H. Kim, E. Kim, C. Chong, P. Kevrekidis, J. Yang, Demonstration of dispersive rarefaction shocks in hollow elliptical cylinder chains, Physical review letters, 120 (2018) 194101.
[19] V. Nesterenko, Propagation of nonlinear compression pulses in granular media, J. Appl. Mech. Tech. Phys.(Engl. Transl.);(United States), 24 (1984).
[20] C. Daraio, V. Nesterenko, E. Herbold, S. Jin, Tunability of solitary wave properties in one-dimensional strongly nonlinear phononic crystals, Physical Review E, 73 (2006) 026610.
[21] W. Zhang, J. Xu, Quantitatively solitary wave tuning strategies based on one-dimensional cylindrical granular chains, Extreme Mechanics Letters, 40 (2020) 100972.
[22] T. On, P.A. LaVigne, J. Lambros, Development of plastic nonlinear waves in one-dimensional ductile granular chains under impact loading, Mechanics of Materials, 68 (2014) 29-37.
[23] E. Kim, J. Yang, H. Hwang, C.W. Shul, Impact and blast mitigation using locally resonant woodpile metamaterials, International journal of impact engineering, 101 (2017) 24-31.
[24] K.T. Tan, H. Huang, C. Sun, Blast-wave impact mitigation using negative effective mass density concept of elastic metamaterials, International Journal of Impact Engineering, 64 (2014) 20-29.
[25] F. Li, D. Ngo, J. Yang, C. Daraio, Tunable phononic crystals based on cylindrical Hertzian contact, Appl. Phys. Lett., 101 (2012) 171903.
[26] N. Boechler, G. Theocharis, C. Daraio, Bifurcation-based acoustic switching and rectification, Nature materials, 10 (2011) 665-668.
[27] F. Li, P. Anzel, J. Yang, P.G. Kevrekidis, C. Daraio, Granular acoustic switches and logic elements, Nature communications, 5 (2014) 1-6.
[28] J. Hong, A. Xu, Nondestructive identification of impurities in granular medium, Appl. Phys. Lett., 81 (2002) 4868-4870.
[29] X. Ni, P. Rizzo, J. Yang, D. Katri, C. Daraio, Monitoring the hydration of cement using highly nonlinear solitary waves, NDT & E International, 52 (2012) 76-85.
[30] R. Misra, H. Jalali Najafabadi, S. Dickerson, P. Rizzo, Wireless Module for Nondestructive Testing/Structural Health Monitoring Applications Based on Solitary Waves, Sensors, 20 (2020) 3016.
[31] G. Gantzounis, M. Serra-Garcia, K. Homma, J. Mendoza, C. Daraio, Granular metamaterials for vibration mitigation, J. Appl. Phys., 114 (2013) 093514.
[32] E. Kim, J. Yang, Wave propagation in single column woodpile phononic crystals: Formation of tunable band gaps, J. Mech. Phys. Solids, 71 (2014) 33-45.
[33] V. Nesterenko, C. Daraio, E. Herbold, S. Jin, Anomalous wave reflection at the

interface of two strongly nonlinear granular media, Physical review letters, 95 (2005) 158702.
[34] V. Nesterenko, Nonlinear waves in “sonic vacuum”, Fizika gorenia i vzryva, 28 (1992) 121.
[35] V. Nesterenko, High-rate deformation of heterogeneous materials, in, Nauka, Novosibirsk, 1992.
[36] J.S. Russell, Report of the Committee on Waves, in: Report of the 7th Meeting of the British Association for the Advancement of Science, Liverpool, John Murray London, 1838.
[37] J.W. Miles, Solitary waves, Annual review of fluid mechanics, 12 (1980) 11-43.
[38] K.L. Johnson, Contact mechanics, Cambridge university press, 1987.
[39] C. Chong, M.A. Porter, P.G. Kevrekidis, C. Daraio, Nonlinear coherent structures in granular crystals, Journal of Physics: Condensed Matter, 29 (2017) 413003.
[40] G. Friesecke, J.A. Wattis, Existence theorem for solitary waves on lattices, Commun. Math. Phys., 161 (1994) 391-418.
[41] J.-Y. Ji, J. Hong, Existence criterion of solitary waves in a chain of grains, Phys. Lett. A, 260 (1999) 60-61.
[42] D. Khatri, D. Ngo, C. Daraio, Highly nonlinear solitary waves in chains of cylindrical particles, Granular Matter, 14 (2012) 63-69.
[43] R. Chaunsali, E. Kim, A. Thakkar, P.G. Kevrekidis, J. Yang, Demonstrating an in situ topological band transition in cylindrical granular chains, Physical review letters, 119 (2017) 024301.
[44] A. Palmgren, Ball and roller bearing engineering, Burbank, Philadelphia, (1959).
[45] A. Chatterjee, Asymptotic solution for solitary waves in a chain of elastic spheres, Physical Review E, 59 (1999) 5912.
[46] V. Nesterenko, Pulse compression nature in a strongly nonlinear grained medium, in: Proc. of the Int. Symp. on Intense Dynamic Loading and its Effects, 1992, pp. 236-239.
[47] V. Nesterenko, A new type of collective excitations in a" sonic vacuum, Akustika neodnorodnykh sred, Novosibirsk, (1992) 228-233.
[48] M.H. Sadd, Q. Tai, A. Shukla, Contact law effects on wave propagation in particulate materials using distinct element modeling, International journal of non-linear mechanics, 28 (1993) 251-265.
[49] V. Nesterenko, Solitary waves in discrete media with anomalous compressibility and similar to" sonic vacuum", Le Journal de Physique IV, 4 (1994) C8-729-C728-734.
[50] W. Zhang, J. Xu, Tunable traveling wave properties in one-dimensional chains composed from hollow cylinders: from compression to rarefaction waves, International Journal of Mechanical Sciences, (2020) 106073.

[51] M. Manciu, S. Sen, A.J. Hurd, The propagation and backscattering of soliton-like pulses in a chain of quartz beads and related problems.(I). Propagation, Physica A: Statistical Mechanics and its Applications, 274 (1999) 588-606.
[52] M. Manciu, S. Sen, A.J. Hurd, The propagation and backscattering of soliton-like pulses in a chain of quartz beads and related problems.(II). Backscattering, Physica A: Statistical Mechanics and its Applications, 274 (1999) 607-618.
[53] A. Shukla, M. Sadd, Y. Xu, Q. Tai, Influence of loading pulse duration on dynamic load transfer in a simulated granular medium, Journal of the Mechanics Physics of Solids, 41 (1993) 1795-1808.
[54] F. Santibanez, R. Munoz, A. Caussarieu, S. Job, F. Melo, Experimental evidence of solitary wave interaction in Hertzian chains, Physical Review E, 84 (2011) 026604.
[55] S. Sen, J. Hong, J. Bang, E. Avalos, R. Doney, Solitary waves in the granular chain, Physics Reports, 462 (2008) 21-66.
[56] P.G. Kevrekidis, Non-linear waves in lattices: past, present, future, IMA Journal of Applied Mathematics, 76 (2011) 389-423.
[57] A. Rosas, K. Lindenberg, Pulse propagation in granular chains, Physics Reports, 735 (2018) 1-37.
[58] Y. Man, N. Boechler, G. Theocharis, P. Kevrekidis, C. Daraio, Defect modes in one-dimensional granular crystals, Physical Review E, 85 (2012) 037601.
[59] S. Yin, D. Chen, J. Xu, Novel propagation behavior of impact stress wave in one-dimensional hollow spherical structures, International Journal of Impact Engineering, 134 (2019) 103368.
[60] C. Daraio, V. Nesterenko, Strongly nonlinear wave dynamics in a chain of polymer coated beads, Physical Review E, 73 (2006) 026612.
[61] H. Wang, B. Wu, X. Liu, C.-H. Yang, C. He, Influencing factors of the performance of an impact buffering made of the composite granular chain, International Journal of Impact Engineering, 137 (2020) 103463.
[62] N. Boechler, G. Theocharis, S. Job, P. Kevrekidis, M.A. Porter, C. Daraio, Discrete breathers in one-dimensional diatomic granular crystals, Physical review letters, 104 (2010) 244302.
[63] C. Coste, B. Gilles, On the validity of Hertz contact law for granular material acoustics, The European Physical Journal B-Condensed Matter and Complex Systems, 7 (1999) 155-168.
[64] A. Nasrollahi, R. Lucht, P. Rizzo, Solitary waves to assess the internal pressure and the rubber degradation of tennis balls, Experimental Mechanics, 59 (2019) 65-77.
[65] G. Theocharis, M. Kavousanakis, P. Kevrekidis, C. Daraio, M.A. Porter, I. Kevrekidis, Localized breathing modes in granular crystals with defects, Physical Review E, 80 (2009) 066601.

[66] M.A. Porter, C. Daraio, I. Szelengowicz, E.B. Herbold, P. Kevrekidis, Highly nonlinear solitary waves in heterogeneous periodic granular media, Physica D: Nonlinear Phenomena, 238 (2009) 666-676.
[67] W.-H. Lin, C. Daraio, Wave propagation in one-dimensional microscopic granular chains, Physical Review E, 94 (2016) 052907.
[68] Y. Takato, M.E. Benson, S. Sen, The effect of surface geometry on collisions between nanoparticles, arXiv preprint arXiv:.06821, (2016).
[69] Y. Takato, M.E. Benson, S. Sen, Small nanoparticles, surface geometry and contact forces, Proceedings of the Royal Society A: Mathematical, Physical and Engineering Sciences, 474 (2018) 20170723.
[70] J. Xu, B. Zheng, Y. Liu, Solitary wave in one-dimensional buckyball system at nanoscale, Scientific Reports, 6 (2016) 1-6.
[71] B. Zheng, J. Xu, Mechanical wave propagation within nanogold granular crystals, Extreme Mechanics Letters, 15 (2017) 17-25.
[72] J. Xu, B. Zheng, Quantitative tuning nanoscale solitary waves, Carbon, 111 (2017) 62-66.
[73] C. Daraio, V. Nesterenko, E. Herbold, S. Jin, Strongly nonlinear waves in polymer based phononic crystals, in: AIP Conf. Proc., American Institute of Physics, 2006, pp. 1507-1510.
[74] R. Kore, A. Waychal, S. Agarwal, P. Yadav, A. Uddin, N. Sahoo, A. Shelke, Impact induced solitary wave propagation through a woodpile structure, Smart Materials and Structures, 25 (2016) 025027.
[75] R.S. Sinkovits, S. Sen, Nonlinear dynamics in granular columns, Physical review letters, 74 (1995) 2686.
[76] S. Job, F. Santibanez, F. Tapia, F. Melo, Nonlinear waves in dry and wet Hertzian granular chains, Ultrasonics, 48 (2008) 506-514.
[77] C. Chong, E. Kim, E. Charalampidis, H. Kim, F. Li, P. Kevrekidis, J. Lydon, C. Daraio, J. Yang, Nonlinear vibrational-state excitation and piezoelectric energy conversion in harmonically driven granular chains, Physical Review E, 93 (2016) 052203.
[78] J. Yang, M. Gonzalez, E. Kim, C. Agbasi, M. Sutton, Attenuation of solitary waves and localization of breathers in 1D granular crystals visualized via high speed photography, Experimental Mechanics, 54 (2014) 1043-1057.
[79] W. Zhang, J. Xu, Toward understanding solitary wave propagation in composite-cylinders-based 1D granular crystals, Extreme Mechanics Letters, Under review (2020).
[80] A. Schiffer, A. Alkhaja, J. Yang, E. Esfahani, T.-Y. Kim, Interaction of highly nonlinear solitary waves with elastic solids containing a spherical void, International Journal of Solids and Structures, 118 (2017) 204-212.

[81] L. Cai, J. Yang, P. Rizzo, X. Ni, C. Daraio, Propagation of highly nonlinear solitary waves in a curved granular chain, Granular Matter, 15 (2013) 357-366.
[82] A. Nasrollahi, P. Rizzo, Modeling a new dynamic approach to measure intraocular pressure with solitary waves, Journal of the Mechanical Behavior of Biomedical Materials, 103 (2020) 103534.
[83] J. Xu, B. Zheng, Highly effective energy dissipation system based on one-dimensionally arrayed short single-walled carbon nanotubes, Extreme Mechanics Letters, 9 (2016) 336-341.
[84] B. Zheng, J. Xu, Enhanced stress wave attenuation of single-walled carbon nanotube lattice via mass mismatch-induced resonance, Carbon, 116 (2017) 391-397.
[85] K. Li, P. Rizzo, Impurity detection in a chain of spherical particles using time reversal and highly nonlinear solitary waves, J. Appl. Phys., 121 (2017) 145105.
[86] J. Yang, D. Khatri, P. Anzel, C. Daraio, Interaction of highly nonlinear solitary waves with thin plates, International Journal of Solids and Structures, 49 (2012) 1463-1471.
[87] E. Kim, F. Restuccia, J. Yang, C. Daraio, Solitary wave-based delamination detection in composite plates using a combined granular crystal sensor and actuator, Smart Materials and Structures, 24 (2015) 125004.
[88] A. Nasrollahi, P. Rizzo, M.S. Orak, Numerical and Experimental Study on the Dynamic Interaction Between Highly Nonlinear Solitary Waves and Pressurized Balls, Journal of Applied Mechanics, 85 (2018).
[89] E. Kim, F. Li, C. Chong, G. Theocharis, J. Yang, P. Kevrekidis, Highly nonlinear wave propagation in elastic woodpile periodic structures, Physical review letters, 114 (2015) 118002.
[90] R. Carretero-González, D. Khatri, M.A. Porter, P. Kevrekidis, C. Daraio, Dissipative solitary waves in granular crystals, Physical review letters, 102 (2009) 024102.
[91] W.-J. Wang, Z.-G. Zhu, Two kinds of dissipation in sheared granular materials, EPL (Europhysics Letters), 82 (2008) 24004.
[92] W. Morgado, I. Oppenheim, Energy dissipation for quasielastic granular particle collisions, Physical Review E, 55 (1997) 1940.
[93] E. Wang, T. On, J. Lambros, An experimental study of the dynamic elasto-plastic contact behavior of dimer metallic granules, Experimental Mechanics, 53 (2013) 883-892.
[94] R.K. Pal, A.P. Awasthi, P.H. Geubelle, Characterization of wave propagation in elastic and elastoplastic granular chains, Physical Review E, 89 (2014) 012204.
[95] T. On, E. Wang, J. Lambros, Plastic waves in one-dimensional heterogeneous granular chains under impact loading: Single intruders and dimer chains, International Journal of Solids and Structures, 62 (2015) 81-90.
[96] H.A. Burgoyne, C. Daraio, Elastic–plastic wave propagation in uniform and periodic

granular chains, Journal of Applied Mechanics, 82 (2015).
[97] E.B. Herbold, V.F. Nesterenko, The role of dissipation on wave shape and attenuation in granular chains, Physics Procedia, 3 (2010) 465-471.
[98] A. Rosas, A.H. Romero, V.F. Nesterenko, K. Lindenberg, Observation of two-wave structure in strongly nonlinear dissipative granular chains, Physical review letters, 98 (2007) 164301.
[99] M. Manciu, S. Sen, A.J. Hurd, Impulse propagation in dissipative and disordered chains with power-law repulsive potentials, Physica D: Nonlinear Phenomena, 157 (2001) 226-240.
[100] A. Rosas, K. Lindenberg, Pulse dynamics in a chain of granules with friction, Physical Review E, 68 (2003) 041304.
[101] V.F. Nesterenko, Waves in strongly nonlinear discrete systems, Philosophical Transactions of the Royal Society A: Mathematical, Physical and Engineering Sciences, 376 (2018) 20170130.
[102] L. Vergara, Model for dissipative highly nonlinear waves in dry granular systems, Physical review letters, 104 (2010) 118001.
[103] M. Gonzalez, J. Yang, C. Daraio, M. Ortiz, Mesoscopic approach to granular crystal dynamics, Physical Review E, 85 (2012) 016604.
[104] G. Lundberg, H. Sjövall, Stress and deformation in elastic contacts, institute of theory of elasticity and strength of materials, Chalmers Inst. Tech., Pub. 4, Gothenburg, Sweden, (1958).
[105] H. Hertz, Ueber die Beruhrung fester elastischer Korper, J reine angew Math, 92 (1882) 156-171.
[106] V. Nesterenko, Propagation of nonlinear compression pulses in granular media, Journal of Applied Mechanics and Technical Physics, 24 (1983) 733-743.
[107] Y. Starosvetsky, A.F. Vakakis, Traveling waves and localized modes in one-dimensional homogeneous granular chains with no precompression, Physical Review E, 82 (2010) 026603.
[108] J. English, R. Pego, On the solitary wave pulse in a chain of beads, Proceedings of the American Mathematical Society, 133 (2005) 1763-1768.
[109] J. Yang, C. Silvestro, D. Khatri, L. De Nardo, C. Daraio, Interaction of highly nonlinear solitary waves with linear elastic media, Physical Review E, 83 (2011) 046606.
[110] M.F. Ashby, D. Cebon, Materials selection in mechanical design, Le Journal de Physique IV, 3 (1993) C7-1-C7-9.
[111] T.A. Harris, Rolling bearing analysis, John Wiley and sons, 2001.
[112] R. Bao, T. Yu, Impact and rebound of an elastic–plastic ring on a rigid target, International Journal of Mechanical Sciences, 91 (2015) 55-63.

[113] G. Lu, T. Yu, Energy absorption of structures and materials, Elsevier, 2003.
[114] M. Puttock, E. Thwaite, Elastic compression of spheres and cylinders at point and line contact, Commonwealth Scientific and Industrial Research Organization Melbourne, 1969.
[115] H. Yasuda, Y. Miyazawa, E.G. Charalampidis, C. Chong, P.G. Kevrekidis, J. Yang, Origami-based impact mitigation via rarefaction solitary wave creation, Science advances, 5 (2019) eaau2835.
[116] E. Kim, Y.H.N. Kim, J. Yang, Nonlinear stress wave propagation in 3D woodpile elastic metamaterials, International Journal of Solids and Structures, 58 (2015) 128-135.
[117] H.Y. Hwang, J.W. Lee, J. Yang, C.W. Shul, E. Kim, Sandwich-structured woodpile metamaterials for impact mitigation, International Journal of Applied Mechanics, 10 (2018) 1850078.
[118] M.H. Khan, B. Li, K.T. Tan, Impact load wave transmission in elastic metamaterials, International Journal of Impact Engineering, 118 (2018) 50-59.
[119] K.T. Tan, H.H. Huang, C.T. Sun, Blast-wave impact mitigation using negative effective mass density concept of elastic metamaterials, International Journal of Impact Engineering, 64 (2014) 20-29.
[120] J. Hu, T.X. Yu, S. Yin, J. Xu, Low-speed impact mitigation of recoverable DNA-inspired double helical metamaterials, International Journal of Mechanical Sciences, 161-162 (2019) 105050.
[121] W. Zhang, S. Yin, T. Yu, J. Xu, Crushing resistance and energy absorption of pomelo peel inspired hierarchical honeycomb, International Journal of Impact Engineering, 125 (2019) 163-172.

APPENDIX A: Formation of solitary waves in 1D composite granular chains

The film sensor was placed at three different locations of an S-W composite granular chain (position 1: the 1st and 2nd particle, position 2: the 4th and 5th particle, position 3: the 7th and 8th particle) to explore the formation of solitary waves. Based on the comparison between different waveforms displayed in Fig. 53, the wave shape is maintained during the stress wave propagation despite a slight attenuation of wave amplitude due to frictional effects, which demonstrates that this type of solitary wave can emerge very fast from the initial impact.

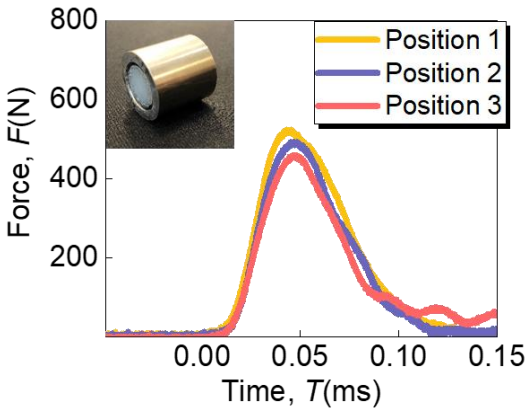

Figure 53 Comparison of waveforms at different locations of an S-W composite chain. Note that the x-axis is shifted for a better comparison.

APPENDIX B: Demonstration of the contact law in 1D composite particles

For further demonstration of the contact law in Eq. (16), a quasi-static compression test on W-S composite particles was conducted. A 3D-printed square box was designed to vertically align the two composite particles (see the inset of Fig. 54). A loading rate of 0.2 mm/min was applied based on an Instron E3000 material testing machine. The force-displacement curve is shown in Fig. 54 (solid line), which is fitted by a power function (dotted line). An exponent of 1.1 is obtained, indicating that the contact law with an exponent of 10/9 in section 2.3.1 is reliable to describe the interaction between two composite cylinders.

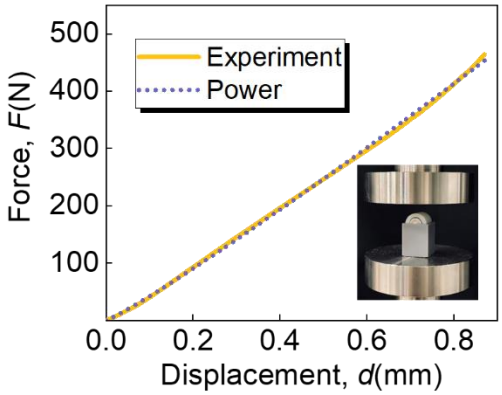

Figure 54 Validation of the power contact law based on a compressive test of two W-S particles

APPENDIX C: Mesh size convergence study of equivalent systems

In FE models of the equivalent systems, a finer mesh is considered within the vicinity of the contact point between two particles, and a gradient variation was applied from the contact point to the middle plane of each spherical particle. The mesh size convergence study was conducted to ensure the calculation accuracy. As shown in Fig. 55, five gradient mesh sizes were applied. Group A and B refer to the forces on particle 5^{th} and 10^{th}, respectively. Thus, it is reasonable to use a gradient mesh size of 0.05~2 mm in the study of equivalent systems.

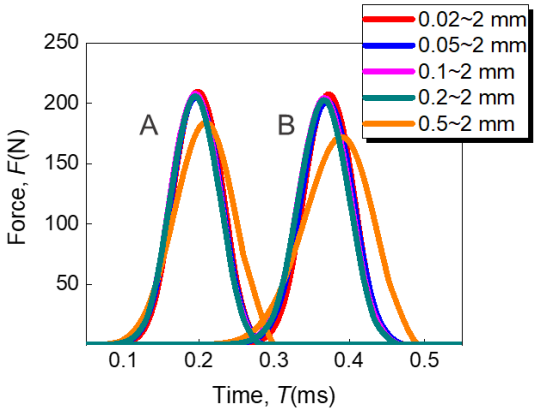

Figure 55 Mesh size convergence study of the equivalent systems: five gradient mesh sizes (0.02~2 mm, 0.05~2 mm, 0.1~2 mm, 0.2~2 mm, 0.5~2 mm) were considered.

APPENDIX D: The evaluation criteria of equivalent systems used in experiments

As v_m cannot be directly measured from experiments, it is important to resort to the relation between v_m and the force captured by the film sensor $F_{m,e}$. Considering that the solitary wave speed V_s has a nonlinear dependence on the v_m and the maximum compression force between particles F_m, written as [1]

$$V_{\mathrm{s}}=\left[\frac{8}{5\pi\left(1-\nu^{2}\right)}\times\frac{E^{*}}{\rho}\right]^{\frac{2}{5}}v_{\mathrm{m}}^{\frac{1}{5}}=0.6802\left(\frac{2E^{*}}{2R\rho^{3/2}\left(1-\nu^{2}\right)}\right)^{1/3}F_{m}^{1/6}. \tag{52}$$

As such, the relation between v_m and F_m can be derived accordingly.

$$v_{m}=1.782\left[\frac{\left(1-\nu^{2}\right)^{2}}{\left(2R\right)^{10}E^{*2}\rho^{3}}\right]^{\frac{1}{6}}F_{m}^{\frac{5}{6}}. \tag{53}$$

Contact force-time curves and the average force-time curve are shown in Fig. 56 to interpret the average compression force obtained in experiments and compare the results of experiments and simulation. A coefficient β obtained from numerical simulation is defined to relate the maximum value of compression force between particles and the maximum value of average compression force captured by a sensor embedded in particle, which can be written as [14]:

$$F_{m}=\beta F_{m,e}+F_{0}, \tag{54}$$

where $F_{m,e}$ is the maximum value of average compression force obtained in the experiments and F_0 is the pre-compression force. Note that there is no pre-compression

in experiments. In addition, it has been proved that the coefficient tends to have negligible dependence on the material properties of the particles [14]. Therefore, the coefficient can be obtained from the simulation results directly, i.e., $\beta = 1.35$.

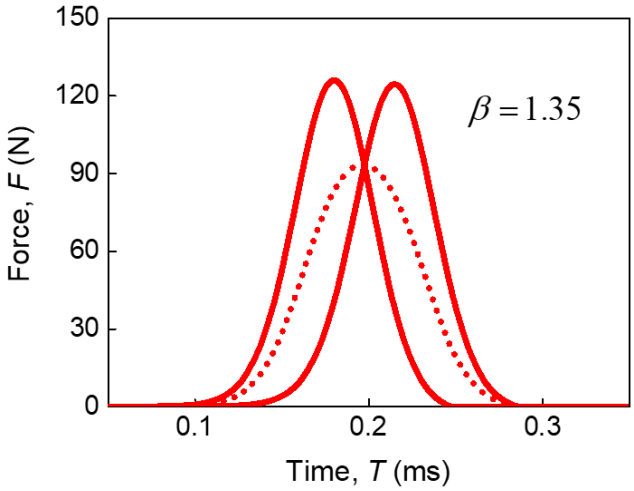

Figure 56 The numerical results of contact force-time curves (the left and right curves in solid line) and average force-time curve (the central curve in dot line), which is also used to obtain the numerical coefficient β representing the ratio of the dynamic contact force between two particles to the maximum dynamic compression force in the center of the given particle.

APPENDIX E: The amplitude decay in experiments of equivalent systems

According to the experimental results shown in Fig. 21, a decay in the amplitude of the 10th particle is observed, which may result from the friction and tiny gap between the particles during the experiments. Hence, the effects of the gap between particles and the friction between the particle and the guide rail are numerically investigated. A 0.1 mm gap is set between the 11th and 12th particles and compared the results of cases with and without a gap in Fig. 57. Group A refers to the contact force between the 5th and 6th particles, while group B is the contact force between the 10th and 11th particles. Decay in the amplitude of contact force was observed upon the case with a gap, indicating that the effect of a tiny gap may be one of the reasons for the dissipation in experiments.

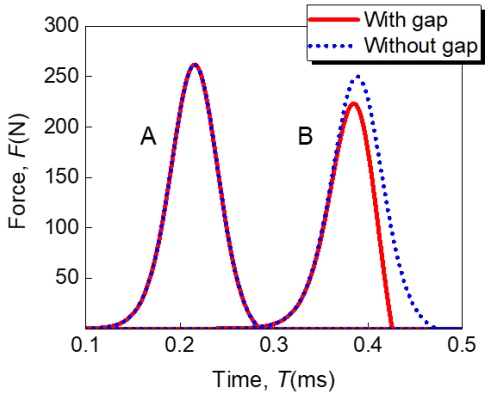

Figure 57 The effect of tiny gap on stress wave propagation within spherical granular chain.

For exploring the frictional effect during the tests, a tube is included in the finite element model as a simplified guide (Fig. 58) and the frictional coefficient is set to 0.3.

Based on the results of frictionless and frictional cases (Fig. 59), a clear decay of magnitude was observed in the frictional case, which demonstrates that the existing friction will also cause dissipation during the experiment.

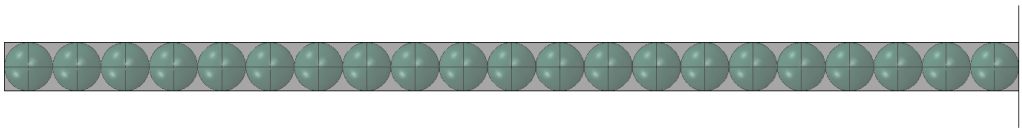

Figure 58 Spherical granular chain model with tube guide.

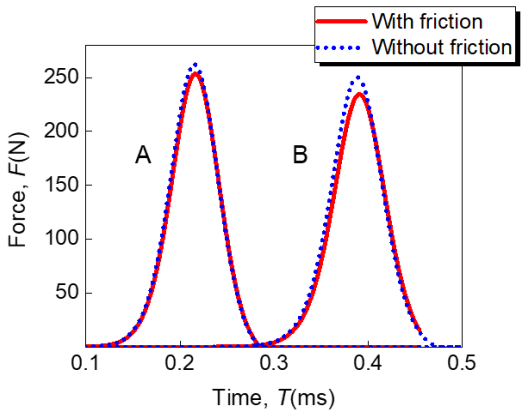

Figure 59 The effect of friction on stress wave propagation within spherical granular chain

APPENDIX F: The return pass in equivalent systems

It is of great significance to include other wave properties (e.g., reflected waves, waves broken down, and secondary solitary waves) into equivalent systems study. The return pass of the solitary waves is numerically explored in the two types of equivalent systems Based on the results shown in Fig. 60, each group can also achieve equivalent rebound properties. Due to the effect of the rigid wall at the end of the granular chain, there exists an increasing trend during the rebounding process.

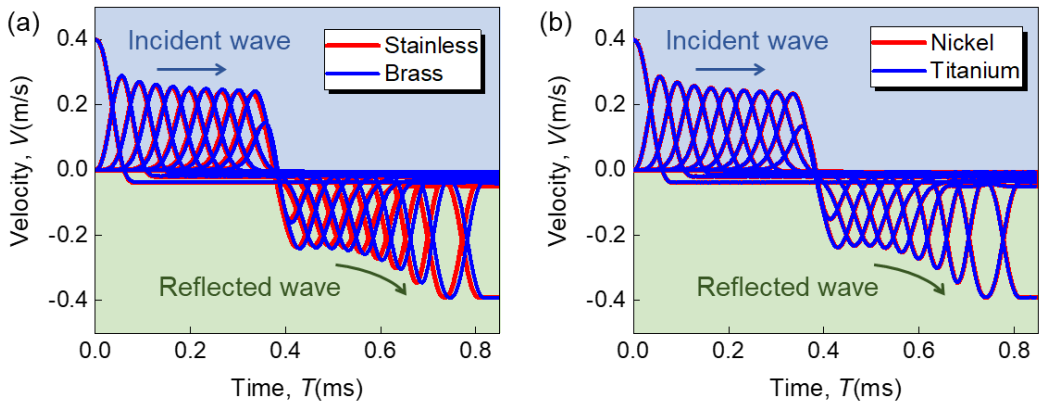

Figure 60 Wave transmissions in two types of equivalent systems: (a) Generalized equivalent system: stainless and brass; (b) Restricted equivalent systems: Nickel and Titanium

APPENDIX G: Waveforms in experiments of 1D cylindrical granular chains

Triggered by the dropping impactor, a photoelectric sensor was adopted as an external input signal to the oscilloscope. The waveforms at different positions can be obtained by changing the position of the film sensor and keeping an identical drop height of the impactor (i.e., identical impact velocity). Fig. 61 shows an example of how to achieve and analyze the waveforms. The film sensor is connected to channel 1 of the oscilloscope, while the photoelectric sensor (the external signal) is connected to channel 2. Channel 1 is set as the trigger, indicating that the waveforms recorded by the film sensor will start at the same time upon different tests. In that case, the interval between the two signals will be different corresponding to two positions of the film sensor. The relative time can be calculated (t^* in Fig. 61(a)) and the waveforms can be obtained by translation (Fig. 61(b)).

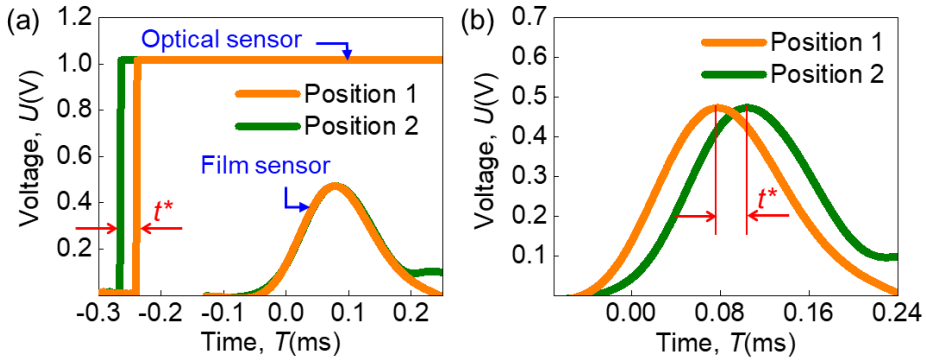

Figure 61 The methodology to obtain waveforms in granular chain tests. (a) The original waveforms from channels 1 (the film sensor) and 2 (the photoelectric sensor). A relative time (t^*) is measured to determine the actual time difference between the two tests given two different positions of the film sensor. (b) The desired waveforms after translation.

APPENDIX H: Mesh size convergence study of 1D cylindrical granular chains

A mesh size convergence study is conducted to achieve optimal mesh size in the FE models of 1D cylindrical granular chains. Six different mesh sizes varying from 0.5 mm to 5.0 mm are considered and two groups of contact force are shown in Fig. 62. As a result, a mesh size of 1 mm is selected for HC particles and at least two layers of elements are set along the thickness direction of the HC particles in view of the thin wall thickness under cases with higher thickness ratios.

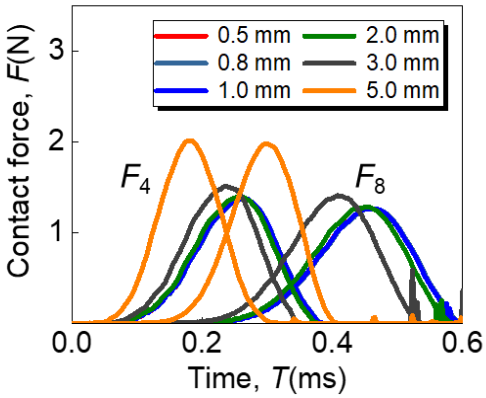

Figure 62 Mesh size convergence study. Six mesh sizes are considered (0.5 mm, 0.8 mm, 1.0 mm, 2.0 mm, 3.0 mm, and 5.0 mm) and two groups of contact force (F_4 and F_8) are compared.

APPENDIX I: The effect of gravity

Since HC particles were vertically aligned in the guide, it is worth exploring the gravitational effects on transmitted waves in 1D HC granular chains. Thus, numerical results from cases with and without gravity are compared in Fig. 63, where the gravitational effect is negligible for a short chain (Region I in Fig. 63, ~9 particles) and noticeable for a longer chain (Region II) in view of wave speed and amplitude. A non-uniform pre-compression distribution has been achieved if gravity is included in the model, while there is no pre-compression for cases without gravity. In this study, the gravitational effect is not considered in the numerical simulation to simplify the model. Meanwhile, the selected positions for the film sensor were far away from the end of the granular chain (Region II) to avoid the influence of gravity and fully validate the finite element model.

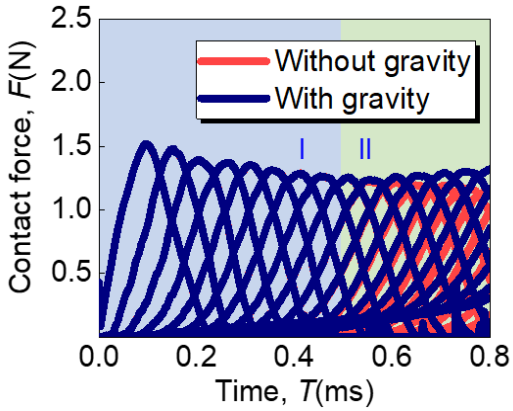

Figure 63 The effect of gravity. The evolution of the contact force was compared upon a specific case (R/t = 20, V_i = 0.1 m/s, N = 20, M/m = 1) with and without gravity, respectively. Two regions (regions I and II) were obtained given the gravitational effects on the granular chain.

APPENDIX J: The elastic assumption of 1D cylindrical granular chains

The yield velocity of material is derived from the stress-velocity relation of the longitudinal elastic wave and there exists stress concentration between different particles in the proposed granular chain. Moreover, the maximum stress is not linearly dependent on the impact velocity. It is important to further demonstrate the elastic assumption applied in this study. Considering all the loading scenarios included in the parametric study, the most critical case might be either "highest impact velocity and thickness ratio" in Section 4.1.3.1 (V_i = 1 m/s, R/t = 20, M/m = 1, and N = 20) or "highest impactor-to-particle mass ratio and thickness ratio" in Section 4.1.3.2 (V_i = 0.1 m/s, R/t = 20, M/m = 10, and N = 20). Also, one additional case with a combination of highest impact velocity, impactor-to-particle mass ratio, and thickness ratio (V_i = 1 m/s, R/t = 20, M/m = 10, and N = 20) is simulated to further demonstrate the assumption.

The 1st cylindrical particle is analyzed due to its direct interaction with the impactor and stress concentration at the contact point (Fig. 64(a)). Based on the maximum Von Mises stress presented in Fig. 64(b), the highest stress value is 157 MPa, while the yield strength of 6061-T6 aluminum is typically around 270 MPa, which demonstrates that the system is within the elastic limit for all the loading scenarios investigated in this study. In addition, an equivalent deformation (d) can be obtained by evaluating the difference between the displacements of two points at the center of each edge, i.e., u_1 and u_2 (Fig. 64(c)). According

to the evolution of equivalent deformations obtained from the 1st cylindrical particle in different loading scenarios shown in Fig. 64(d), the maximum deformation of the cylindrical particle is under 0.05 mm, which is covered by the deformation range (0-0.3 mm) in the contact model. Therefore, it is quite reasonable to apply the elastic assumption in this study.

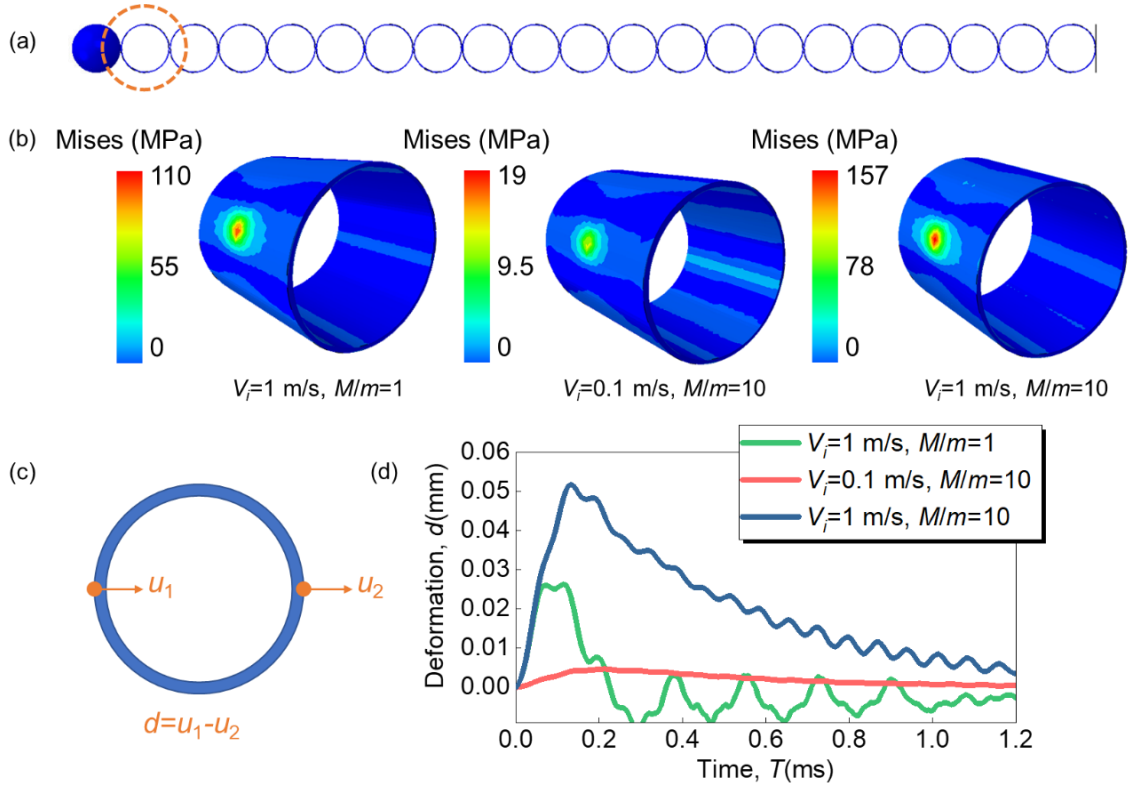

Figure 64 The investigation on elastic assumption. (a) A critical granular chain (R/t = 20, N = 20), where the 1st cylindrical particle is selected to investigate its response during the stress wave propagation. (b) The maximum Mises stress of the 1st cylindrical particle in three critical loading scenarios. (c) The definition of equivalent deformation of the 1st cylindrical particle. (d) The evolution of equivalent deformations obtained from the 1st cylindrical particle in different loading scenarios displayed in (b).

APPENDIX K: The mitigating effect of 1D HC chains under a higher impact velocity

In Section 4.1.3.1, three impact velocities (i.e., 0.1 m/s, 0.5 m/s and 1 m/s) were selected to investigate the effect of impact velocity on 1D HC granular chains. An interesting phenomenon was discovered that the HC granular chain is capable of delivering stress waves with amplitude-independent wave speed. Moreover, the force mitigation effect is superior under higher impact velocities. Herein, one additional case with an impact velocity of 10 m/s (R/t = 20, M/m = 1, and N = 20) was conducted and analyzed to demonstrate the universality of these existing results. The demonstration of existing results is shown in Fig. 65, where the profiles of contact forces, the wave width variation, and comparison of wave speeds are given.

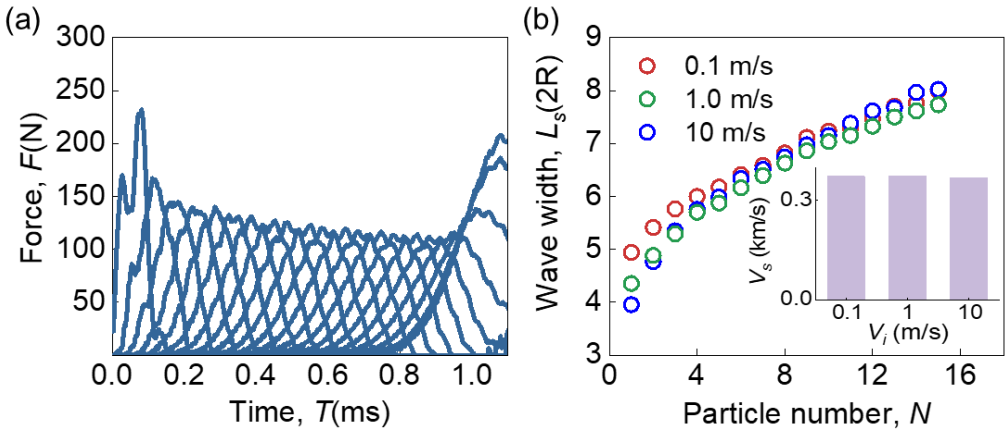

Figure 65 The demonstration of existing results under an impact velocity of 10 m/s. (a) Contact forces of different particles (R/t = 20, M/m = 1, N = 20). (b) Wave width variation in space domain under different impact velocities (i.e., 0.1 m/s, 1 m/s and 10 m/s). The inset shows wave speeds of corresponding cases.

It appears that the amplitude-independent wave speed is valid under higher impact

velocities and the varying trend of wave width is consistent under different impact velocities. Furthermore, the specific force mitigation ratio is 49.18% obtained from Fig. 65(a), which is further decreased compared to 62.08% in the case with an impact velocity of 1 m/s. Therefore, the existing results for impact velocities are not limited to the range of 0.1-1 m/s and are consistent under higher impact velocities.

APPENDIX L: Investigation on the reusability of 1D kirigami lantern chains

Five impact tests were conducted sequentially to demonstrate the reusability of the proposed 1D kirigami lantern chain (Fig. 66). Due to possible plastic deformation in the first impact, a slight increase of the maximum strain is observed within the first few kirigami cells starting from the second impact, especially the first kirigami cell. Despite the minor variation, the solid performances during repeated tests show that the proposed kirigami chain can be reusable for impact mitigation.

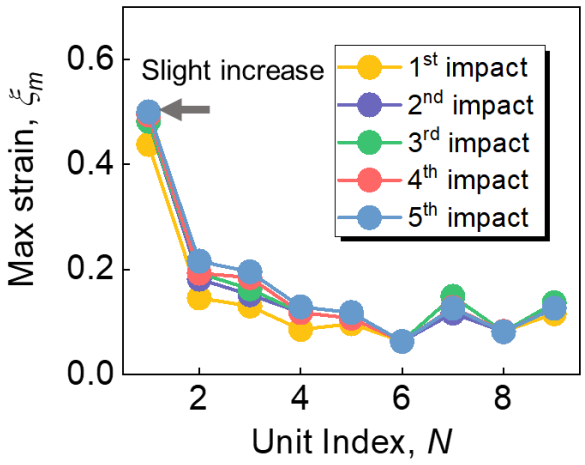

Figure 66 Demonstration of the reusability via five repeated impacts in experiments

APPENDIX M: PERMISSION LETTERS

Permission letters from the publishers are provided below for reusing my previous publications in the dissertation.

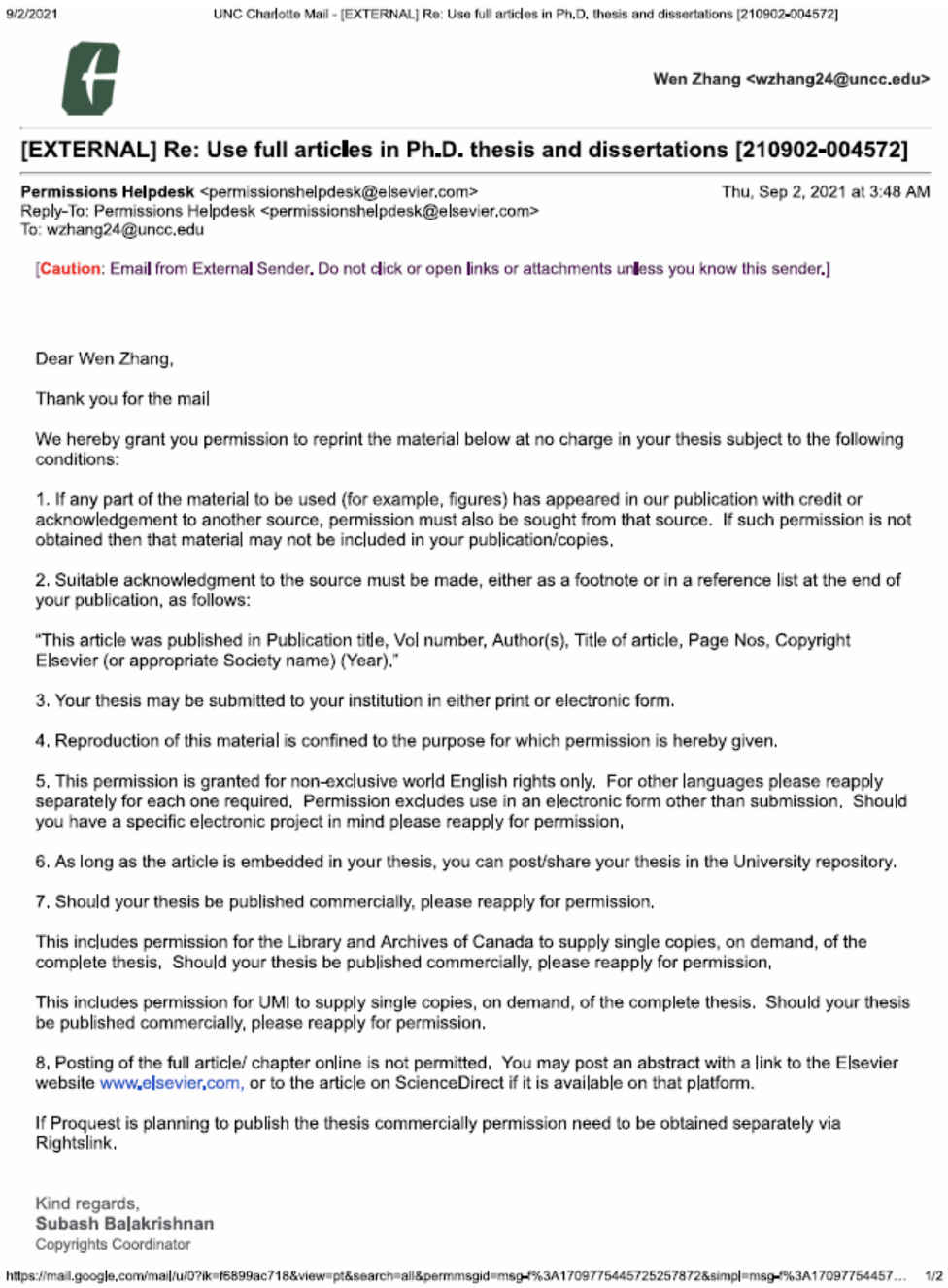

9/2/2021 UNC Charlotte Mail - [EXTERNAL] Re: Use full articles in Ph.D. thesis and dissertations [210902-004572]

Wen Zhang <wzhang24@uncc.edu>

[EXTERNAL] Re: Use full articles in Ph.D. thesis and dissertations [210902-004572]

Permissions Helpdesk <permissionshelpdesk@elsevier.com> Thu, Sep 2, 2021 at 3:48 AM
Reply-To: Permissions Helpdesk <permissionshelpdesk@elsevier.com>
To: wzhang24@uncc.edu

[Caution: Email from External Sender. Do not click or open links or attachments unless you know this sender.]

Dear Wen Zhang,

Thank you for the mail

We hereby grant you permission to reprint the material below at no charge in your thesis subject to the following conditions:

1. If any part of the material to be used (for example, figures) has appeared in our publication with credit or acknowledgement to another source, permission must also be sought from that source. If such permission is not obtained then that material may not be included in your publication/copies.

2. Suitable acknowledgment to the source must be made, either as a footnote or in a reference list at the end of your publication, as follows:

"This article was published in Publication title, Vol number, Author(s), Title of article, Page Nos, Copyright Elsevier (or appropriate Society name) (Year)."

3. Your thesis may be submitted to your institution in either print or electronic form.

4. Reproduction of this material is confined to the purpose for which permission is hereby given.

5. This permission is granted for non-exclusive world English rights only. For other languages please reapply separately for each one required. Permission excludes use in an electronic form other than submission. Should you have a specific electronic project in mind please reapply for permission.

6. As long as the article is embedded in your thesis, you can post/share your thesis in the University repository.

7. Should your thesis be published commercially, please reapply for permission.

This includes permission for the Library and Archives of Canada to supply single copies, on demand, of the complete thesis. Should your thesis be published commercially, please reapply for permission.

This includes permission for UMI to supply single copies, on demand, of the complete thesis. Should your thesis be published commercially, please reapply for permission.

8. Posting of the full article/ chapter online is not permitted. You may post an abstract with a link to the Elsevier website www.elsevier.com, or to the article on ScienceDirect if it is available on that platform.

If Proquest is planning to publish the thesis commercially permission need to be obtained separately via Rightslink.

Kind regards,
Subash Balakrishnan
Copyrights Coordinator

https://mail.google.com/mail/u/0?ik=f6899ac718&view=pt&search=all&permmsgid=msg-f%3A1709775445725257872&simpl=msg-f%3A17097754457... 1/2

Wen Zhang <wzhang24@uncc.edu>

Reuse a paper in Ph.D. thesis

Journalpermissions <journalpermissions@springernature.com> Wed, Sep 8, 2021 at 6:17 PM
To: Wen Zhang <wzhang24@uncc.edu>

[**Caution**: Email from External Sender. Do not click or open links or attachments unless you know this sender.]

Dear Wen,

Thank you for your email.

ProQuest is a self-archiving repository, so is an acceptable place to deposit an Article under our self-archiving policy (please see below).

Springer Nature journal authors retain broad rights to self-archive the Accepted Manuscript version of their article, details of which may be found on our Publication Policies page. This will explain any relevant embargos, as well as where deposits may be made. You may also reference your Licence to Publish which will detail what self-archiving rights you retain. Our self-archiving policy permits authors to deposit their Accepted Manuscripts on their own personal website and/or in their funder or institutional repositories.

Many thanks,

Bod,

Bod Adegboyega

Permissions Assistant

Springer Nature

4 Crinan Street, London N1 9XW, UK

T +44 (0) 442034263235

Bod.adegboyega.1@springernature.com